Triplet Exciton Transport in Porphyrin-Based Surface-Anchored Metal-Organic Framework Thin Films

Zur Erlangung des akademischen Grades eines
Doktor-Ingenieurs
von der KIT-Fakultät für Elektrotechnik und Informationstechnik des
Karlsruher Instituts für Technologie (KIT)

genehmigte
Dissertation
von

Michael Adams, M. Sc.

Tag der mündlichen Prüfung:	17. Juli 2019
Hauptreferent:	Prof. Dr. Bryce Sydney Richards
Korreferent:	Prof. Dr. Gerd Ulrich Nienhaus

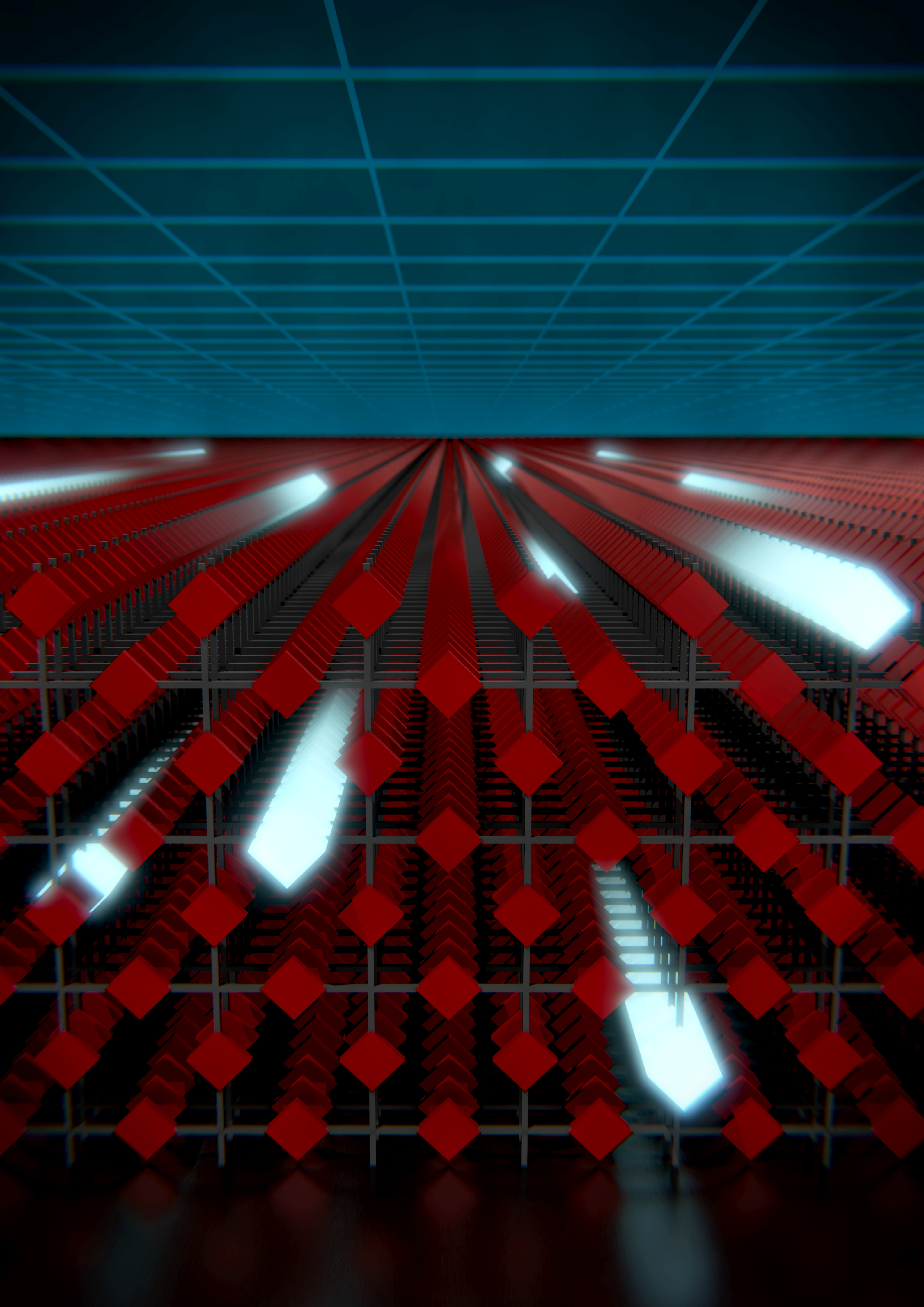

Contents

Kurzfassung

Aufstrebende Technologien wie organische Leuchtdioden oder organische Photovoltaik sind angewiesen auf den effizienten Transport von angeregten elektrischen Zuständen, wie z. B. Exzitonen. In Pflanzen basiert Exzitontransport auf geordneten Arrangements von Porphyrin-Molekülen. Dieses Konzept kann künstlich angewandt werden, indem solche Moleküle mittels eines metall-organischen Gerüsts (metal-organic framework, MOF) angeordnet werden, was entweder als MOF-Pulver oder in Form eines dünnen Films (surface-anchored metal-organic framework, SURMOF) möglich ist.

Bei SURMOFs handelt es sich um kristalline molekulare Gerüste, die ein hohes Maß an innerer Ordnung aufweisen und dabei einfach aus Lösungen herstellbar sind. Bei den untersuchten SURMOF-Proben handelt es sich um Dünnschicht-Filme, in welchen Palladium-Porphyrin-Verbindungsmoleküle (PdP) sich zu dicht gepackten, aufrecht stehenden Ebenen anordnen. Indem PdP-Moleküle als Bausteine eingesetzt werden kann eine hohe Ausbeute an Triplett-Exzitonen erzielt werden. Die üblicherweise langen Lebensdauern von Tripletts sind vorteilhaft in Bezug auf den Transport von angeregten Zuständen über große Distanzen.

Im Zentrum dieser Dissertation steht die Untersuchung des Transports angeregter Zustände in besagten PdP-SURMOF-Dünnschicht-Filmen. Dazu wird eine Kombination experimenteller Techniken eingesetzt. Ein eigener Messaufbau für transiente Absorptionsspektroskopie (TAS) wurde im Zuge dieser Arbeit entwickelt und aufgebaut. Ergänzt werden die TAS-Messungen von zeitaufgelöster Elektronenspinresonanz, zeitaufgelöster und stationärer Lumineszenz-Spektroskopie sowie Lumineszenz-Mikrokopie.

Es zeigt sich, dass der Transport von Triplett-Exzitonen innerhalb von PdP-SURMOF-Filmen tatsächlich effizient ist. Sprung-Raten zwischen benachbarten Molekülen auf der Größenordnung von $10^{11}\,\mathrm{s}^{-1}$ können ermittelt werden. Zusammen mit der langen mono-molekularen Lebensdauer der Tripletts ermöglicht dies Diffusionslängen von mehreren Mikrometern (etwa $6.3\,\mu\mathrm{m}$). Der Exzitonen-Transport ist dabei stark anisotrop, da eindimensionale Diffusion zwischen benachbarten Porphyrin-Ebenen bevorzugt stattfindet.

Anhaltende Beleuchtung, selbst unter Vakuum, führt zu einer fotochemischen Reaktion, welche Fotoprodukt-Moleküle innerhalb der SURMOF-Struktur entstehen lässt. Bei diesen Defekten handelt es sich mit hoher Wahrscheinlichkeit um Chlorin-Moleküle. Bei Kontakt mit diesen dissoziieren die Triplett-Exzitonen. Die daraus entstehenden Radikale können mittels zeitaufgelöster Elektronenspinresonanz nachgewiesen werden. Diese Deaktivierung der Tripletts verringert die erreichbare Diffusionslänge. Dies ist abhängig von der Konzentration der Fotoprodukt-Defekte, welche wiederum von der Anzahl absorbierter Photonen abhängt. So führt zum Beispiel eine Belichtung mit dem Äquivalent von 110 h Sonneneinstrahlung zu einer Verringerung der Triplett-Diffusionslänge auf 45 % des Wertes in einem unbelichteten Film.

Eine weitere Begrenzung der Transport-Distanz von Triplett-Exzitonen stellt die Größe der PdP-SURMOF-Kristallite dar. Dies konnte in den vorliegenden Filmen durch Lumineszenz-Mikrokopie ermittelt werden. Korngrößen unterhalb des optischen Auflösungslimits verhindern die direkte Beobachtung von Exziton-Diffusion über mehrere Mikrometer hinweg. Der eindimensionale Transport innerhalb der Kristallite ist jedoch weiterhin effizient.

Einige lohnende Herausforderungen bestehen noch: Diese sind vor allem das Ändern der Vorzugsrichtung des Transports, die Verbesserung der Fotostabilität des Materials sowie die Erhöhung der Kristallit-Größe durch neue Herstellungsverfahren. Allgemein können PdP-SURMOFs jedoch bereits jetzt vorteilhafte fotophysikalische

Eigenschaften attestiert werden, insbesondere im Hinblick auf Anwendungen welche auf effizienter Erzeugung und dem Transport von Triplett-Exzitonen basieren.

Abstract

Efficient transport of excited states such as excitons is an important ingredient in rising technologies such as organic light-emitting diodes or organic photovoltaics. Exciton transport in plants relies on ordered arrays of porphyrin molecules. This concept can be mimicked synthetically by arranging porphyrin molecules in a metal-organic framework (MOF) powder or a surface-anchored MOF (SURMOF) thin film.

SURMOFs are crystalline molecular scaffolds that possess a high degree of internal order and are at the same time easy to deposit as thin films from solution. The investigated palladium porphyrin (PdP) SURMOF samples are prepared as thin films ($\approx 200\,\mathrm{nm}$ thick) in which the porphyrin linkers assemble into upright-standing sheets that are closely spaced. By utilizing PdP linkers as building blocks, a high triplet exciton yield can be achieved. The typically long lifetimes of triplets are beneficial for long-distance excited state transport.

This thesis focuses on investigating the excited state transport in PdP SURMOF thin films by a combination of experimental methods. Notably, a custom transient absorption spectroscopy (TAS) setup was developed for this task. Other methods include time-resolved electron paramagnetic resonance spectrosopy (trEPR), time-resolved and steady-state photoluminescence (PL) spectroscopy and PL microscopy.

Triplet exciton transport inside PdP SURMOFs is indeed found to be efficient, with exciton hopping rates on the order of $10^{11}\,\mathrm{s}^{-1}$. In combination with the long monomolecular triplet lifetime, diffusion lengths of several micrometers (around $6.3\,\mu\mathrm{m}$) are possible. Exciton transport is established to be strongly anisotropic, favoring 1D triplet transport between adjacent porphyrin sheets.

Prolonged illumination – even under vacuum conditions – leads to a photochemical reaction that produces photoproduct sites inside the PdP SURMOF. These defects are likely to be identified with chlorin molecules. Triplet excitons dissociate at these sites. The resulting radicals can be monitored via trEPR. The triplet quenching reduces the achievable diffusion length. This depends on the concentration of photoproduct sites which in turn depends on the number of absorbed photons per volume. For example, exposure to an equivalent of 110 h of sunlight leads to a reduction in triplet diffusion length to 45 % of the value in a pristine film.

Another limiting factor on the exciton transport distance is the size of crystalline domains in the PdP SURMOF. This could be established in the present samples via PL microscopy. Domain sizes below the optical resolution limit prevent direct observation of multi-micron exciton diffusion. However, 1D transport inside each crystal domain is still efficient.

Some open challenges remain. These are, most notably, changing the preferential transport direction, improving the material's photostability and increasing the size of crystal domains by novel deposition methods. Overall, the PdP SURMOF material is found to have highly beneficial photophysical properties already in its present state, especially with regard to applications that rely on efficient generation and transport of triplet excitons.

Acknowledgments

First, I would like to thank my supervisor Prof. Dr. Bryce Richards for giving me the opportunity to pursue my PhD in such a positive environment and supporting me throughout it.

I want to thank Prof. Dr. Nienhaus for awakening my interest in photophysics during my master studies in his biophysics lecture, for giving me the opportunity to collaborate and perform microscopy experiments on our SURMOF samples, and for agreeing to be the second reviewer of my dissertation.

Special thanks goes to Dr. Ian Howard for his continuous strong support in all aspects of my work. His joyful fascination with all photophysics helped me keep my motivation up even in times when setups broke or data appeared not to make sense. He freely shared his extensive theoretical and practical know-how – hands-on, if necessary (e. g. during the infamous chiller crisis of 2016/17). He was always available for constructive feedback. Moreover, bouldering and skiing outings will be fondly remembered!

My publications and this thesis would not have been possible without all the collaboration partners from other institutes that assisted me along the way, namely Dr. Ritesh Haldar and Prof. Dr. Christof Wöll from the Institute of Functional Interfaces at KIT; Rui Ma and Prof. Dr. Ulrich Nienhaus from the Institute of Applied Physics at KIT; Dr. Mariana Kozlowska and Prof. Dr. Wolfgang Wenzel from the Institute of Nanotechnology at KIT; Dr. Rowan MacQueen, Felix Kraffert, Dr. Jan Behrends and Prof. Dr. Klaus Lips from Helmholtz Zentrum Berlin; Dr. Ganapathi Emandi and Prof. Dr. Mathias Senge from Trinity College Dublin.

I want to thank the Karlsruhe School of Optics and Photonics for enabling me to grow my knowledge and skills outside the topics of my PhD thesis.

When I joined the Richards group in 2015, it was a small circle of four PhD students, two post-docs and one professor. Since then, it has grown extensively and the exchange – both social, cultural and professional – with the group members has enriched my time there immensely. Special thanks go to my long-term office companions Sheying and Nicolò for the shared laughs, rants and the steady supply of Chinese and Italian sweets. I want to thank Michael for lots of interesting discussions and Marius for the productive (?) time in both the TrALaLa and The Rock.

◆

Zu guter Letzt möchte ich natürlich noch meiner Familie danken. Dies gilt insbesondere meinen Eltern Anni & Gerhard, die mir mein ganzes Leben über große Freiheit und bedingungslose Unterstützung gaben und geben. Zudem möchte ich meiner Schwester Kerstin für ihr offenes Ohr und Verständnis danken und viel Erfolg bei der eigenen Dissertation wünschen! Meine Freundin Manuela hatte unschätzbaren Anteil daran, meine geistige (und körperliche) Gesundheit während meiner Zeit als Doktorand auf einem (hoffentlich) guten Niveau zu erhalten. Sie hatte Verständnis wenn es mal wieder länger dauerte („Nur noch schnell eine Messung starten. . . “) und freute sich mit mir über alle Erfolge.

List of Publications

Peer-Reviewed Journals

Parts of this thesis have already been published in peer-reviewed scientific journals:

- **Adams, M.**, Baroni, N., Oldenburg, M., Kraffert, F., Behrends, J., MacQueen, R. W., Haldar, R., Busko, D., Turshatov, A., Emandi, G., Senge, M. O., Wöll, C., Lips, K., Richards, B. S. & Howard, I. A. Reaction of porphyrin-based surface-anchored metal-organic frameworks caused by prolonged illumination. *Physical Chemistry Chemical Physics* **20**, 29142–29151. doi:`10.1039/C8CP05254A`. (2018)
- **Adams, M.**, Kozlowska, M., Baroni, N., Oldenburg, M., Ma, R., Busko, D., Turshatov, A., Emandi, G., Senge, M. O., Haldar, R., Wöll, C., Nienhaus, G. U., Richards, B. S. & Howard, I. A. Highly Efficient One-Dimensional Triplet Exciton Transport in a Palladium–Porphyrin-Based Surface-Anchored Metal–Organic Framework. *ACS Applied Materials & Interfaces* **11**, 15688–15697. doi:`10.1021/acsami.9b03079`. (2019)

The transient absorption spectroscopy setup developed for this thesis has been used by the author for experiments together with collaboration partners, leading to co-authorship in the following publications:

- Haldar, R., Mazel, A., Joseph, R., **Adams, M.**, Howard, I. A., Richards, B. S., Tsotsalas, M., Redel, E., Diring, S., Odobel, F. & Wöll, C. Excitonically Coupled States in Crystalline Coordination Networks. *Chemistry - A European Journal* **23**, 14316–14322. doi:`10.1002/chem.201702968`. (2017)
- Lami, V., Leibold, D., Fassl, P., Hofstetter, Y. J., Becker-Koch, D., Biegger, P., Paulus, F., Hopkinson, P. E., **Adams, M.**, Bunz, U. H. F., Huettner, S., Howard, I., Bakulin, A. A. & Vaynzof, Y. N-Heteroacenes as a New Class of Non-Fullerene Electron Acceptors for Organic Bulk-Heterojunction Photovoltaic Devices. *Solar RRL* **1**, 1700053. doi:`10.1002/solr.201700053`. (2017)

Conference Contributions

Parts of this thesis have been presented at national and international scientific conferences:

- **Adams, M.**, Howard, I. A., Richards, B. S., Weu, A., Vaynzof, Y. Studying the Effects of Degradation in Organic Solar Cell Materials. *80. Jahrestagung der DPG und DPG-Frühjahrstagung*, Regensburg, Germany (08.03.2016), poster
- **Adams, M.**, MacQueen, R. W., Oldenburg, M., Behrends, J., Lips, K., Richards, B. S., Howard, I. A. Photophysics of Porphyrin-Based Surface-Anchored Metal-Organic Frameworks Investigated by Time-Resolved Optical and EPR Spectroscopy. *DPG-Frühjahrstagung*, Mainz, Germany (08.03.2017), poster
- **Adams, M.** Photophysics in Palladium-Porphyrin Metal-Organic Frameworks. *Karlsruhe Days of Optics and Photonics*, Karlsruhe, Germany (08.11.2017), poster

- **Adams, M.**, Baroni, N., Oldenburg, M., Kraffert, F,. Behrends, J., MacQueen, R. W., Busko, D., Turshatov, A., Emandi, G., Senge, M. O., Wöll, C., Lips, K., Richards, B. S., Howard, I. A. Porphyrin-Based Surface-Anchored Metal-Organic Frameworks: Photophysics in Pristine and Photoreacted Samples. *19th International Conference on Physics of Light-Matter Coupling in Nanostructures*, Chengdu, China (18.05.2018), oral presentation

List of Acronyms

AOM	acousto-optic modulator
AOTF	acousto-optical tunable filter
BBO	beta barium borate ($Ba(BO_2)_2$)
BODIPY	boron dipyrromethene
CMP	conjugated microporous polymer
CPA	chirped pulse amplification
CW	continuous wave
DFT	density functional theory
EMCCD	electron multiplying charge-coupled device
EPR	electron paramagnetic resonance
FbP	free-base porphyrin
FRET	Förster resonance energy transfer
FWHM	full width at half maximum
GaN	gallium nitride
GSB	ground-state bleach
GUI	graphical user interface
GVD	group velocity dispersion
HOMO	highest occupied molecular orbital
ISC	intersystem crossing
LBO	lithium triborate (LiB_3O_5)
LPE	liquid-phase epitaxy
LUMO	lowest unoccupied molecular orbital
MALDI-ToF-MS	matrix-assisted laser desorption/ionisation time-of-flight mass spectrometry
MCP	micro-channel plate
MCS	multi-channel scaling
MO	molecular orbital
MOF	metal-organic framework
ND	neutral density, synonym for optical density
Nd:YAG	neodymium-doped yttrium aluminum garnet ($Nd{:}Y_3Al_5O_{12}$)
Nd:YLF	neodymium-doped yttrium lithium fluoride ($Nd{:}LiYF_4$)
Nd:YVO	neodymium-doped yttrium vanadate ($Nd{:}YVO_4$)
OD	optical density
OLED	organic light emitting diode
OPA	optical parametric amplifier
PCE	photoconversion efficiency
PdC	palladium chlorin
PdP	palladium porphyrin (in this work: 15-bis(4-carboxyphenyl)-10,20-diphenylporphyrinato)-palladium(II))

PdTPP	palladium tetraphenyl-porphyrin (palladium(II) meso-tetrakis(4-phenylethynyl)-phenylporphyrin)
PIA	photoinduced absorption
PL	photoluminescence
PLQY	photoluminescence quantum yield
PMT	photomultiplier tube
PtP	platinum porphyrin
PV	photovoltaic
QCW	quasi continuous wave, see section 3.1.3
SAM	self-assembled monolayer
SE	stimulated emission
SFG	sum-frequency generation
SHG	second harmonic generation
SURMOF	surface-anchored metal-organic framework
SVD	singular value decomposition
TAS	transient absorption spectroscopy
TCSPC	time-correlated single photon counting
Ti:Sa	titanium-doped sapphire (Ti:Al_2O_3)
trEPR	time-resolved electron paramagnetic resonance spectrosopy
TTA	triplet-triplet annihilation
WLG	white-light generation
XRD	X-ray diffractometry
ZnP	zinc porphyrin

1 Introduction

Nature clearly has a head-start when it comes to the design of light-harvesting and energy-transporting systems. The intricate molecular machinery that drives photosynthesis in plants and bacteria is the result of eons of evolution. Hence, when science and engineering set out to accomplish similar tasks, they are well-advised to at least seek inspiration from the natural world. Photosynthesis, for instance, is based on light absorption by a conjugated molecule – chlorophyll, from the family of porphyrins – and subsequent exciton transport that is enabled by an ordered arrangement of the molecules.

Such excited state transport is also relevant for many technical applications, for example in organic light emitting diodes (OLEDs) or (organic) photovoltaic (PV) devices. In the latter, ideally, all incoming light is absorbed and converted into electricity. Light absorption in any material can be described by the Beer-Lambert law, according to which the light intensity I is attenuated exponentially over the material's depth coordinate z:

$$I(z) = I_0 e^{-z/L_\mathrm{A}}\,, \tag{1.1}$$

where, I_0 is the incoming light intensity and L_A is the *absorption length*. After L_A, around 63 % of all incoming photons have been absorbed. This leads to the creation of excited states. In inorganic semiconductors, this may be electrons and holes moving independently in the conduction and valence bands, respectively. In organic semiconductors, the electron-hole pair is bound due to the larger Coulomb interaction in the low dielectric environment. The electron and hole then move together, creating a quasi-particle called an *exciton*.

In order to be useful for electricity generation, the excited states need to be transported to an interface such as an heterojunction. If the distance to an exciton's origin is too big, the exciton cannot reach this interface during its limited lifetime and it recombines. This loss mechanism reduces the solar cell's efficiency. Hence, it is crucial that the excitonic *transport length* (or diffusion length, L_D) – defined as the average displacement of an exciton during its lifetime – is sufficiently long: $L_\mathrm{D} > L_\mathrm{A}$.

Excitons are initially created as spin singlets. In the incoherent limit, when singlet excitons hop between molecules via Förster resonance energy transfer (FRET), a theoretical upper bound of 200 nm can be placed on their diffusion length [5]. However, in practical applications, such as organic solar cells based on semiconducting polymers or small molecules, singlet exciton diffusion lengths on the order of 10 nm are typically measured [6].

The singlet's transport length can be extended beyond the theoretical incoherent limit by designing systems in which transport is assisted by coherent mechanisms (i. e. the excitation becomes delocalized over many molecules). In this way, singlet exciton transport lengths on the micron scale have been achieved in self-assembled organic systems such as nanotubes [7, 8] and nanofibers [9] as well as in a conjugated polymer wire embedded in a crystal [10]. However, translating the impressive transport lengths into practical energy harvesting devices based on these exotic material systems is a topic of ongoing research.

Another option for achieving large transport lengths while remaining reliant on incoherent diffusion is to alter the spin state of the exciton to one of triplet character. In this case, the transport shifts from FRET to a Dexter mechanism, which relies on the exchange of two electrons between neighboring molecules. Notably, there is no theoretical upper limit to the diffusion length for triplet excitons [5]. It is, however, highly dependent on the wave function overlap between adjacent molecules and on the mesoscale order within the system [11]. For example, the triplet diffusion length in single-crystal rubrene is around 4 µm [12], whereas triplet transport lengths in semiconducting polymer films typically do not exceed 100 nm [6, 13].

An advantage of Dexter transport over FRET is that the exciton transport pathways and their direction can be better controlled via molecular arrangement and especially the inter-chromophore distances. Networks that enable anisotropic 1D transport were suggested to be particularly desirable for light harvesting [14], as energy transfer can be directed towards an interface or – similar to photosynthesis – a reaction center.

As mentioned above, the ratio between the transport length and the absorption length, L_D/L_A, is crucial when it comes to designing efficient PV materials. This ratio is graphically reviewed in Figure 1.1 for a variety of materials used in photon-harvesting applications. The larger the ratio, the better suited is the material for photon harvesting. If the ratio is greater than 1, the majority of incident photons can be absorbed, and the majority of the excited states created can be transported to the material's surface where they can be used to drive a reaction. If the ratio is less than 1, either a reduced fraction of the incident light can be absorbed or a reduced fraction of the excited-states created can be transported to the material's surface. Therefore, materials whose transport length exceeds their photon absorption length are ideal for photon energy harvesting. Whereas inorganic materials (such as silicon or copper indium gallium selenide (CIGS)), and hybrid materials (such as methylammonium lead halide perovskite) fulfill this requirement, organic materials that can be used to fabricate large area devices usually do not.

Because the processes involved in photosynthesis are similar to those in organic PV, it makes sense to look to nature for inspiration. Ordered arrays of molecules from the family of porphyrins are used both as absorbing chromophores and for efficient singlet exciton transport. One way to obtain such ordered arrangements of (porphyrin) molecules, while retaining the ability to deposit the material on large areas, is the fabrication of surface-anchored metal-organic frameworks (SURMOFs). These thin film materials consist of metal nodes that are connected by organic linker molecules. They can be easily deposited from solution and self-assemble into crystalline molecular scaffolds with a high degree of order. Moreover, choosing linker molecules with a high triplet exciton yield allows to extend the transport length, as discussed above.

This thesis will demonstrate that a palladium-porphyrin-based SURMOF thin-film can achieve a L_D/L_A ratio of around 60 by utilizing anisotropic (1D) triplet diffusion as its transport mechanism. This establishes that

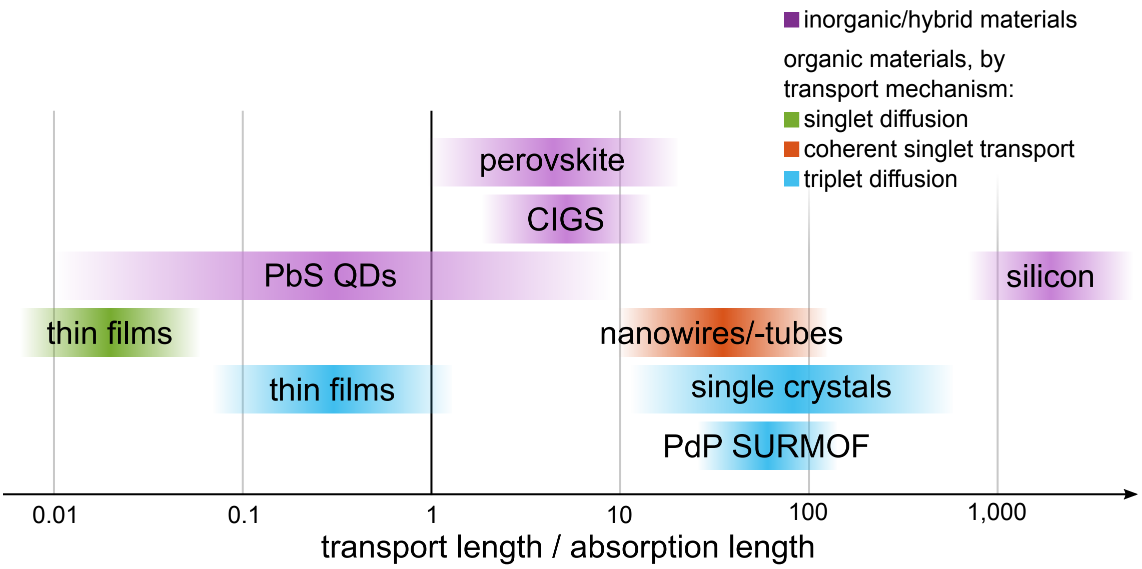

Figure 1.1: Comparison of typical ratios of excited state transport length to absorption length (in the visible and near-infrared) in several materials. The transport mechanism in inorganic or hybrid materials (crystalline silicon [15, 16], perovskites [17, 18], CIGS [19, 20] and PbS colloidal quantum dots [21]) is charge carrier diffusion. In organic materials, excited states move via incoherent singlet exciton diffusion [6, 13], incoherent triplet exciton diffusion (in thin films [6, 13, 22] or molecular crystals [6, 12, 13, 23, 24]) or coherent singlet transport [7, 8, 10, 13]. This work establishes the ratio for anisotropic triplet exciton diffusion in a PdP SURMOF as around 60 (for L_A calculated at the absorption maximum).

such material systems should be of definite interest for photon harvesting applications. What distinguishes this material from other organic systems with micron-scale transport length is the fact that the fabrication process is scalable. Large area thin films of varying thickness and of good optical quality can be easily deposited [25]. Furthermore, this thesis looks into the film's photostability and how film morphology affects the achievable transport distance. The three key topics of this thesis are illustrated in Figure 1.2.

Outline

In chapter 2, the theoretical background of this work is established. First, relevant excitonic processes are presented and discussed, followed by a closer look at porphyrin and its properties. Then, metal-organic frameworks (MOFs) are introduced and an overview of relevant publications focusing on exciton transport in MOFs and SURMOFs is given. Lastly, pump-probe spectroscopy is introduced, as this is one of the main investigative methods used in this work. In chapter 3, relevant experimental techniques and setups are described in detail.

The experimental results of this thesis are presented in chapter 4 to chapter 6. First, in chapter 4, basic photophysical properties of the investigated SURMOF films are established. Furthermore, triplet exciton transport is investigated by transient absorption spectroscopy (TAS) and found to be efficient and anisotropic. In chapter 5, the effect of prolonged illumination on the film's photoresponse is examined. The effect of film morphology – more specifically, the size of crystalline SURMOF domains – is investigated in chapter 6. An attempt to directly measure the triplet diffusion length via luminescence microscopy is presented, which reveals that long-range exciton diffusion is limited in the present thin films by the crystal domain size. This is corroborated in an independent steady-state PL experiment.

In chapter 7, the findings are summarized and discussed in the context of current literature. Potential approaches to overcome the investigated material's drawbacks and to increase its utility are presented as well.

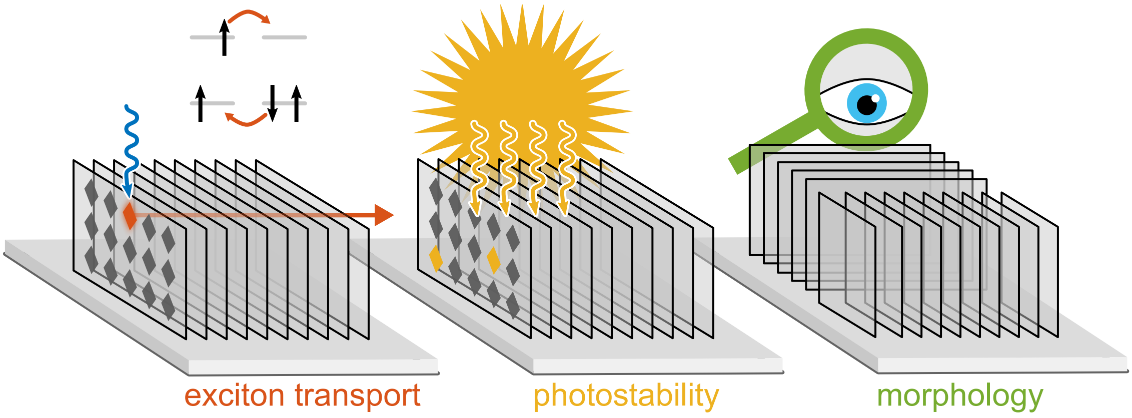

Figure 1.2: Illustration of the key topics in this thesis: Anisotropic triplet exciton transport, photostability under extended illumination and the impact of film morphology on the photoresponse (probed by direct observation via luminescence microscopy) in a porphyrin-based SURMOF.

2 Theoretical Background

This chapter introduces fundamental concepts used in this thesis.

2.1 Excitons in Organic Semiconductors

This section presents a brief fundamental background to excitonic processes in organic semiconductors. Further details can be found in the textbooks *Electronic Processes in Organic Semiconductors* [26] and *Electron Spin Resonance Spectroscopy of Organic Radicals* [27].

2.1.1 Electronic States in a Molecule

When atoms form a molecule, their orbitals combine to form new molecular orbitals (MOs). In the ground state configuration, these are occupied by the electrons according to Hund's rules, starting from the lowest energy MO until the highest occupied molecular orbital (HOMO). The next-highest orbital is known as the lowest unoccupied molecular orbital (LUMO). These two MOs – known as the *frontier orbitals* – play a critical role in electrical and optical processes.

Absorption of light can excite an electron from the HOMO (or a lower orbital) to the LUMO (or a higher orbital), while a "hole" is left in the MO where the electron originated. This hole can be described as a quasi-particle with positive elementary charge. The recombination of electron and hole can occur via emission of a photon. Typical energies for the HOMO-LUMO gap in organic semiconductors are 2 eV to 3 eV (about 600 nm to 400 nm in wavelength units).

Ignoring electron-electron interactions, the excited state lowest in energy is that of one electron in the HOMO and one in the LUMO. However, such interactions are usually not negligible. A superior approximation – known as *configuration interaction* – of the excited state(s) can be obtained by describing such states as weighted linear combinations of different electron configurations. Here, a configuration is defined as one way to distribute the molecule's electrons on the MOs. Typically, the lowest excited state is composed of a 80 % to 95 % contribution of the configuration with one electron in both HOMO and LUMO, with other configurations (e. g. one electron in the HOMO, none in the LUMO and one in the LUMO+1) making up the remaining 5 % to 20 %. Often, the state picture is more useful than the description of the molecule by orbitals.

2.1.2 Aggregates

When two molecules (with ground state energies E_1 and E_2) are close together, they can no longer be treated as independent monomers. The ground state energy of this dimer system becomes

$$E_g = E_1 + E_2 + D\,, \tag{2.1}$$

where D is a (negative) contribution due to van-der-Waals interaction [26]. If one of the molecules is excited ($E_1 \rightarrow E_1^*$), the energy of the dimer is given by [26]:

$$E_\pm = E_1^* + E_2 + D' \pm \beta\,. \tag{2.2}$$

Here, D' represents the van-der-Waals interaction between one molecule in the ground and one in the excited state ($|D'| > |D|$). The last term, β, is a resonance interaction, which leads to a splitting of the energies into E_- and E_+.

Figure 2.1 shows how the energies change from monomer to dimer arrangement. Importantly, the optical transitions depend on the relative alignment of the two transition dipole moments. When the molecules are aligned side-by-side, the dipoles can be arranged parallel or anti-parallel. In the latter case, the resulting total dipole moment is zero, therefore the transition has no oscillator strength and is optically forbidden. Only the transition to the higher-energy state E_+ is allowed, which shifts the absorption spectrum to a smaller wavelength. Because of this hypsochromic shift, this molecular side-by-side configuration is called an *H-aggregate*. When the dipole moments are aligned in a collinear or anti-collinear fashion, again, only the transition with a non-vanishing net dipole moment is allowed. In this case it is the transition to E_- and the absorption spectrum shifts to longer wavelengths. Such dipole arrangements are called *J-aggregates*.[1] When the dipoles are arranged neither in H- nor in J-aggregate configuration, both transitions obtain oscillator strength and are allowed, which leads to a splitting of the absorption spectrum.

2.1.3 Excitons

One of the major differences between inorganic and organic semiconducting materials is their relative permittivity (also known as dielectric constant) ϵ_r. In inorganic semiconductors (such as silicon), the relative permittivity can typically be as high as $\epsilon_\mathrm{r} \approx 11$. Hence, the coulomb interaction between an electron and a hole are efficiently screened. An electron that is lifted to the conduction band by light absorption can be considered as “free”. The same goes for the resulting hole in the valence band. In contrast, the relative permittivity is typically lower in organic semiconductors, with values of around $\epsilon_\mathrm{r} \approx 3.5$. Upon absorption of light, an electron-hole pair is created, which is bound by the unshielded coulomb attraction. Typical binding energies are 0.5 eV to 1.0 eV. This bound electron-hole pair can be described by a single quasi-particle, an *exciton*.

In organic semiconductors, the typical distance between the electron and hole comprising an exciton is below 1 nm, which is smaller than the typical intermolecular distance in organic crystals or polymers. This is known as a *Frenkel exciton*. In inorganic semiconductors, *Wannier-Mott excitons* can be formed which have electron-hole distances up to 10 nm and span several unit cells. A third type of exciton, the *charge-transfer exciton*, is formed when absorption of light leads to the creation of electron and hole in adjacent unit cells. The three exciton types are visualized in Figure 2.2. In the remainder of this thesis, the term *exciton* is used as shorthand for a Frenkel exciton, unless otherwise specified.

2.1.4 Spin States

For a more complete picture, the spin states of the electrons have to be considered as well. For a multi-electron system, the total spin quantum number S is the positive sum of all single-electron spin quantum numbers ($s = \pm 1/2$). In other words, S is the eigenvalue of the spin operator $\vec{S}^2$. Likewise, the magnetic spin quantum number M_S is the eigenvalue of S_z, the projection of the spin vector $\vec{S}$ on the z-axis. A full orbital with paired spins does not contribute to S, because the two spin components cancel each other out. Thus, only singly occupied orbitals need to be taken into account. The magnetic spin quantum number can take the values $M_S = S, S-1, \ldots, -S$, which results in $2S+1$ possible combinations. This value is known as the *spin multiplicity*.

For example, a single unpaired electron – also known as a radical – has $S = 1/2$, a multiplicity of 2 and therefore two possible values for M_S ($+1/2$ and $-1/2$). This is called a *doublet* state. It is visualized in

---

[1] For terminological consistency with the H-aggregate, they should in theory be called B-aggregates due to the bathochromic shift. Instead, the J-aggregate is named after E. E. Jelley, who first characterized such aggregates in 1936 [28]. Moreover, as they were discovered independently by G. Scheibe [29], they are sometimes also called Scheibe aggregates.

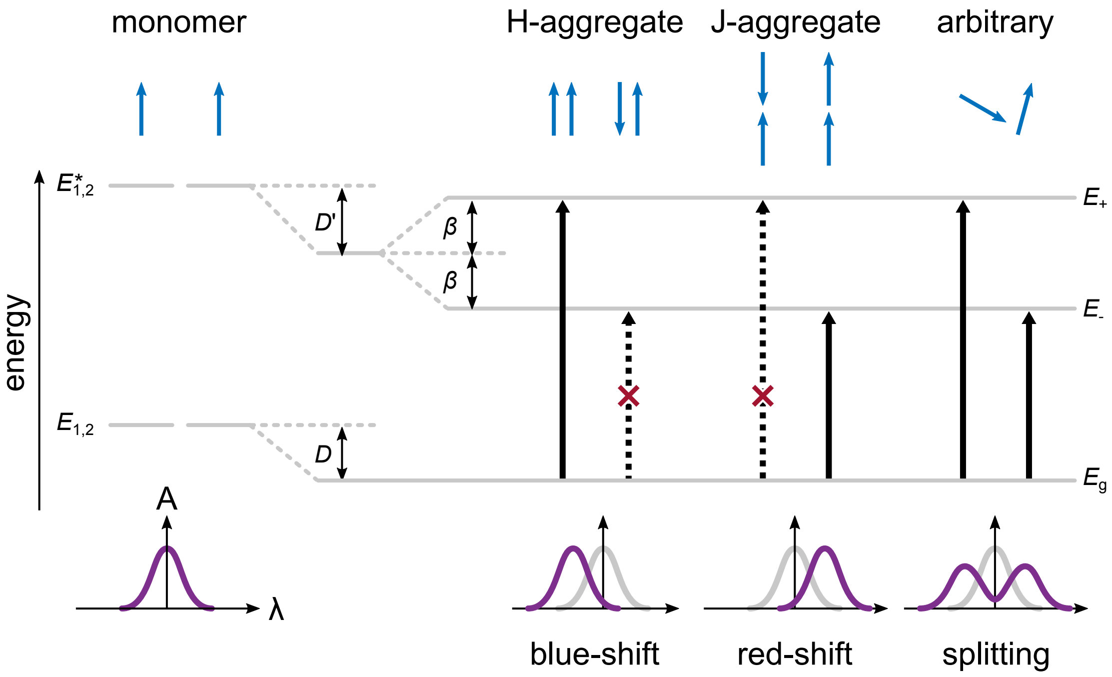

Figure 2.1: Energies and transitions for independent monomers (left) and dimers (right) in H-, J-, and arbitrary dipole configuration (see text). The blue arrows indicate the transition dipole moments and their relative alignment. At the bottom of the figure, the effect of the aggregation on the absorption spectrum over the wavelength λ is depicted schematically.

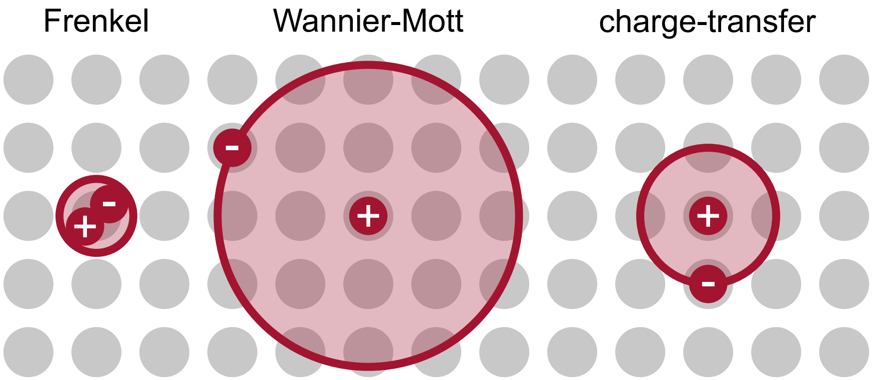

Figure 2.2: Schematic illustration of bound pairs of electrons (-) and holes (+) on a periodic lattice of molecules or atoms. The electron-hole distance (indicated by a red circle) is smaller than the lattice constant for a Frenkel exciton, whereas it is larger for a Wannier-Mott exciton. In a charge-transfer exciton, electron and hole are located on adjacent lattice sites. Adapted with permission from Pope *et al.* [30].

Figure 2.3A. In case of an exciton, there are two unpaired electrons and the total spin quantum number is either $S = 1/2 - 1/2 = 0$ or $S = 1/2 + 1/2 = 1$. The first case has a multiplicity of 1 and is called a *singlet* ($M_S = 0$), whereas the second case has a multiplicity of 3 and is called a *triplet* ($M_S = -1, 0, +1$). These states are visualized in Figure 2.3B and Figure 2.3C, respectively. When two excitons interact, there are four unpaired electrons involved that form singlet ($S = 0$), triplet ($S = 1$) and quintet ($S = 2$) states (see also section 2.1.8).

It is instructive to note that both singlet and triplet state share the same electron configuration. Yet, due to their spin alignment, their energy and wavefunction differ and they are two distinct excited states. This highlights the importance of not confusing orbitals or configurations with states.

Most organic molecules are in a singlet ground state (with molecular oxygen being a notable exception), denoted as S_0. As electronic transitions that change the spin multiplicity are forbidden (the selection rule is $\Delta S = 0$), absorption of a photon leads to an excited singlet state S_n. Due to nonradiative internal conversion,

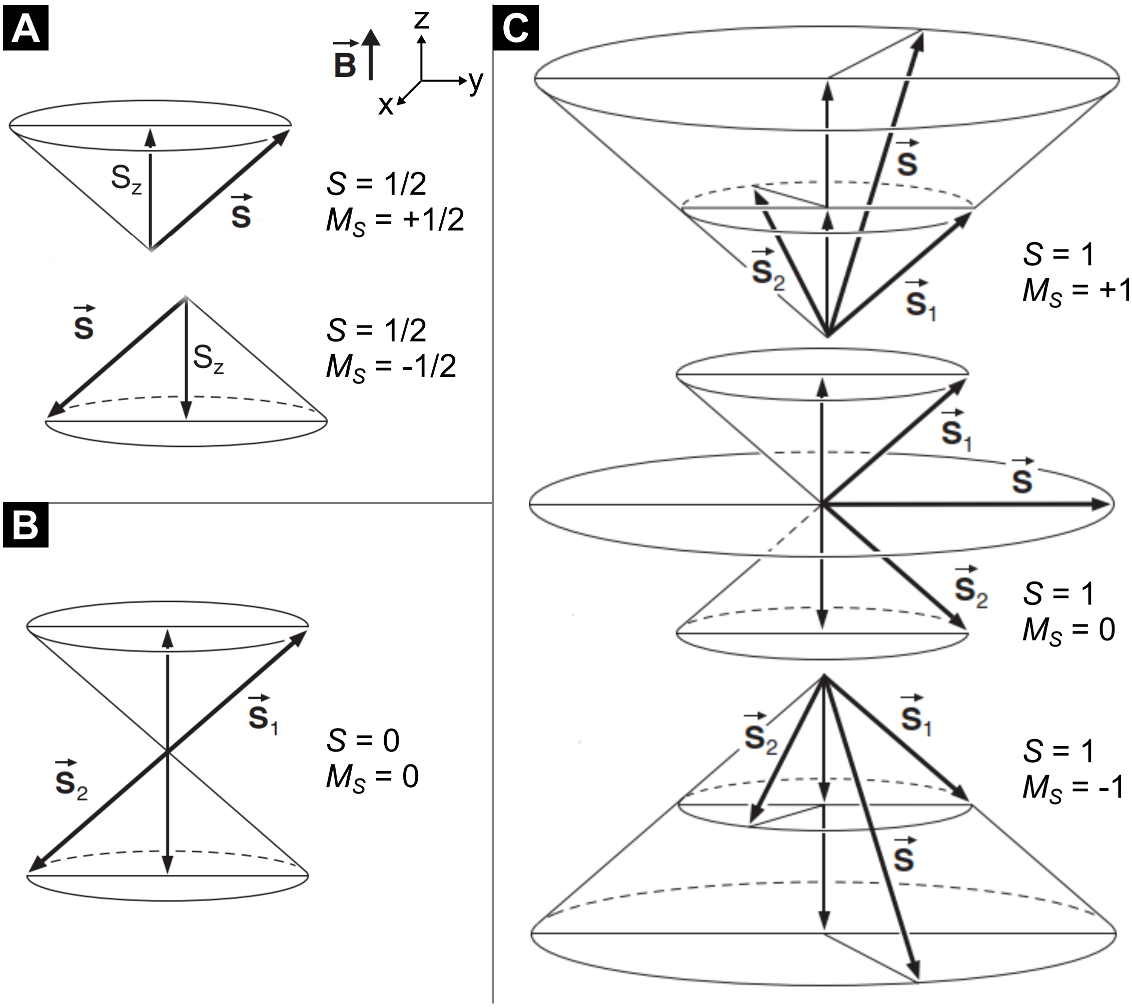

Figure 2.3: Precession of the spin vector $\vec{S}$ about a magnetic field $\vec{B}$ in the z-direction. **(A)** The two components of the doublet state of a single unpaired electron (a radical). **(B)** The singlet state and **(C)** the three components of the triplet state for two unpaired electrons (e. g. an exciton). Adapted with permission from Gerson & Huber [27].

this state quickly transitions to the lowest excited singlet state S_1 on a typical timescale of picoseconds. This state decays radiatively back to the ground state. The corresponding emission is called *fluorescence*, with typical lifetimes on the order of 10 ns. A conversion between singlet and triplet states is spin-forbidden. However, the transition from excited singlet to triplet state $S_1 \rightarrow T_1$ – known as intersystem crossing (ISC) – can be enabled if the change in spin angular momentum of an electron can be compensated by an opposite change in orbital angular momentum (spin-orbit coupling). The presence of heavy atoms (such as palladium) can facilitate this. As the return to the singlet ground state is again spin-forbidden, the rate of the radiative transition $T_1 \rightarrow S_0$ (called *phosphorescence*) is small. Hence, the triplet state's lifetime is typically long and can range from hundreds of microseconds up to several minutes. Furthermore, exchange interaction leads to an energy difference between singlet and triplet states.

A Jablonski diagram illustrating the transitions between exciton states is shown in Figure 2.4A. The respective configurations are depicted in Figure 2.4B. The Coulomb interaction leads to an increase in the HOMO and a decrease in the LUMO of the singlet state. The exchange interaction has a similar additional effect on the triplet's frontier orbitals.

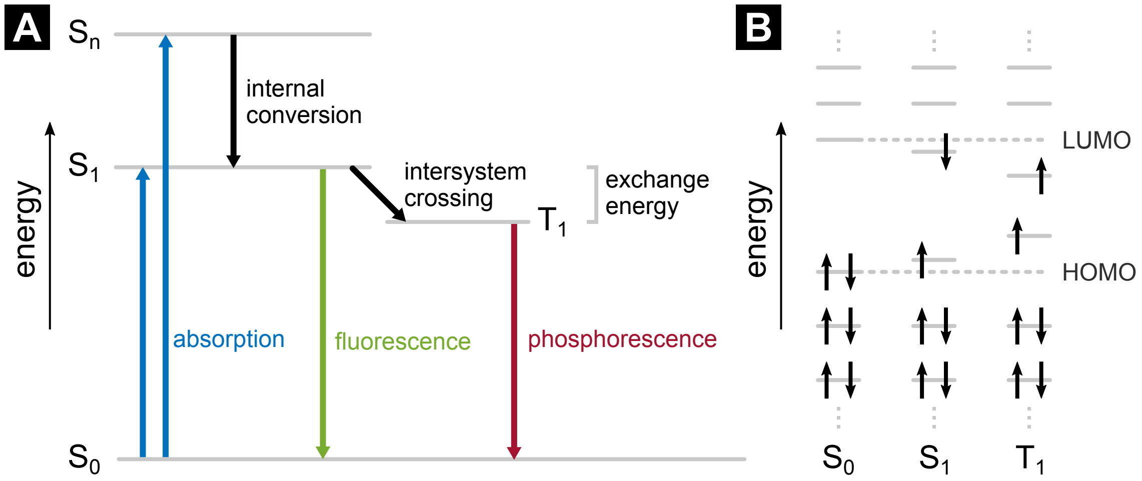

Figure 2.4: Energy levels in an organic molecule. **(A)** Simplified Jablonski diagram of the radiative and nonradiative transitions between exciton states. **(B)** Orbital configuration of a singlet ground state and excited singlet and triplet states. Only the dominant configuration of each state is shown and only one of the three triplet configurations is depicted. The effect of Coulomb and exchange interactions on the HOMO/LUMO energies is indicated for the excited states.

2.1.5 Zeeman Splitting

The magnetic moment $\vec{\mu}_e$ of an electron is proportional to the spin vector

$$\vec{\mu}_e = \frac{g_e(-e)}{2m_e}\vec{S}\,, \tag{2.3}$$

where g_e is the so called g-factor ($g_e = 2.0023$ for a free electron), $e = 1.6022 \times 10^{-19}$ C is the elementary charge, and $m_e = 9.1096 \times 10^{-31}$ kg the electron mass [27]. This magnetic moment enables interaction with an external magnetic field $\vec{B}$. The interaction energy E for a field in z-direction is

$$E = -\vec{\mu}_e \cdot \vec{B} = g_e \mu_B M_S B\,, \tag{2.4}$$

with the Bohr magneton $\mu_B = \hbar e/(2m_e)$ [27]. Thus, the energies of the spin substates of e. g. doublet or triplet states split according to M_S when an external magnetic field is applied. This is known as the *Zeeman effect*. Notably, even without external field, the three triplet substates are not degenerate. Interaction between the unpaired spins such as dipole-dipole coupling lead to *zero-field splitting*, which depends on the molecular geometry. The effect of an external magnetic field on the energy levels of a doublet, singlet and triplet state are depicted in Figure 2.5.

2.1.6 Exciton Transport Mechanisms

In a perfect, static molecular crystal, excitons can move coherently between lattice sites until they decay. However, energetic disorder in the crystal as well as scattering at phonons (which occur in the crystal at non-zero temperatures) lead to exciton localization and a loss of coherence. In this case, excitons motion in the molecular crystal is an incoherent process and can either occur via a emission and absorption of a photon (*trivial transfer*), nonradiative energy transfer (*Förster* process) or an electron exchange (*Dexter* process). The three mechanisms are illustrated in Figure 2.6 for exciton transport from a donor molecule D to an acceptor molecule A.

In case of trivial transfer, the excited donor decays to the ground state and emits a photon, which in turn is absorbed by the acceptor. This two-step process requires overlap of the donor emission spectrum with the

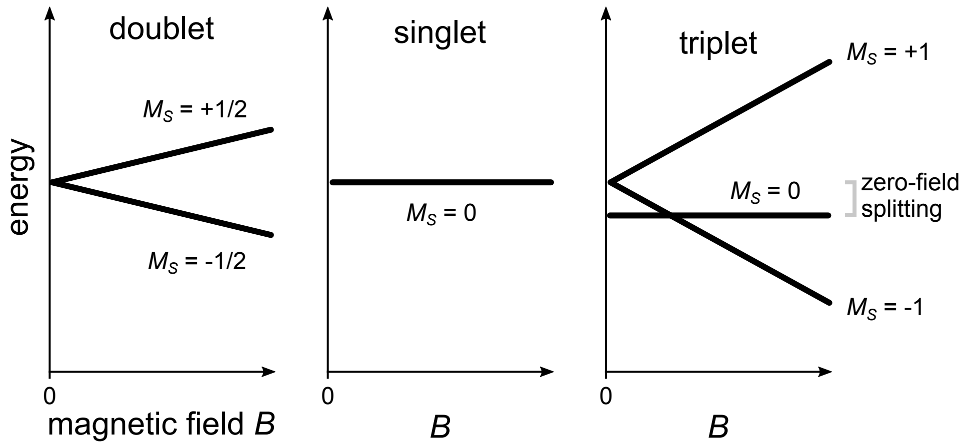

Figure 2.5: Effect of an external magnetic field on doublet, singlet, and triplet energy levels (Zeeman effect).

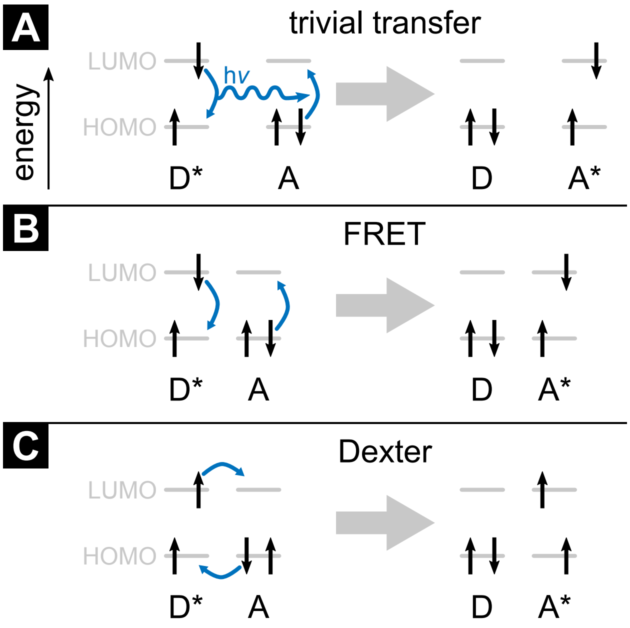

Figure 2.6: Visualization of exciton transport from an excited donor molecule D^* to an acceptor molecule A via **(A)** trivial transfer, **(B)** Förster resonance energy transfer (FRET), and **(C)** via the Dexter exchange mechanism.

acceptor absorption spectrum. No quantum chemical coupling of D and A is necessary. As this type of energy transfer can cover large distances, it is frequently encountered in dilute solutions.

In more dense materials where the molecules are in close proximity, nonradiative exciton transfer occurs. For molecules that are coupled via dipole-dipole interaction, FRET leads to simultaneous de-excitation of D and excitation of A, effectively moving the exciton state between molecules (see Figure 2.6B). The rate of this energy transfer can be expressed as

$$k_{\mathrm{FRET}} = \frac{1}{\tau_{\mathrm{D}}} \left(\frac{R_0}{R} \right)^6 , \tag{2.5}$$

where τ_D is the excited state lifetime of the donor in absence of the acceptor, R is the distance between D and A, and R_0 is the so called *Förster radius* [26]. At $R = R_0$, the probability of FRET and (non-)radiative decay are equal. Typical R_0 values are in the range of 1 nm to 4 nm. The Förster radius depends on the dipole-dipole orientation, the donor's quantum yield, and the spectral overlap integral J between donor emission and acceptor absorption.

Dexter transport occurs when the coupling between D and A is not due to dipole-interactions but caused by an exchange interaction. Here, an excited electron (e. g. in the LUMO) is transferred from D to A, while simultaneously a HOMO electron transfers from A to D (see Figure 2.6C). The transfer rate is

$$k_{\mathrm{Dexter}} \propto J \exp\left(-\frac{2R}{L}\right), \tag{2.6}$$

where L is the sum of the donor's and acceptor's van-der-Waals radii [26]. For Dexter transport to occur, overlap of the quantum mechanical wavefunctions of D and A is required.

FRET and Dexter transport can be present in a material at the same time. Because of the shorter range of the Dexter interaction, energy transfer occurs preferentially via FRET for distances above 1 nm. However, in a FRET process, the ground and excited states involved need to be of the same spin multiplicity. This is the case for a singlet exciton, but a triplet exciton cannot be transferred to an acceptor in a singlet ground state via FRET. Therefore, triplet transport is usually a Dexter process.[2]

2.1.7 Exciton Diffusion

In absence of an external gradient such as an electromagnetic field[3] or a temperature or concentration difference, a particle's motion is undirected and can be described as a random walk. The average distance a particle has traveled in the time t after its creation can be expressed as

$$L = \sqrt{2ZDt}\,, \tag{2.7}$$

where Z is the dimensionality of the diffusion process (e. g. $Z = 3$ for 3D diffusion). The factor D is known as the *diffusion coefficient*.

In a molecular crystal with lattice spacing a, Equation 2.7 allows to calculate the time t_{hop} it takes an exciton to perform a single "hop" between molecules by setting $L = a$. The hopping rate $k_{\mathrm{hop}} = t_{\mathrm{hop}}^{-1}$ is then given by

$$k_{\mathrm{hop}} = \frac{2ZD}{a^2}\,. \tag{2.8}$$

In case of pure FRET or Dexter transport, k_{hop} can be equated to k_{FRET} or k_{Dexter} from above (Equation 2.5 and Equation 2.6).

During an exciton's lifetime τ, the average displacement due to diffusion is given by Equation 2.7 as

$$L_{\mathrm{D}} = \sqrt{2ZD\tau}\,. \tag{2.9}$$

This distance is known as the *diffusion length*. An upper limit for the diffusion length of singlet excitons was calculated by Yost *et al.* [5] as $L_{\mathrm{D,S,max}} = 230\,\mathrm{nm}$. The reason for this limit is that the FRET transfer rate increases with the transition dipole moment μ ($k_{\mathrm{FRET}} \propto \mu^4$), but so does the radiative decay rate, which reduces the lifetime ($\tau \propto \mu^{-2}$). Hence, there exists an optimal value for μ which results in a maximum diffusion length.[4] Typical singlet diffusion lengths are in the range of 2 nm to 20 nm, which is well below the fundamental limit [6]. In contrast, no intrinsic limit of the diffusion length exists for triplet excitons because Dexter transport does not rely on dipole interactions. Additionally, the longer lifetime of triplets leads to larger diffusion lengths, which can be well above 100 nm [6]. Moreover, even longer triplet exciton diffusion distances

---

[2] Spin-orbit coupling can lead to a "mixing" of singlet and triplet wavefunctions, which enables FRET for triplet excitons. This is relevant e. g. in organometallic compounds.

[3] Notably, an exciton is electrically neutral and therefore not affected by external electric fields.

[4] This limit exists for the incoherent transport of singlets. Exciton delocalization and coherent transport can lead to significantly longer singlet transport distances of 1 µm to 3 µm [7–9] and even 20 µm in a quantum wire cooled to 10 K [10]. However, these reports consider single nanofibers or nanowires and have not yet been scaled up to macroscopic films.

have been reported, such as 1.6 µm (3D diffusion) in an anthracene-based MOF [31], 1.7 µm to 3.9 µm in a ladder-type conjugated polymer [32], and 4 µm along one crystal axis in a rubrene single crystal [12].

2.1.8 Triplet-Triplet Annihilation

During their diffusion, two triplets can collide an form an encounter complex. Depending on the total spin S_{TT} of this complex, either a singlet, triplet or quintet state is formed:

$$\mathrm{T}_1 + \mathrm{T}_1 \rightarrow (\mathrm{TT})^* \rightarrow \begin{cases} \mathrm{S}_1 + \mathrm{S}_0 + \text{heat, if } S_{\mathrm{TT}} = 0 \\ \mathrm{T}_1 + \mathrm{S}_0 + \text{heat, if } S_{\mathrm{TT}} = 1 \\ \mathrm{Q}_1 + \mathrm{S}_0 + \text{heat, if } S_{\mathrm{TT}} = 2 \end{cases} \tag{2.10}$$

There are 3^2 possible combinations of spin states: one results in a singlet, three in a triplet and five in a quintet. Therefore, the probability of forming a quintet should be highest. However, the quintet state is usually higher in energy than two times the triplet energy and thus not accessible. Regardless, the probability that one triplet exciton remains after the encounter is three times as high as for the case where a singlet remains. As in both cases the number of triplet excitons is reduced in the system, this bimolecular process is called *triplet-triplet annihilation* (TTA).

A general rate equation for triplet excitons that can decay both through monomolecular and bimolecular decay channels is given by

$$\frac{\mathrm{d}[T]}{\mathrm{d}t} = -k_{\mathrm{GS}}[T] - f\gamma(t)[T]^2, \tag{2.11}$$

where $[T] = [T](t)$ denotes the triplet concentration, and k_{GS} the combined rate of all monomolecular decay processes to the ground state, such as photoluminescence (PL). The factor f depends on the expectation value for the number of remaining triplets after a pair encounter (e. g. $f = 1$ when exactly one triplet survives every encounter). Finally, $\gamma(t)$ is the bimolecular TTA rate coefficient.

Interestingly, the time-dependence of $\gamma(t)$ is related to the dimensionality of the diffusion process. When triplets can diffuse in all three spatial direction, the TTA rate coefficient is given by [33, 34]

$$\gamma_{3\mathrm{D}}(t) = 8\pi DR\left(1 + \frac{R}{\sqrt{2\pi Dt}}\right). \tag{2.12}$$

This model assumes that two triplets interact as soon as their distance is closer than the interaction radius R. This distance is typically on the order of the lattice constant in a crystal.

If the diffusion of triplets is restricted to a single dimension, $\gamma(t)$ is given by [34, 35]

$$\gamma_{1\mathrm{D}}(t) = \frac{1}{an}\sqrt{\frac{8D}{\pi t}} = \frac{\gamma_0}{\sqrt{t}}, \tag{2.13}$$

where a is the distance between molecules along the transport direction and n is the 3D concentration of molecules. The experimentally accessible parameter γ_0 can be used to calculate the diffusion coefficient:

$$D = \frac{\pi}{8}\left(\gamma_0 an\right)^2. \tag{2.14}$$

2.2 Porphyrin

Often called “the pigments of life”, porphyrins are a versatile class of molecules that is at the center of many natural processes such as photosynthesis in plants (in the form of chlorophylls) or oxygen transport in the blood of most vertebrates (in the form of hemes). As nature selected these molecules after billions of years of evolutionary competition, porphyrins clearly have beneficial physical and chemical properties, which could be used in the creation of novel organic systems, e. g. for artificial light-harvesting systems. This section describes some basic derivatives of this class, their optical properties and presents some examples of how porphyrins have been put to use – either by nature itself or by scientists in the lab.

2.2.1 Types of Porphyrins

The most basic porphyrin is porphin.[5] It is a macrocyclic tetrapyrrole, which means it is a molecule that consists of a conjugated ring of four pyrroles in four-fold symmetry. A metal ion can be bound in the molecule's center. An unmetalated porphyrin is labeled *free-base* (FbP) and has a lower symmetry than its metalated counterpart. Reduction of one peripheral double bond leads to chlorin,[6] which forms the macrocycle of chlorophyll. Reducing another double bond yields – depending on the position of the reduced bonds – bacteriochlorin or isobacteriochlorin. These molecules are shown in Figure 2.7. More complex porphyrins are formed by modification of these fundamental molecules such as attachment of substituents. As an example, Figure 2.7 also shows bacteriochlorophyll *a*, which is central to the photosynthesis mechanism in purple bacteria (see page 15).

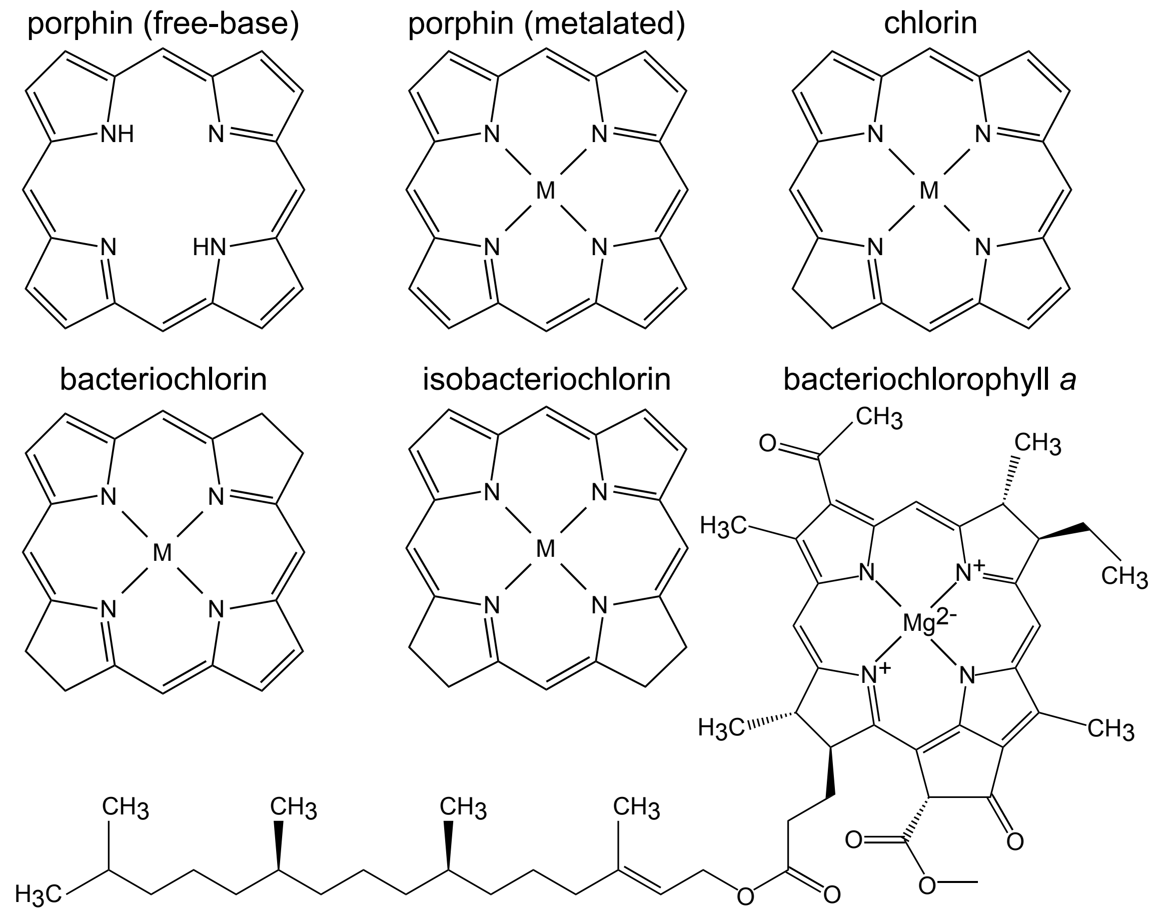

Figure 2.7: Different porphyrins. The letter M denotes the position of a metal ion. Please note that porphin, chlorin and the bacteriochlorins differ in their number of double bonds. The structure of bacteriochlorophyll *a* is taken from the ChEBI database [36, 37].

---

[5] Sometimes also spelled porphine.

[6] Not to be confused with chlorine!

2.2.2 Optical Properties of Porphyrin

The electronic properties of porphyrins can be described by the four-orbital model established by Gouterman [38, 39]. It considers the four frontier orbitals b_1, b_2, c_1 and c_2 as depicted in Figure 2.8A. In a metalloporphyrin (with four-fold symmetry), the HOMO levels b_1 and b_2 are nearly degenerate and the LUMO levels are exactly degenerate (see Figure 2.8B). The resulting states split due to configuration interaction into a low-energy state with vanishing transition dipole moment and a high-energy state with a large transition dipole. The corresponding optical absorptions are called the *Q-band* and the *Soret band*[7], respectively. They are shown in Figure 2.8C.

In chlorin, the molecule's symmetry is lowered, which lifts the degeneracy of the b and c orbitals. Furthermore, the y polarization component of the Q-band (after the convention in Figure 2.8) is no longer forbidden by configuration interaction and becomes significant. It is also shifted to lower energies, whereas the y-component of the Soret absorption is blue-shifted. As the x-polarized transitions $b_1 \rightarrow c_2$ and $b_2 \rightarrow c_1$ remain (nearly) degenerate, the Q_x band is still suppressed. Going to bacteriochlorin continues the trend (blue-shifted Soret band, red-shifted Q_y band). These changes can be seen well in the absorption spectra in Figure 2.9.

The central metal ion in metalloporphyrins influences their electronic properties. For example, the metalation affects the shape of the frontier orbitals slightly and influences their energies [42]. As another example, the ISC yield depends on the mass of the central atom. Accordingly, it increases from free base over zinc- to palladium-metalated porphyrin [43]. Notably, the ISC yield was determined as 1 in several palladium porphyrin derivatives [43, 44].

---

[7] Named after Jacques-Louis Soret who first described this absorption peak in 1883 [40]. Sometimes also called B-band.

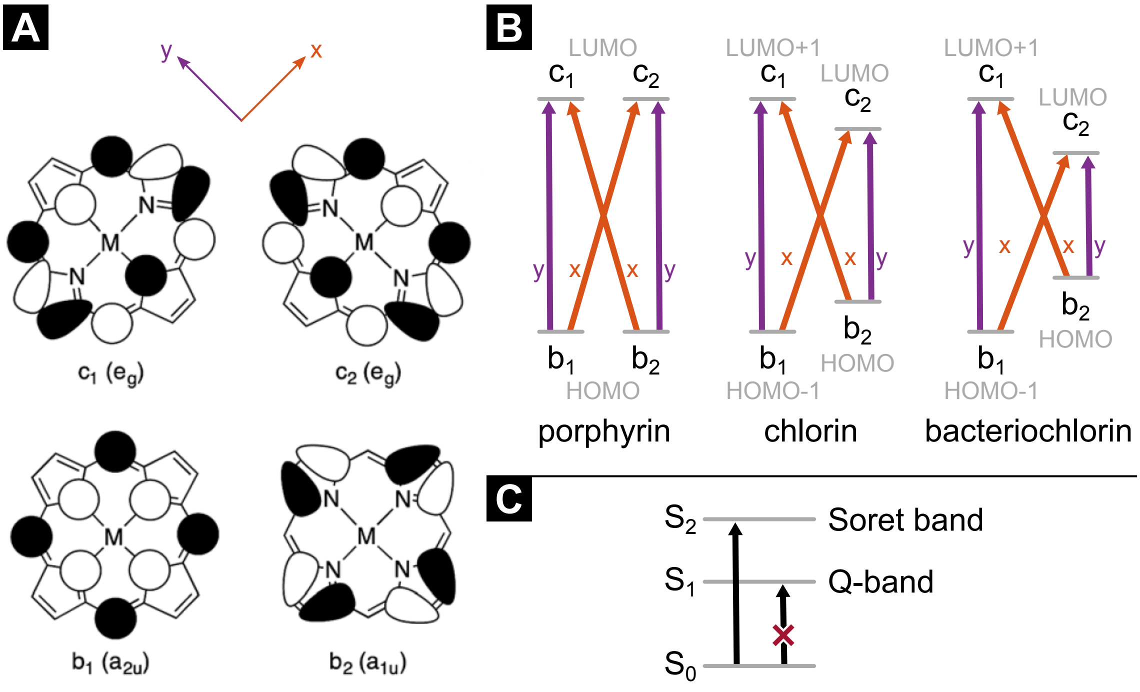

Figure 2.8: The four orbital model. **(A)** The frontier orbitals of porphyrin, labeled after the convention introduced by Gouterman [38]. Reproduced with permission from Otsuki [41]. **(B)** Schematical electronic transitions between the orbitals in metallated porphyrin, chlorin and bacteriochlorin. **(C)** State diagram of the resulting electrical transitions. The Q-band transition is forbidden in porphyrin, but partially allowed in chlorin and bacteriochlorin.

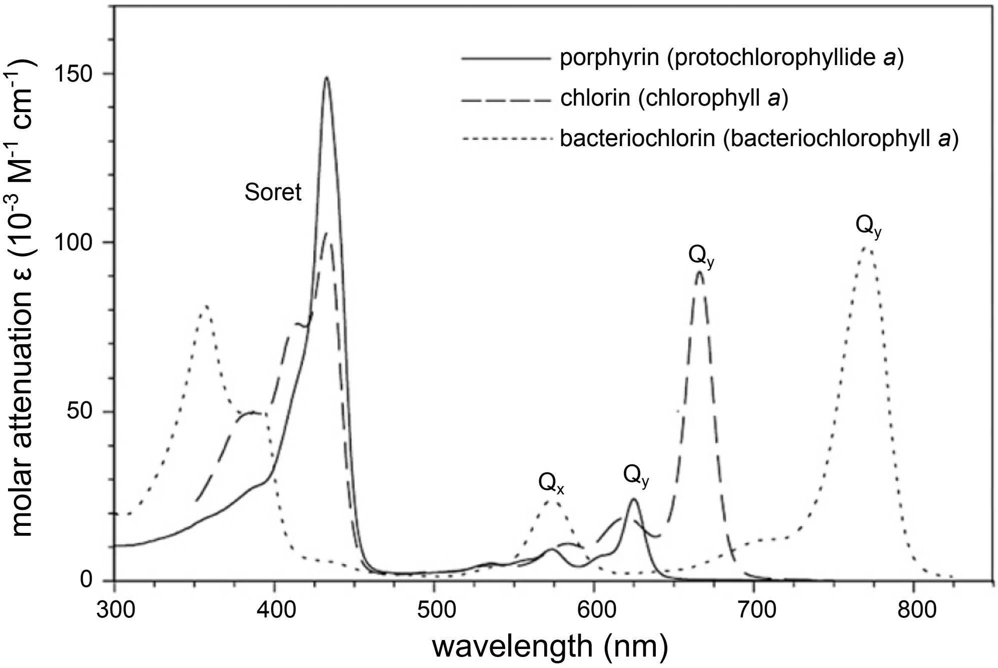

Figure 2.9: Absorption spectra of naturally occurring chlorophylls with porphyrin, chlorin and bacteriochlorin macrocycles in THF. Adapted with permission from Otsuki [41] and Wang & Tamiaki [42].

2.2.3 Porphyrins in Light Harvesting

Photosynthesis in phototrophical plants and bacteria is driven by absorption of light in antenna chromophores followed by energy transfer to a reaction center where charge separation occurs. This allows the plant to store chemical energy. To increase the yield of this process, hundreds of antennas are associated with one reaction center to increase the transfer frequency of excitons to the reaction center [41]. Exciton transport from the antennas is required to be efficient.

The LH2 Complex in Purple Bacteria

As just one of many possible example systems, the light harvesting complex LH2 in purple bacteria shall be summarized here (based on Otsuki [41]). The LH2 complex of *Rhodopseudomonas acidophila* is depicted in Figure 2.10A. This protein complex contains a ring of nine building units, which in turn contain three bacteriochlorophylls (BChl *a*, see Figure 2.7) and a carotenoid. The BChl *a* chromophores are labelled B800 and B850, according to the wavelength of their Q-band absorption peak (800 nm and 850 nm, respectively).

The distance between B800 chromophores (measured between Mg atoms) is 21.3 Å and they are isolated. In contrast, the B850 molecules are 9.2 Å apart and they are electronically coupled, which leads to a delocalization of the exciton over 2-6 chromophores. Hence, the time constant for exciton transport among B800 molecules is 500 fs, whereas it is 100 fs to 200 fs for the B850 ring. Transfer between the rings (from B800 to B850) occurs in around 1.2 ps. From here the excitons can transfer to another similar light harvesting complex, LH1, which is also a ring of bacteriochlorophylls (B875). A final step from the LH1 complex to the reaction center occurs on the timescale of 35 ps. The whole process is depicted in Figure 2.10B. The efficiency of the whole process is high, as the lifetime of the excited state (1 ns to 2 ns in LH1) is long compared to the individual steps.

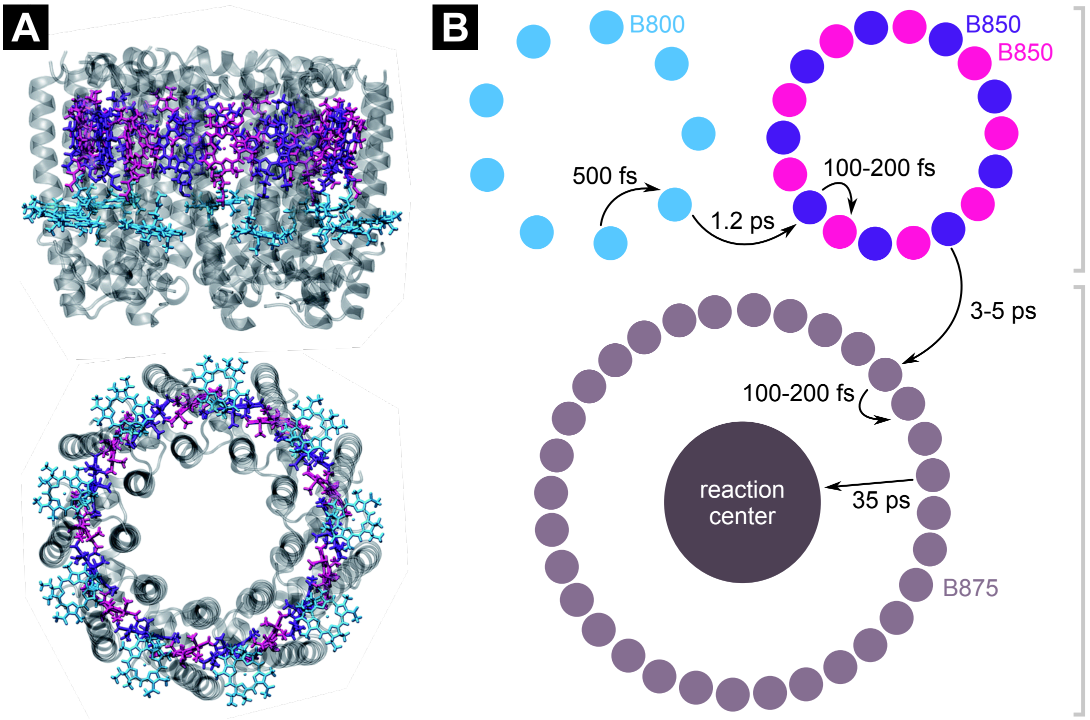

Figure 2.10: Light harvesting in purple bacteria (*Rhodopseudomonas acidophila*). **(A)** Side and top view of the LH2 complex. The B850 bacteriochlorophyll *a* molecules are colored pink and purple due to their different local environments. The B800 molecules are colored cyan. Reprinted with permission from Caprasecca *et al.* [45]. **(B)** Time constants in the LH2 and LH1 complexes. Adapted with permission from Fleming & Grondelle [46] and Mirkovic *et al.* [47].

Synthetic Approaches

Synthetic light harvesting can mimic nature's approach of photon absorption by antenna chromophores and exciton transfer. Instead of using a reaction center and additional biochemical steps to store chemical energy, electrodes can be used to extract electricity. A multitude of different approaches has been examined, especially in the realm of supramolecular structures, such as self-assembled porphyrin rings and boxes, aggregates and MOFs. Porphyrins have been even attached to viruses, DNA or existing natural light harvesting complexes. An excellent overview is given in a review by Otsuki [41].

This thesis will focus on porphyrin-based MOFs. An overview of existing work on exciton transport in such materials is given in section 2.3.2 on page 17.

2.3 Metal-Organic Frameworks

As order is beneficial for exciton transport, it is obvious that crystalline chromophore assemblies are a promising research direction. One way to create such highly ordered structure is spontaneous self-assembly of molecular building units into coordination networks. In case of *metal-organic frameworks* (MOFs), these units are metal-based nodes and organic ligands (known as *linkers*). Together, they form nanoporous[8] crystalline networks via coordination bonds. The choice of ligands allows tuning of the network geometry. One way of applying the material is by employing its porosity via incorporation of "guest" molecules into the pores (host-guest architecture, also known as "guest@MOF"), putting these guests in a well-controlled local environment. The first stable porous MOF (known as MOF-5) was synthesized by Li *et al.* in 1999 [49]. Since then, the versatility and abundance of realized MOF structures has enabled a wide range of applications, such as gas storage [50–52],

---

[8] The presence of voids in the material is a requirement for a coordination network to be called MOF [48].

separation [25, 51], catalysis [25, 53, 54] as well as electronic conductivity [54, 55], data storage [54, 56, 57], photon upconversion [58–61], and light harvesting [25, 50, 54, 62–67].

2.3.1 Surface-Anchored Metal-Organic Frameworks

Typical MOFs are micro- or nano-crystalline powders. They can be deposited as films to coat surfaces [68]. However, the deposited crystallites do usually not have a common orientation. To overcome this issue and achieve a higher degree of order, there exist preparation methods that result in MOFs which are directly attached to the substrate. These materials are known as *surface-anchored metal-organic frameworks* (SURMOFs). How the structure can be attached to a surface depends on the substrate and the building unit's chemistry. For example, the first reported SURMOF was connected to a substrate functionalized with a self-assembled monolayer (SAM) [69], and this method remains widely used [70]. Other methods include oxygen plasma treatment of substrates with a native oxide layer to form hydroxyl groups [70, 71].

The deposition of the SURMOF's constituents has been performed by a wide range of different methods, among them direct crystallization, spray-coating, dip-coating, spin-coating, evaporation and electrochemical methdods [70, 72]. Exemplarily, the deposition process by liquid-phase epitaxy (LPE) shall be described here. The metal nodes and the linker molecules are prepared in separate solutions. The previously functionalized/activated substrate is then coated in one of the solutions, e. g. the metal node solution. In this case, the metal nodes attach to the functional groups on the surface. In a rinsing step, residual unreacted building units are removed. Now the substrate is coated with the second solution and the organic linkers attach themselves to the already present metal centers. This is followed by another rinsing step. The whole process is repeated over several cycles (shown in Figure 2.11) to build up the SURMOF. This process allows to control the film thickness by the number of deposition cycles [73]. Furthermore, it is easily automated and scaled up to coat large substrates [74].

SURMOF growth by LPE is not an ideal layer-by-layer process, which means that more than one molecular layer can be grown per deposition cycle. For example, Summerfield *et al.* observed growth rates of 5 to 10 layers per cycle in a HKUST-1 SURMOF [73]. This has been linked to the solution-mediated formation of secondary building units from weakly absorbed precursor molecules that are not removed by the rinsing step [75]. Especially when using a spraying technique – as opposed to a dip-coating process – larger growth rates can be expected, as a sprayed solvent film is less effective in removing residual precursors than immersion of the substrate in solvent [74].

2.3.2 Exciton Transport in Porphyrin-Based MOFs and SURMOFs

This section gives an overview of relevant developments related to energy transport in MOFs and SURMOFs, with special focus on porphyrin-based materials.[9]

An early example of energy transfer in a porphyrin-based MOF is the work of Lee *et al.* [63]. They presented a pillared-paddlewheel MOF wherein zinc porphyrin (ZnP) chromophores are connected by boron dipyrromethene (BODIPY) pillars. Upon selective excitation of the BODIPY molecules, they observed singlet exciton transfer to the ZnP chromophore (over a distance of around 16 Å) and subsequent ZnP fluorescence.

Son *et al.* presented a ZnP-based MOF (named DA-MOF) and observed singlet exciton transfer between adjacent parallel as well as coplanar porphyrin linkers [64]. They calculated anisotropic transfer rates, depending on the linker-to-linker distance in each transport direction. The fastest singlet transport was found

---

[9] An attempt to present the complete literature on porphyrin MOFs is outside the scope of this thesis. To give some perspective on the size of this growing field: Farha *et al.* counted 40 publications with 81 reported 2D and 3D porphyrin-based MOFs back in 2011 [76]. As of April 2019, a search on Web of Science yields over 400 publications for the search query “`TOPIC: (porphyrin "metal-organic framework") OR TOPIC: (porphyrin SURMOF) OR TOPIC: (porphyrin MOF)`” in the Web of Science Core Collection, with roughly half of these publications falling in the time range between the years 2017 and 2019.

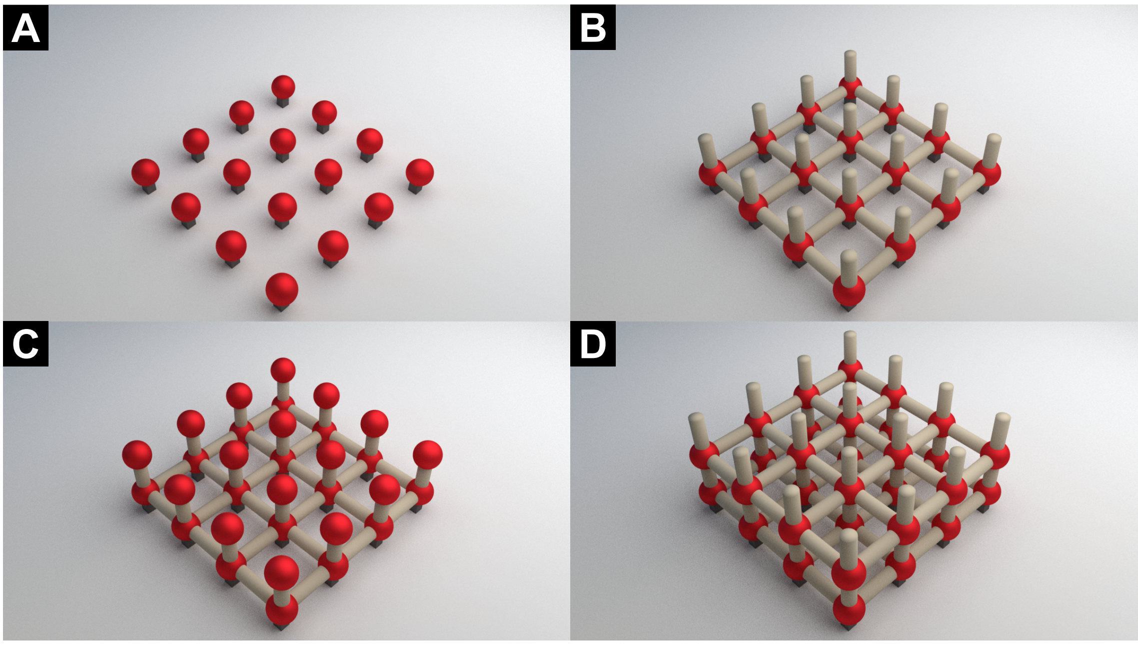

Figure 2.11: Schematic drawing of the deposition steps in the preparation of a SURMOF. **(A)** Metal nodes (red spheres) attach to an activated substrate (with the dark blocks representing for example hydroxyl groups). **(B)** Linker molecules (white rods) attach to the metal nodes. This cycle is repeated by **(C)** deposition of metal nodes and **(D)** linker molecules. Further cycles increase the SURMOF film thickness.

between adjacent (11 Å apart) parallel ZnP linkers with a hopping rate of $k_{\text{hop}} = 1.0 \times 10^{11}\,\text{s}^{-1}$ and a diffusion length of $L_D = 38\,\text{nm}$, whereas the largest L_D was calculated for the collinear direction as $L_D = 58\,\text{nm}$. Notably, in order to improve exciton transport, they suggested to shrink the inter-chromophore distance or to utilize long-lived triplet excitons instead of singlets. Both suggestions will be addressed in this thesis.

The first porphyrin-based SURMOFs were presented by So *et al.* [62]. They fabricated a ZnP-SURMOF based on the previously reported DA-MOF (see above) as well as a novel FbP SURMOF film. A bipyridine linker is used to form vertical pillars with the porphyrin molecules being oriented parallel to the substrate. To investigate the singlet exciton transport properties, a squaraine dye is attached to the surface of a roughly 35 nm thick DA-MOF film. This leads to a quenching of the ZnP fluorescence. Excitation of the ZnP linker leads to almost exclusive emission from the squaraine dye, highlighting the efficiency of vertical singlet transport in this thin film.

The FbP porphyrin SURMOF from that study was used again by Goswami *et al.* [77]. Instead of attaching a dye, two additional deposition cycles of palladium porphyrin (PdP) linker were performed, leading to a SURMOF heterojunction. Again, the top layer acts as a quencher an shows efficient vertical singlet exciton transport in the film. The novel concept in this study was the in-place substitution of the bipyridine pillars with shorter pyridine molecules, which leads to the collapse of the 3D structure into crystalline MOF layers. The reduced distance between the layers results in an increase of the number of layers traveled by a singlet exciton from 6-8 (before the collapse) to 9-11 (afterwards). However, taking into account the layer-to-layer spacing (14.7 Å before, 6.9 Å after), the corresponding distance traveled (L_D) actually gets shorter. This is due to the fact that, although the layer distances are reduced by the SURMOF collapse, the nearest-neighbor distance between porphyrin linkers remains similar (14.7 Å before, 14.3 Å after) because adjacent layers are shifted laterally.

The impact of the MOF topology on the material's photophysical properties was investigated by Deria *et al.* [78]. They fabricated two MOFs with different network structures but the same linker chromophores (FbP and ZnP). The different geometry in the two MOFs leads to different electronic interaction among linkers.

Stronger interaction results in a more pronounced redshift in the absorption spectra and a shorter excited state lifetime. These findings underline the tunability of physical MOF properties by choice of the network topology alone.

Several reports exist of porphyrin-MOF based solar cells. Liu *et al.* fabricated SURMOFs based on either FbP or PdP linkers, which show photovoltaic activity when used in a liquid electrolyte PV device. The SURMOF is comprised of closely packed free-standing 2D sheets. Therefore, exciton/charge transport to the electrodes has to occur inside the sheets, which might not be the ideal transport direction.[10] Still, photoconversion efficiencys (PCEs) of 0.2 % and 0.45 % could be observed for the FbP and PdP SURMOFs, respectively. The same group fabricated also an all-solid-state solar cell based on the same SURMOF structure (albeit with ZnP linkers) [66]. The best device exhibits a PCE of 0.017 %. The current record for the best-performing porphyrin-MOF based PV device is held by Gordillo *et al.* [65]. They presented a MOF-sensitized liquid electrolyte solar cell based on a solvothermally grown pillared ZnP-MOF film. The PCE in the device was reported as 0.8 %.

Another interesting application of a porphyrin SURMOF was presented by Oldenburg *et al.* in the form of a SURMOF heterostructure for photon upconversion [59]. The heterostructure is comprised of layers of an anthracene-linker based SURMOF as emitter and a PdP SURMOF as sensitizer (either in an emitter-sensitizer-emitter stack or in an emitter-sensitizer stack). Excitation of the PdP linker leads to the creation of triplet excitons that could be shown to travel across the heterojunction into the emitter SURMOF, where TTA upconversion occurs. As in the aforementioned work of Liu *et al.* [67], PdP triplets are required to move perpendicular to the substrate, that is in the plane of the free-standing sheets, in order to reach the emitter.

2.4 Pump-Prope Spectroscopy

Electronic processes can occur on timescales from several seconds (phosphorescence) over nanoseconds (fluorescence, ISC) down to the femtosecond regime (electron transfer) [79]. Investigation of the latter requires sophisticated measurement techniques, such as femtosecond pump-prope spectroscopy. In the late 1980s, Ahmed H. Zewail pioneered this technique as a method to investigate transition states of chemical reactions and was awarded the Nobel Prize in Chemistry for this work in 1999 [80].

Generally, in pump-probe experiments, a sample is first excited from the ground to an excited state by a *pump* event, for example via illumination with a pulsed laser. After a defined and tunable delay time Δt, a physical property of the excited sample is *probed*, for example transmittance/reflectance of a light pulse. By tuning Δt, the excited state evolution of the sample material can be tracked.

Pump and probe duration need both to be short compared to the timescale of the events under investigation. Hence, to observe excitonic processes using optical spectroscopy, picosecond or even femtosecond light pulses are required.

2.4.1 Transient Absorption Spectroscopy

A special incarnation of the pump-probe technique is *transient absorption spectroscopy* (TAS). This method uses a probe light pulse which is directed through an absorptive sample and detected at a spectrometer. Excitation by the pump light pulse is performed at half the probe frequency. Thus, the detector measures an alternating sequence of transmission spectra that either correspond to a previously excited sample ("pump on" spectra T_{on}) or an un-excited sample in the ground state ("pump off" spectra T_{off}). Notably, this scheme requires the time between two probe pulses to be longer than the excited-state lifetimes in the sample, as otherwise the "pump off" measurement does not represent the material in its ground state.

---

[10] This will be investigated in the results chapter of this thesis, see section 4.2.

Transmission is defined by the incident radiant flux Φ_i and the transmitted flux Φ_t:

$$T = \frac{\Phi_\mathrm{t}}{\Phi_\mathrm{i}} . \tag{2.15}$$

TAS data is usually represented as the *differential transmission*. This is the dimensionless fraction $\Delta T/T$, wherein $\Delta T = T_\mathrm{on} - T_\mathrm{off}$ and T in the denominator is shorthand for T_off. This representation will be used throughout this thesis. A graphical summary of the measurement scheme is depicted in Figure 2.12A. The practical realization of a TAS setup is described in section 3.5.

As the difference between two measurements is small (typical $\Delta T/T$ values are on the order of 10^{-4}), the measurement is repeated for several (10^2 to 10^4) probe pulse pairs and the individual $\Delta T/T$ values are averaged. An important underlying assumption is that the probe light pulses for the "pump on" and "pump off" measurements are identical in spectrum and intensity. Only then can all differences in transmission be attributed to the pump-induced changes in the sample's photoresponse. Otherwise, probe light fluctuations introduce an error. This is the reason why shot-to-shot measurements as outlined above are often preferred over averaging schemes, wherein a series of "pump on" pulses is averaged ($\overline{T_\mathrm{on}}$), followed by a series of "pump off" pulses ($\overline{T_\mathrm{off}}$) and calculation of $\Delta T/T = (\overline{T_\mathrm{on}} - \overline{T_\mathrm{off}})/\overline{T_\mathrm{off}}$.

Figure 2.12B illustrates the possible signals in a TAS spectrum, which are explained below.

Ground-state bleach (GSB): The ground state is depopulated by the pump pulse and $T_\mathrm{on} > T_\mathrm{off}$. Therefore, a positive feature is observed in the TAS spectrum. Its spectral shape corresponds to the ground state absorption of the sample.

Photoinduced absorption (PIA): A negative signal occurs when the photo-excited sample shows an increased absorption, that is $T_\mathrm{on} < T_\mathrm{off}$. This can be caused by the presence of excited states that can absorb an additional photon to reach higher excited states (excited state absorption), or by absorption of charged molecules after dissociation of the excited state (polaron absorption).

Stimulated emission (SE): Probe light photons can stimulate emission from the S_1 state. This luminescence leads to more light reaching the detector during the "pump on" measurement. Because $T_\mathrm{on} > T_\mathrm{off}$, the corresponding TAS feature is positive. The SE signal's spectrum and lifetime correspond to the fluorescence.

An important advantage of TAS is that the dynamics of non-emissive excited states can be monitored.

Besides $\Delta T/T$, TAS data is commonly represented as differential optical density, ΔOD, or differential absorbance, ΔA. Transmission and absorbance are related via the decadic logarithm:

$$A = -\log_{10}(T) , \tag{2.16}$$

and thus the relationship between the differential absorbance $\Delta A = A_\mathrm{off} - A_\mathrm{on}$ and the differential transmission is

$$\Delta A = -\log_{10}\left(\frac{\Delta T}{T} + 1\right) . \tag{2.17}$$

As $\Delta T/T \ll 1$ (typical values are below the percent level), Taylor expansion around $\Delta T/T = 0$ can be performed:

$$\Delta A \approx \underbrace{-\log_{10}(1)}_{=0} - \frac{1}{\ln(10)} \frac{\Delta T}{T} + \ldots , \tag{2.18}$$

which yields a useful linear approximation to convert between the two representations:

$$\Delta A \approx -0.4343 \times \frac{\Delta T}{T} . \tag{2.19}$$

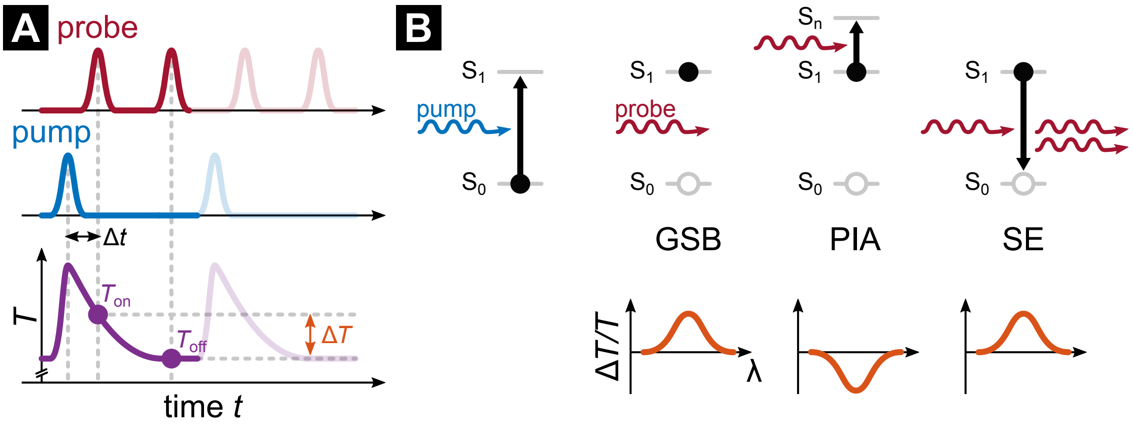

Figure 2.12: Origin and shape of the signal in transient absorption spectroscopy. **(A)** A train of probe pulses is transmitted through the sample. The transmission T is influenced by excitation of the sample into an excited state by a pump pulse. ΔT is calculated from the difference in transmission between a "pump on" and "pump off" probe pulse. Tuning of the delay time Δt allows to measure the excited state kinetics. **(B)** Possible features in a TAS spectrum as described in the text.

For the usual range of TAS signals ($\Delta T/T < 0.01$), this approximation deviates from the exact value by less than 0.5 %.

2.4.2 Light Sources for TAS

As mentioned above, a requirement for pump-probe spectroscopy on picosecond timescales is the availability of femtosecond laser pulses. Light sources that generate such short bursts of intense radiation are also necessary to efficiently harness nonlinear optical effects such as supercontinuum generation. The following brief overview on relevant concepts of textbook laser physics is based on the *Springer Handbook of Lasers and Optics* [81] and *Lasers in Chemistry* [82].

Femtosecond Lasers via Mode Locking

The most common technique for the generation of light pulses on the femtosecond time scale is *mode locking*. In a laser cavity of length L, the round-trip time τ_{RT} of a photon traveling at the speed of light c is

$$\tau_{\mathrm{RT}} = \frac{2L}{c}\,. \tag{2.20}$$

In the cavity, only transverse modes of a wavelength λ can oscillate that fulfill the standing wave condition

$$\frac{2L}{\lambda} = k\,, \tag{2.21}$$

with k being an integer. In terms of frequency f, this becomes

$$\frac{2Lf}{c} = k\,, \tag{2.22}$$

and the frequency difference between two cavity modes is

$$\Delta f = \frac{c}{2L} = \frac{1}{\tau_{\mathrm{RT}}}\,. \tag{2.23}$$

In a free-running laser, the phase between individual modes is arbitrary, which leads to an output in which both intensity and wavelength fluctuate. By introducing a periodic gain or loss with a frequency of $1/\tau$ in the laser cavity, the phase of all lasing modes can be synchronized. This results in intense, short laser pulses that are coupled out of the cavity after each round-trip time. Hence, the repetition rate of the laser is $f_{\mathrm{rep}} = \tau_{\mathrm{RT}}^{-1} = c/(2L)$.

It is instructive to first consider an already mode-locked laser. The different modes are in phase and produce a resonant pulse with a temporal width of τ_{p}, which is shorter than the round-trip time. This pulse performs one round trip in the cavity during τ_{RT}. As a visualization, a shutter can be placed in the cavity that is opened periodically for a short time interval ($\approx \tau_{\mathrm{p}}$). When its frequency matches τ_{RT}, the relative timing of the shutter can be chosen so that the laser pulse oscillates undisturbed. This mode-locked end state is also reached when the same shutter is placed in a free-running cavity. In this case, lasing of out-of-phase modes is suppressed by the modulation. Only one pulse can survive in the cavity, which corresponds to the initial picture of a mode-locked laser.

In *active mode locking*, the periodic loss modulation is performed by an active element, such as an intra-cavity acousto-optic modulator (AOM) or a Pockels cell. The modulation frequency is driven by external electronics and has to match the cavity length precisely. In *passive mode locking*, an optically nonlinear device, for example a saturable absorber, is placed in the cavity. The periodic interaction of the light pulse with the nonlinear material and the corresponding periodic loss lead to a modulation that intrinsically matches the cavity length without the need for external electronics.

The minimal duration of the resulting light pulse, τ_{p}, depends on the number of modes N that contribute to it and their spacing in the frequency domain. As the gain medium restricts which modes are amplified, τ_{p} is ultimately defined by the gain bandwidth Δf_{gain}. Approximately, τ_{p} is given by

$$\tau_{\mathrm{p}} \approx \frac{1}{N\,\Delta f} \approx \frac{1}{\Delta f_{\mathrm{gain}}}\,. \tag{2.24}$$

As an example, the gain bandwidth of an Ar^{+} laser is around 8 GHz [82]. Accordingly, the shortest possible pulses using this material are $\tau_{\mathrm{p}} \approx 125\,\mathrm{ps}$ long. In contrast, titanium-doped sapphire (Ti:Sa) can have a bandwidth of up to 128 THz [82] and a corresponding pulse duration of only $\tau_{\mathrm{p}} \approx 8\,\mathrm{fs}$, which is one of the reasons why it is a commonly used material in femtosecond lasers.

Chirped Pulse Amplification

When trying to amplify an ultrashort light pulse, the high peak power can cause non-linear distortion or damage to the amplifier optics. In order to overcome these problems and enable high-intensity femtosecond pulses, a technique called chirped pulse amplification (CPA) can be employed. It utilizes the fact that ultrashort light pulses have a broad spectral bandwidth. A pair of dispersive elements (such as prisms or gratings) is used to introduce positive or negative group velocity dispersion (GVD). Thus, a variation in frequency over time is introduced, which is called *chirp*. In a an up-chirped signal, the frequency increases over the pulse. Simply speaking, the long-wavelength (red) components of the light pulse arrive before the short-wavelength (blue) components. In a down-chirped pulse the situation is reversed: the blue components arrive first and the red components last. The chirp leads to either stretching or compression of the temporal envelope of the light pulse, depending on the sign of the GVD change. By stretching the pulse, the peak power is reduced and the pulse can be amplified without the aforementioned problems. Afterwards, it is compressed back to its original pulse duration. For this ingenious concept, introduced in 1985 [83], one half of the 2018 Nobel Prize in Physics was awarded to Gérard Mourou and Donna Strickland [84].

White Light Generation

Femtosecond lasers are useful as both pump and probe sources in ultrafast pump-probe spectroscopy. The pump wavelength needs to correspond to an absorption of the investigated material. For a monochromatic probe pulse, only the kinetics (e. g. evolution of a TAS signal over delay time Δt) at this specific wavelength can be measured. By using a spectrally broad probe pulse combined with detection at a fast spectrometer, a wider spectral range can be investigated. One technique to produce very broadband ("white") light pulses is called *supercontinuum generation* or white-light generation (WLG). This effect is a combination of several nonlinear optical effects such as self- and cross-phase modulation, four-wave-mixing and stimulated Raman scattering. As such, it depends strongly on the input laser power, which makes short but intense femtosecond pulses as produced by CPA ideal sources for this technique. Such pulses are sent through a fiber (for example a special photonic crystal fiber) or focused into a crystal (for example sapphire or calcium fluoride), where the nonlinear effect leads to a significant spectral broadening of the pulse that can span multiple octaves.

Q-Switched Lasers

When the physical processes under investigation occur on the nanosecond timescale or above, it is no longer necessary to employ a femtosecond laser as pump source. Pulse durations on the pico- to nanosecond scale may be sufficient in those cases. These can be produced by a *Q-switched laser*.

When a laser cavity is pumped (by a pulsed or continuous wave (CW) source) and the population inversion reaches the laser threshold, stimulated emission prevents further energy storage in the gain medium. This limits the laser's pulse energy. To overcome this, the cavity's quality factor Q can be reduced, which prevents the onset of efficient lasing and a much larger population inversion than before can be reached. Once the gain material is saturated, the Q-factor is switched to a high value and a single pulse of high-intensity laser light is emitted. To reach the maximum laser intensity, several (up to hundreds or even thousands) round-trips are necessary. As an example, one round-trip takes $\tau_{\mathrm{RT}} = 1\,\mathrm{ns}$ in a $15\,\mathrm{cm}$ cavity. Accordingly, typical pulse lengths for Q-switched lasers range from nanoseconds to microseconds.

Similar to the situation in mode-locking, modulation of the Q-value can either be performed actively, for example by placing an AOM or a Pockels cell in the cavity, or passively, by using a saturable absorber material.

3 Methods and Materials

This chapter gives an overview over relevant experimental techniques, setups and devices that are used in this thesis.

3.1 Light Sources

Several lasers are used throughout this thesis and presented in this section.

3.1.1 Femtosecond Pulsed Laser System

The femtosecond laser source used for the TAS setup is a SpectraPhysics Spitfire Pro XP system. The amplifier uses CPA to generate femtosecond pulses. It is pumped by a SpectraPhysics Empower laser and seeded by a SpectraPhysics Tsunami Ti:Sa laser, which in turn is pumped by a SpectraPhysics Millennia CW laser. Simply speaking, the Tsunami provides femtosecond-short but weak pulses that are amplified with the Empower's pulse energy inside the Spitfire unit. In the following, the individual components are presented in more detail.

Pump Laser

The gain medium inside the Empower pump laser is a rod of neodymium-doped yttrium lithium fluoride (Nd:YLF) that is uniformly pumped by diode lasers [85]. The excited neodymium emits infrared laser radiation at 1053 nm, which is frequency-doubled inside the laser cavity in a heated lithium triborate (LBO) crystal to 527 nm. The laser is actively Q-switched by an AOM. The output pulses are 100 ns long and contain an energy of 10 mJ to 20 mJ at a repetition rate of 1 kHz.

Seed Laser

The Tsunami is a mode-locked Ti:Sa laser [86]. The Ti:Sa rod is excited by the Millennia's 532 nm CW output and emits fluorescence at a broad wavelength range from 600 nm to 1000 nm. Inside the folded cavity is a pair of prisms, which disperses the light and spatially spread out the different wavelengths, and a second prism pair which mirrors the first one and reverses the effect. In between the two prism pairs is a slit, whose user-adjustable position determines the center wavelength and whose width affects the spectral bandwidth. As the "standard" mirror set is used, the center wavelength tuning range is 720 nm to 850 nm. An AOM inside the cavity is used to generate a periodic loss. The Tsunami uses regenerative mode-locking, which means that the frequency of the AOM is derived directly from the cavity by measuring the laser light intensity on a photodiode. The usual round-trip time in the Tsunami is $\tau = 12.5\,\text{ns}$, which results in a repetition rate of $\tau^{-1} = 80\,\text{MHz}$. The pulse length lies between 35 fs and 150 fs. The output power at 800 nm center wavelength was measured at 440 mW (5.5 nJ per pulse), with a spectral bandwidth of 42 nm full width at half maximum (FWHM).

Chirped Amplifier

Inside the Spitfire unit, the nJ laser pulses from the Tsunami are amplified over six orders of magnitude to the mJ scale. The working principle of a chirped amplifier is described in section 2.4.2. In short, a single fs-pulse from the seed laser's pulse train is selected and amplified by passing several times ($\geq 10\times$) through a Ti:Sa crystal that has been excited by the pump laser. To prevent damage to the crystal caused by high light energies, the pulse is stretched in the time-domain before the cavity and recompressed afterwards. Selecting a pulse from Tsunami's input is done by exploiting the light's polarization: Vertically polarized light is trapped inside the cavity, while horizontally polarized light can enter and exit the cavity through a polarization filter. By controlling the laser polarization with Pockels cells (one inside and another one outside the cavity), precisely one pulse can be accepted into the cavity from the 80 MHz train and kept inside for the required number of passes through the crystal, before being ejected. The Spitfire's 1 kHz output has a specified pulse energy of $> 3.5\,\mathrm{mJ}$,[1] and a pulse width of $< 120\,\mathrm{fs}$. [87]

Wavelength Tuning

The femtosecond pulses of the Spitfire system have a fundamental wavelength of 800 nm. However, certain applications (e. g. as a pump beam in TAS) require different wavelengths. To this end, optical nonlinear effects can be utilized to change the pulse's wavelength.

Sum-frequency generation (SFG) is a process that can occur in a medium with a quadratic nonlinearity, i. e. with a non-vanishing second-order susceptibility $\chi^{(2)}$. This requirement can be fulfilled in materials that have no inversion symmetry [81]. In SFG, two light waves with frequencies f_1 and f_2 generate a signal at the frequency $f_3 = f_1 + f_2$. If $f_1 = f_2 = f$, the resulting frequency is $2f$, the second harmonic of f. Second harmonic generation (SHG) of laser light is easily realized by placing a suitable material such as a beta barium borate (BBO) or LBO crystal in the beam path. This allows to convert the Spitfire output wavelength from 800 nm to 400 nm. However, the conversion is not complete and the resulting beam contains a mix of the fundamental and the second harmonic wavelength. To obtain a clean SHG beam, the residual fundamental needs to be removed, e. g. with a hot mirror or shortpass filter.

To have even more control over the wavelength, a two-stage optical parametric amplifier (OPA) is available (Light Instruments TOPAS). In this device, a small fraction of the Spitfire's output is used for WLG in a sapphire crystal. The white light is overlapped non-collinearly with another fraction of the Spitfire output in a non-linear crystal, where parametric amplification occurs. Briefly, this splits the incoming photons with frequency f into two (called signal and idler), according to the energy conservation relation $f = f_{\text{signal}} + f_{\text{idler}}$. The actual value of f_{signal} can be tuned by adjusting the timings between the two light pulses in the crystal. Next, the signal is amplified by overlapping it collinearly with the bulk of the input light in a second nonlinear crystal. Finally, a mixing stage can be used to increase the output frequency by SFG or SHG, which extends the range of accessible wavelengths. The tuning range of the TOPAS is 290 nm to 2600 nm. The pulse energy output varies with the selected wavelength.

3.1.2 Picosecond Pulsed Laser

As a source for pico- to nanosecond pulses, a compact laser system from InnoLas Laser GmbH is used, the Innolas picolo-1 MOPA. The acronym MOPA stands for *master oscillator power amplifier*. As such, the device consists two stages. The first is a Q-switched neodymium-doped yttrium vanadate (Nd:YVO) oscillator which provides short light pulses ($< 0.8\,\mathrm{ns}$) at a fundamental wavelength of 1064 nm. The repetition rate can be tuned up to 5 kHz. The second stage is an amplifier that increases the pulse energy up to 152 µJ. An integrated harmonic generator module can be used to convert the fundamental wavelength to its second (532 nm) or third harmonic (355 nm). This is done using a temperature-controlled LBO non-linear crystal. At 532 nm, the maximum pulse energy is 65.8 µJ.

The laser can be triggered electronically, which makes it ideally suited for application in the long-delay TAS setup described in section 3.5.

---

[1] Measured values for our setup were in the range of 2.7 mJ to 3.6 mJ.

3.1.3 CW Laser Diodes

Besides the pulsed lasers, several CW laser sources are used throughout this thesis as well. Relevant device specifications are given below.

(Q)CW Laser Diode 525 nm

As a source of CW light, a laser diode from Roithner LaserTechnik (LD-515-10MG) is used. This gallium nitride (GaN) based diode has a typical center wavelength of 515 nm with a typical range of 510 nm to 530 nm and a spectral width of 2 nm [88]. The actual center wavelength of our diode was measured as 525 nm. The typical optical output power is 10 mW.

The laser diode is operated in a temperature-controlled mount (Thorlabs TCLDM9) by a laser diode and temperature controller (Thorlabs ITC4001). With this controller, the diode can be run in CW mode or in pulsed quasi continuous wave (QCW) mode. The latter periodically turns the CW output on and off, with a pulse width in the range of 100 µs to 1 s and a repetition rate between 0.2 Hz and 1 kHz [89].

CW Laser Diode 405 nm for PL experiments

For the extended illumination experiments in chapter 5, a GaN based laser diode with a typical center wavelength of 405 nm from Roithner LaserTechnik (DL-7146-101S) is used [90]. The maximum optical output power is 85 mW.

CW Laser Diode 405 nm for microscopy experiments

As an excitation source for luminescence microscopy experiments (see section 3.7 and section 6.1), a diode laser module from Vortran Laser Technology (Stradus 405-250) with a center wavelength of (405 ± 5) nm and an output power of 250 mW is used [91].

3.2 Lifetime Determination via Multi-Channel Scaling

For the experimental determination of PL lifetimes, a setup consisting of a double monochromator, a photomultiplier tube (PMT) and a multi-channel scaling (MCS) card is used, as shown in Figure 3.1. Briefly, laser light (different sources can be used) is used to excite a sample, which can be kept at ambient conditions or in a specially designed vacuum sample holder. The emitted PL from the sample is collected by a set of two lenses and focussed on the slit of a double monochromator. This device acts as a narrow bandpass filter and allows to select a single wavelength from the input light to be passed to the output at which a sensitive detector, the PMT, is placed. The PMT's electric output signal is passed to a MCS card inside a computer for processing. In the following, each of the relevant steps are discussed in detail.

The intensity of the excitation light at the sample position can be controlled by a tunable neutral-density filter in the beam path and monitored by a power meter placed after a beam splitter, so only a small amount of light is sent to the power meter. The light intensity at the sample position and at the power meter scale linearly, the scaling factor can be obtained by performing a power measurement at both positions. Thus, the power at the sample position can be determined without blocking the excitation beam path.

The monochromator (Bentham DTMS300) is used as a variable bandpass filter to select a single wavelength from the incoming light. In the common Czerny-Turner design [92], broadband light is focused on the monochromator's input slit. Inside the device, the slit is on the focal point of a curved mirror, which thus collimates the light and directs it onto a planar diffraction grating. The reflected light is then focused by another curved mirror on the monochromator's output port. However, due to the diffraction grating, each wavelength arrives at a different position and not all of them exit the device. By rotating the diffraction grating, the center

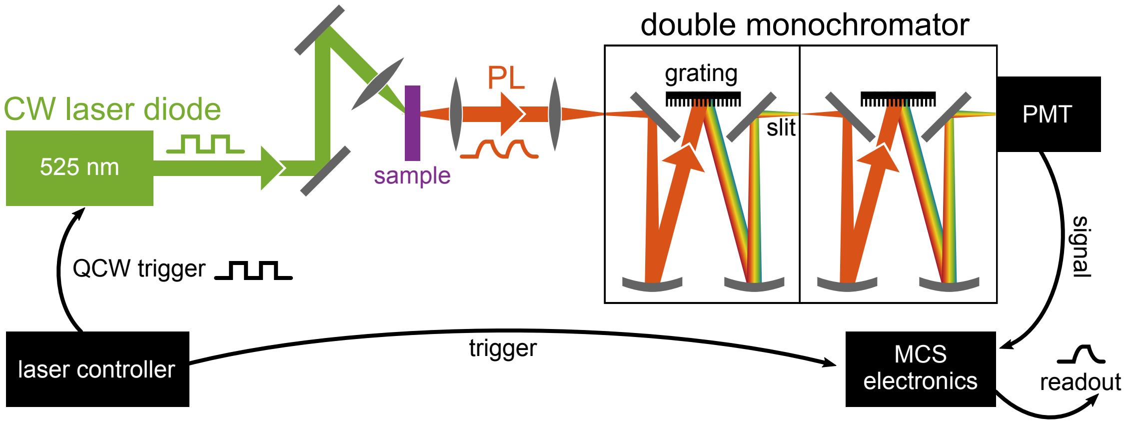

Figure 3.1: Scheme of the MCS setup to measure PL lifetime. A CW laser is used in QCW mode to drive a sample's PL periodically into steady-state. The emission is collected into a double monochromator, where a single wavelength is selected to be sent onto a PMT. The detector's signal is processed by a MCS electronics board to obtain a temporal emission profile (see also Figure 3.3).

wavelength that is able to pass (as well as its diffraction order) can be selected, and by changing the size of the exit slit, the spectral bandwidth of the output light can be tuned.

To improve the rejection of stray light, our setup uses a double monochromator. This design essentially consists of two monochromators connected in series and set to the same wavelength.

After the double monochromator, the filtered, monochromatic light is detected by a PMT. This type of photodetector has a high sensitivity. Even single photons can be detected, which makes it especially interesting for PL measurements of samples with a low emission intensity.

The basic working principle of a PMT is shown in Figure 3.2. Light enters the evacuated device through a window and excites electrons in a photocathode, which are then emitted to the vacuum. Using an electric field, the photoelectrons are accelerated onto a series of electrodes, usually referred to as "dynodes". At each electrode, the electron impact leads to the creation of secondary electrons, which are then accelerated onto the next electrode and so on. The number of secondary electrons per primary electron, δ, usually ranges from 10 to 100, depending on the electrode material and the applied voltage [93]. In an n-stage dynode, the current amplification (gain) is thus δ^n. After the last electrode, the electrons reach an anode, where they are collected and output as an electron current to an external circuit.

The PMT in our setup (Hamamatsu R928P) uses a circular-cage layout for the 9-stage dynode, as shown in Figure 3.2. It has the benefit of being very compact and having a fast time response [93, 94]. The typical gain factor at a supply voltage of 1 kV is 10^7. A multialkali photocathode (consisting of a mixture of different alkali metals) is used to enhance the width of the spectral response (185 nm to 900 nm) [94]. The electrical output signal is amplified by a PicoQuant PAM-102P pre-amplifier module.

Finally, the electrical signal arrives at the MCS board (PicoQuant TimeHarp NANO), which is synchronized to the laser controller. After each laser pulse, the incoming electrical pulses from the detector, which correspond to single photons, are counted and binned according to their time of arrival. This data is then read out by a computer and, over many excitation pulses, a histogram of the time distribution of photon counts is generated. The process is schematically shown in Figure 3.3.

The benefit of MCS over "classical" time-correlated single photon counting (TCSPC) is the fact that multiple events (photons) can be counted per excitation pulse. This greatly decreases the required acquisition time, especially for samples with an emission lifetime on the scale of microseconds and above. One has to keep in mind that the time-to-digital converter has an intrinsic dead time after each photon counting event, during which no further events can be detected. The TimeHarp NANO has a dead time of < 2 ns [95]. This sets an

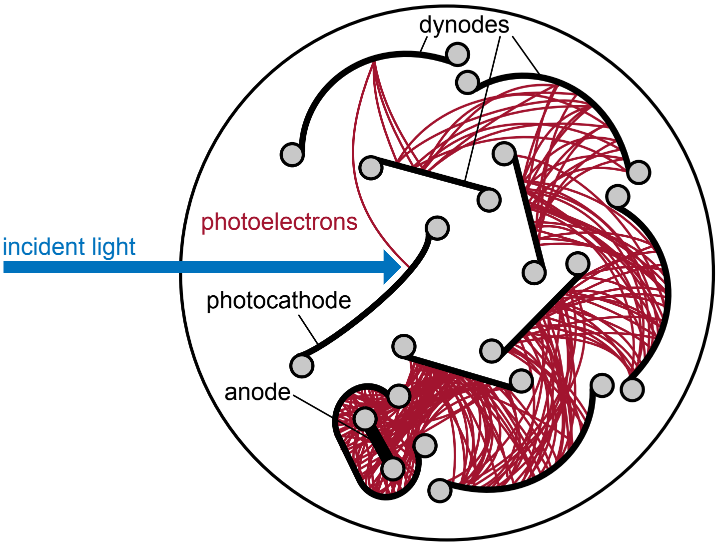

Figure 3.2: Schematic drawing of a circular cage PMT with a 9-stage dynode, similar to the Hamamatsu R928P. Based on *Photomultiplier Tubes – Basics and Applications* [93].

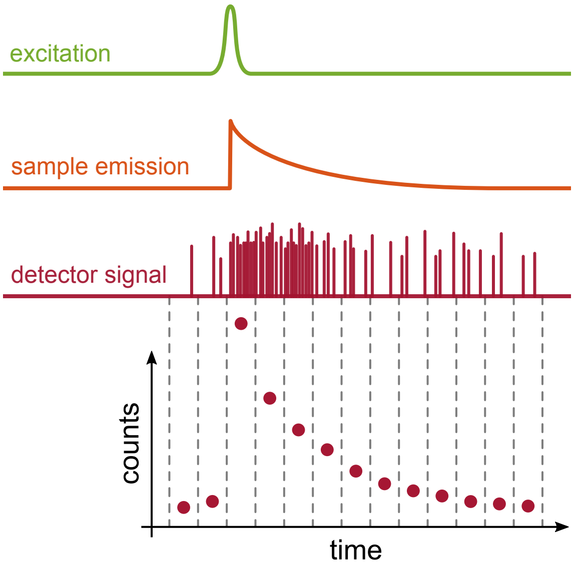

Figure 3.3: Schematic of a MCS measurement. A short light pulse excites the sample, which then emits light. At the detector (e. g. a PMT) photons generate electric pulses which are then counted and assigned to timing bins by the MCS electronics, resulting in the reconstruction of the emission decay profile.

upper limit on the photon rate. If it is surpassed, the resulting decay curve is distorted, as not all photons are counted. Therefore, the PL intensity has to be adjusted accordingly, e. g. by changing the intensity of the excitation light.

3.3 Streak Camera Setup

Time-resolved PL measurements are performed using a streak camera setup, as depicted schematically in Figure 3.4A. The Q-switched laser described above (see section 3.1.2) is used to excite a sample in a vacuum holder (pumped dynamically to $< 10^{-4}$ Pa). The PL is collected by a 2 inch lens and focused onto the input slit of a grating-based spectrometer (Acton SpectraPro SP2300). The dispersed light is then coupled into the actual streak unit (Hamamatsu Universal Streak Camera C10910).

Figure 3.4B illustrates the working principle of the streak unit [96]. Incoming light is focused onto a photocathode, which leads to the emission of photoelectrons. These are accelerated in an electric field and deflected vertically by a second field. The latter field is synchronized to the laser's electronic trigger signal and performs a fast sweep in field strength. Electrons that arrive at different times during the sweep cycle are deflected by a different angle. Subsequently, they are multiplied by a micro-channel plate (MCP). A MCP consists of an array of thin glass capillaries (10 µm to 20 µm in diameter, 0.5 mm to 1 mm long) coated with an electron-emitting material. Secondary electrons are created by repeated impact on the walls of a primary electron traveling through a capillary. This process can lead to the multiplication of a single electron to as many as 10^4 electrons. On a phosphorescent screen, impacting electrons lead to the emission of light, which is then imaged on a CMOS area camera (OrcaFlash 4.0 V2).

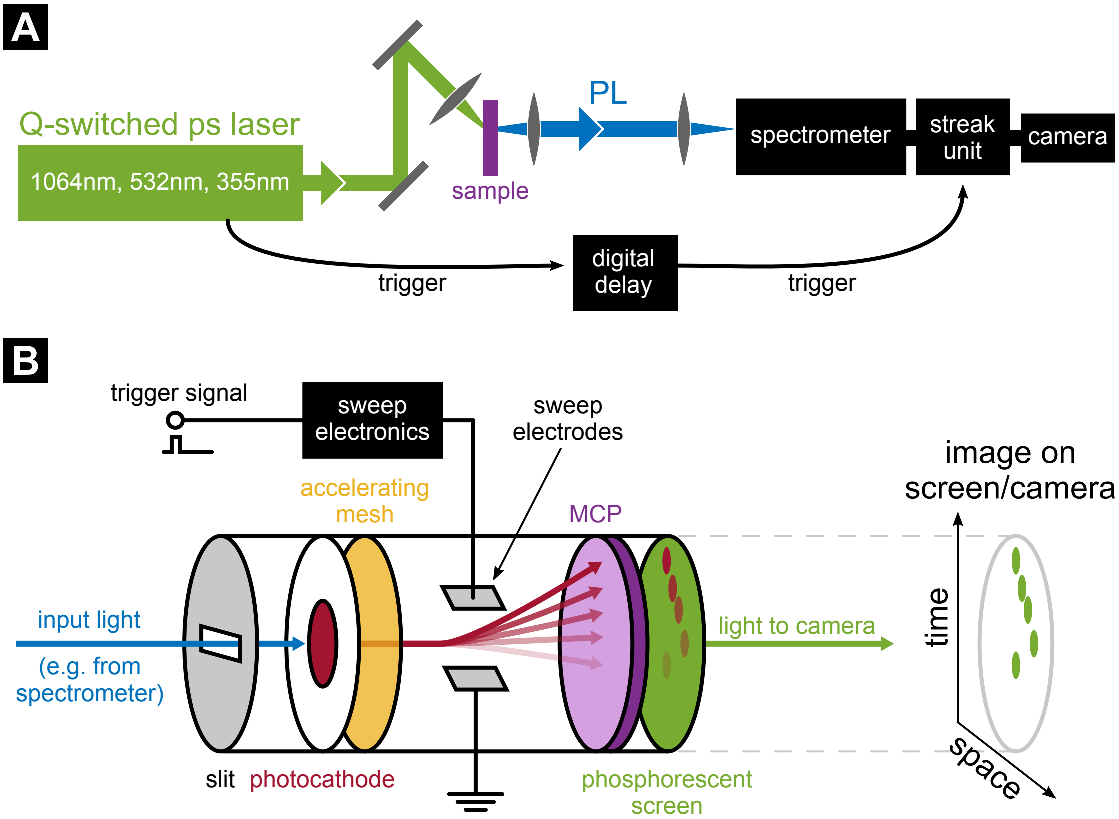

Figure 3.4: Streak camera setup. **(A)** Schematic overview of the setup. A Q-switched laser is used to excite a sample. The emitted PL is collected and focused into a spectrometer, which is coupled to a streak unit and finally a camera module. The streak unit is synchronized to the laser through a digital delay generator. **(B)** Working principle of the streak unit. See text for detailed description. Based on *Guide to Streak Cameras* [96].

As the light is split into its spectral components horizontally by the spectrometer, one axis of the resulting image corresponds to the wavelength of the light. Due to the vertical orientation of the electric sweep field, the vertical image dimension contains information about the light's arrival time. Thus, the streak camera allows to track the evolution of the PL spectrum over time. By changing the sweep speed, different time ranges can be accessed. The sweep unit's trigger signal can be delayed using a digital delay generator (Stanford Research Systems DG645).

3.4 UV/Vis Absorption

Absorption spectra are measured using a PerkinElmer LAMBDA 950 UV/Vis/NIR spectrophotometer [97]. In this device, a deuterium lamp (for the ultraviolet range) or a tungsten-halogen lamp can be used as light sources. The illumination wavelength is scanned by a grating-based monochromator. The light is split into a reference beam and a sample beam by a rotating reflective chopper wheel. The sample is placed inside an integrating sphere coated with Spectralon (a broadband reflective material produced by Labsphere, Inc.). A PMT is used as a detector for wavelengths in the range from 200 nm to 860 nm. For measurements further in the infrared region (860 nm to 2500 nm), an InGaAs detector is available. In this work, only the combination of the tungsten lamp with the PMT is used.

The sample beam directly hits the sample inside the integrating sphere, whereas the reference beam is directed at the sphere's wall and its light reaches the sample only indirectly, as illustrated in Figure 3.5. The transmittance T can be calculated from the detected light intensity with ($I_{\text{sample},1}$) and without ($I_{\text{sample},0}$) sample:

$$T = \frac{I_{\text{sample},1}}{I_{\text{sample},0}}\,. \tag{3.1}$$

The reference beam is used to compensate fluctuations in the light intensity:

$$T = \frac{I_{\text{sample},1} I_{\text{reference},0}}{I_{\text{sample},0} I_{\text{reference},1}}\,. \tag{3.2}$$

Additionally, the reference beam measurement includes absorption of scattered light by the sample. Thus, only absorption by the direct hit of the sample beam is included in the resulting value of T when calculated by Equation 3.2. The sample's absorbance A can be derived from T by

$$A = -\log_{10} T\,. \tag{3.3}$$

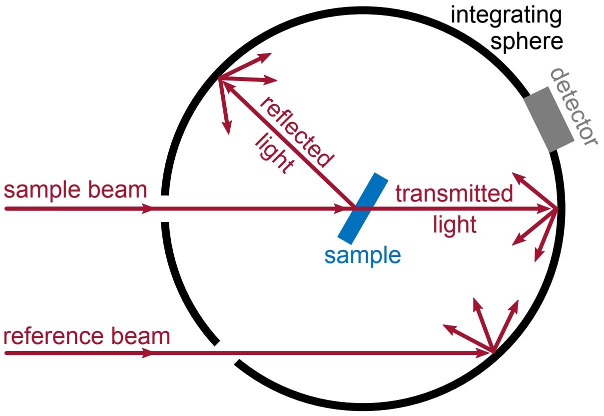

Figure 3.5: Schematic overview of an transmission/absorbance measurement inside an integrating sphere.

3.5 Transient Absorption Spectroscopy

As part of my work, I developed and built a TAS setup, with the goal of investigating triplet exciton dynamics in PdP SURMOFs. Additionally, the setup was conceived as being a versatile tool, aiding other researchers in their investigations. As a result, the setup has been used in six peer-reviewed publications so far [1–4, 98, 99], with another paper[2] currently being under review.

The system was planned with experimental flexibility in mind. It allows for measurements over a wide range of time ranges (pico- to milliseconds), for reflective or transmissive samples in air, solution or under dynamic vacuum and with a range of different pump wavelengths to choose from. Furthermore, the whole experimental process from the actual data-taking until the analysis of the TAS data matrices was taken into account and graphical user interfaces (GUIs) were created to enable a frictionless workflow.

3.5.1 Hardware

This section describes how the TAS system is set up on the optical table and presents the different modes of operation. A schematic overview of the generation of pump and probe pulses can be found in Figure 3.6.

Probe light

The setup uses a femtosecond amplifier (SpectraPhysics Spitfire Pro XP, see section 3.1.1), that outputs a train of 800 nm laser pulses with a pulse width of < 120 fs at a repetition rate of 1 kHz. A fraction of the output is focused into a sapphire crystal, where it is transformed into a broadband white light pulse. This nonlinear process is very sensitive to the position and orientation of the 3 mm thick sapphire crystal. Therefore, it is mounted on a linear translation stage (Thorlabs PT1) that can be moved with micrometer precision along the light propagation direction. Additionally, the crystal can be rotated to ensure the front surface is perpendicular to the light path. A hot mirror is used after the WLG stage to reduce the intensity of residual 800 nm light in the white light spectrum, which is necessary to prevent detector saturation in this spectral region. The 1 kHz femtosecond white light pulse is used as the probe beam.

Pump Light and Delay

Regarding the pump light, two modes of operations are possible for the TAS system: *short delay* and *long delay*. In the former, a fraction of the Spitfire's femtosecond output is used for generating the pump pulse. The tunable pump-probe delay is realized using a retro-reflector on a mechanical delay stage (Thorlabs ODL600/M). The stage has a minimum step size of 0.1 µm, which translates to a minimum delay step of 0.67 fs (for a single pass back and forth on the stage). The range of motion is 600 mm, which means that the maximum delay time is 4 ns. Even considering two or three passes over the stage, which makes the system more difficult to align, this value can be increased only to 8 ns or 12 ns.

To increase the delay time by orders of magnitude, a different approach is necessary. Hence, in the long delay mode, the pump source is no longer the same femtosecond laser as used for WLG. Instead, a Q-switched pump laser (Innolas picolo-1 MOPA, see section 3.1.2) is used that is synchronized to the femtosecond amplifier. A digital delay generator (Stanford Research Systems Digital Delay/Pulse Generator DG535) is used to adjust the relative timing between of the two light sources.

Pump Light Wavelength Tuning

In short delay, the femtosecond laser pulses at 800 nm can directly be used as a pump source. When another wavelength is required to excite the sample, this can be done by using an OPA (Light Instruments TOPAS),

---

[2] Delgado, D. R. *et al.*, Solution-Processed and Evaporated C_{60} Interlayers in Perovskite Photovoltaics.

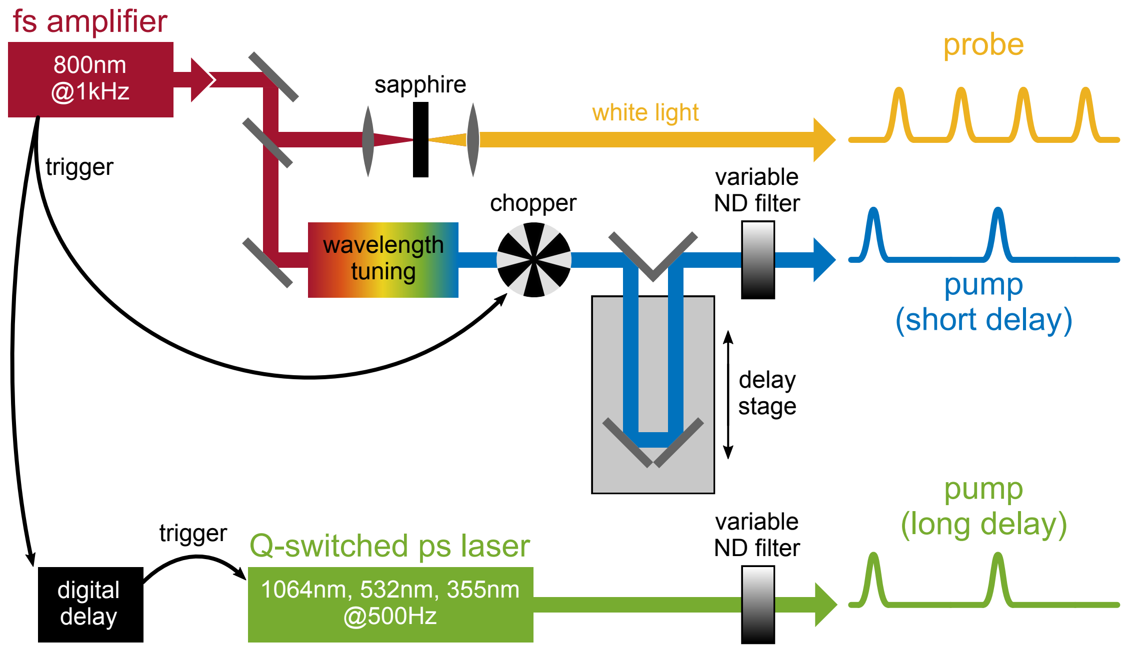

Figure 3.6: Schematic overview of the generation of pump and probe pulses in the TAS setup. The probe light is generated by WLG in a sapphire crystal. Short delay pump pulses are generated from a fraction of the femtosecond amplifier's output. Wavelength tuning can be performed by an OPA or a BBO crystal. A rotating chopper wheel (synchronized to the amplifier) blocks every second pulse. A motorized delay stage is used to vary the pump-probe delay time. A variable ND filter can be used to control the pump fluence. The long delay pump light comes from a Q-switched laser that is triggered from the amplifier through a digital delay generator.

which enables access to wavelengths from 290 nm to 2600 nm (see section 3.1.1 for details). Alternatively, a BBO crystal can be placed in the beam path to convert the wavelength to 400 nm via SHG.

When the OPA is used, it introduces around 2 m of additional path length into the pump beam path. This corresponds to 6.7 ns of added delay between pump and probe pulses. Hence, the temporal overlap between the pulses (zero time) at the sample position is shifted outside the 4 ns wide time window that is accessible by the delay stage in short delay mode. Thus, if the OPA is used, the probe beam path needs to be extended by 2 m.

In long delay mode, the available pump wavelengths are determined by the Q-switched pump laser, which can be operated at 1064 nm, 532 nm or 355 nm.

Pump Light Repetition Rate

As the repetition rate of the probe beam is 1 kHz, the rate for the pump beam has to be 500 Hz. In the short delay setup, the repetition rate is reduced by a mechanical chopper wheel (Thorlabs MC2000). Its rotation speed is synchronized to the Spitfire amplifier in such a way, that every second pulse is blocked by the chopper blades. In long delay mode, a special feature of the digital delay generator is used to trigger only on every second signal from the Spitfire's electronic trigger output.

Sample Conditions

Pump and probe beam are focused and brought into overlap on the sample. Importantly, the pump spot has to be larger than the probe spot on the sample, in order to provide a constant excited state density over the probed region. The sample can be a solution in a cuvette or a solid. Often, experiments under oxygen-containing atmosphere are undesired. For solutions, custom-made cuvettes are available that can be filled and sealed under nitrogen atmosphere in a glovebox. Solid samples can be placed in a custom-built sample holder that is connected to a vacuum pump (Pfeiffer Vacuum HiCube 80 Eco) which allows to keep the sample at low atmospheric pressure (typically below 10^{-4} Pa). In all cases, the samples are at room temperature. The sample holder has two windows that allow transmission of the probe beam.

Detection

After the sample, the pump light is blocked and the probe light passes a slit into a custom-built spectrometer (see Figure 3.7A). The light is dispersed by a equilateral flint glass prism (Thorlabs F2) and the spectrum is detected on a 512 px linear image sensor (Hamamatsu S3904-512Q). The sensor data is read out by a preamplifier (tec5 DZA-S3901-4 1M), digitized (tec5 FEE-1M, bit depth: 16 bit) and sent to a computer (interfaced via a PCI Express card tec5 PD-PCIe01V1). The electronics allow for integration times down to 0.6 ms. Thus, the system allows to detect each probe pulse's spectrum individually. This shot-to-shot method is beneficial compared to averaging over multiple pluses (see section 2.4.1). The readout electronics are synchronized to the 500 Hz rate of the probe pulses, so that the order of "pump on" and "pump off" spectra is ensured to be always the same. Otherwise, potential missing of one trigger pulse would lead to an undesired flip in sign of the TAS signal.

Detecting the transmission behind the sample is the typical way a TAS experiment is performed. However, some samples (for example thin films on silicon substrates) cannot be measured this way. For these cases, the setup can also be used in a reflection mode, as illustrated in Figure 3.7B. Probe light is transmitted through the sample and reflected at the substrate. It is then focused into an optical fiber, to which a compact off-the-shelf spectrometer (Zeiss MMS1) is connected. The grating-based spectrometer has only a 256 px wide sensor (Hamamatsu S8381-256Q). It uses the same readout electronics as the custom spectrometer (namely, the A/D converter tec5 FEE-1M and the PCI card tec5 PD-PCIe01V1) and can accordingly achieve the same shot-to-shot readout rate.

Whereas the fiber-coupled Zeiss spectrometer is factory-calibrated, the custom spectrometer requires manual wavelength-calibration. This process is semi-automated using a motorized filter wheel (Thorlabs FW102C) which is placed directly in front of the spectrometer's input opening. It houses five narrow band-pass filters at different wavelengths, covering the available white light spectrum (typically the center wavelengths of these filters are 480 nm, 532 nm, 633 nm, 730 nm and 850 nm). The filters are consecutively rotated into the probe beam path. An automated fit of a Gaussian distribution to the resulting spectrum at the detector allows to

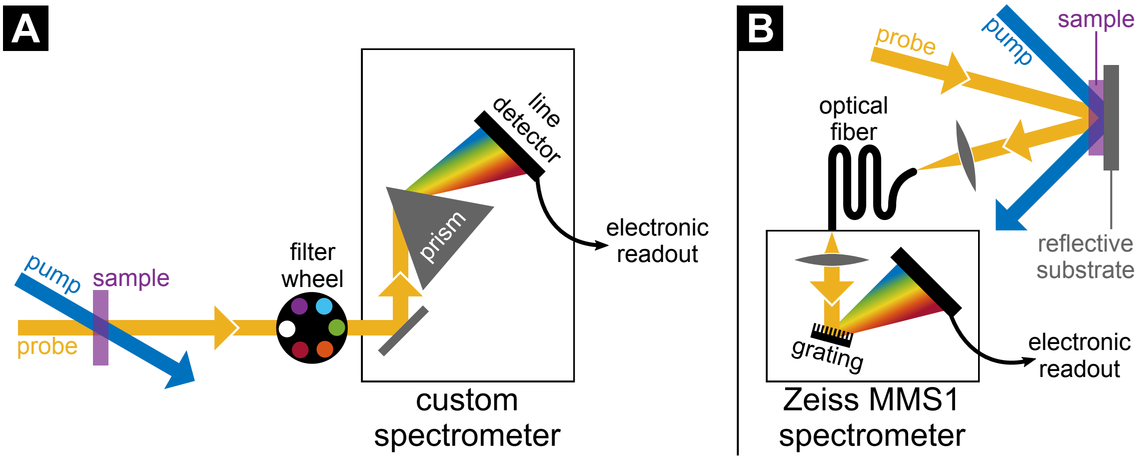

Figure 3.7: Schematic overview of the detectors in the TAS setup for transmission and reflection measurements. **(A)** In transmission mode, a custom spectrometer is used. After the probe beam has passed through the sample, it enters the spectrometer box, where the white light is dispersed by a prism and detected on a line detector. The filter wheel is used for wavelength calibration (see text). **(B)** In reflection mode, the probe beam is transmitted through the sample and reflected on the substrate. The light is then coupled into an optical fiber connected to a grating-based spectrometer.

locate the center pixel which corresponds to the center wavelength of each filter. This way, a look-up table with five pixel-wavelength pairs is built up and used later to translate the sensor data into wavelength units. The sixth position of the filter wheel is used during the measurements. It is either left empty or equipped with a suitable notch filter to prevent stray pump light from entering the spectrometer housing.

3.5.2 Measurement and Control Software

As the TAS system was intended to be used by a wide user base, special care was taken to create user-friendly control software. A single LabVIEW GUI (“TA Control”) needs to be launched on the control computer. From this, all necessary features and tools can be accessed. The workflow of a typical TAS experiment is briefly outlined below.

Before the measurement

In the software’s “Live View” mode, bursts of several pulses are taken repeatedly and the individual spectra are displayed continuously. This allows to check the quality and stability of the probe white light. The “live” spectra are useful feedback for optimizing the white light by adjusting the position and orientation of the sapphire crystal.

Additionally, averaged spectra for T_{on} and T_{off} are displayed as well as ΔT and $\Delta T/T$ spectra. The user can quickly assess whether a TAS signal is present and optimize the spatial overlap between pump and probe beams, as better overlap leads to a stronger signal. By changing the delay, the effect on the TAS spectrum can be directly observed. Thus, zero time (timing overlap between pump and probe pulses) can be determined exactly. Additionally, the lifetime of the TAS signal can be roughly estimated, which is useful information for deciding on the delay time range that is required for the experiment.

The delay times that are to be sampled during the experiment can be defined by the user in a GUI. Typically, the spacing between the delay time points is not uniform but logarithmically stretched, with short intervals at early times (around zero time) and longer intervals later on.

To measure the dependence of the TAS signal on the excitation fluence, a motorized neutral density (ND) filter wheel can be placed in the pump beam path. It can be controlled directly from the TAS control software. A list of filter positions can be defined in a GUI.

A constant background signal on the detector (for example room light) affects T_{on} and T_{off} equally and cancels out in ΔT. In contrast, background signals such as PL from the sample or scattered pump light only affect T_{on} and lead to a constant delay-independent offset in the TAS spectra. To compensate this, two background spectra B_{on} and B_{off} are measured (averaged over many pulses, typically on the order of 10^4) with the white light blocked. During the measurement, they are subtracted from the detector signal.

Finally, the automated wavelength calibration as described above is performed. Now all requirements for the measurement are met and the experiment can be started.

During the measurement

During the measurement, no user interaction is required. For all delay timings a certain (user-defined) number of pump on/off spectra pairs is taken and an average $\Delta T/T$ calculated. After all delay positions have been accessed, the data are saved as a 2D matrix ($\Delta T/T$ over delay time) in a binary file format and (for compatibility reasons) as MATLAB file (.mat). Then, the ND filter wheel rotates automatically to access the next pump fluence and a new run over all delay timings is initiated. After the TAS data for the last fluence have been measured, the experiment starts again from the first fluence value. This cycle repeats until stopped by the user. Finally, the individual 2D data matrices with identical pump fluence are averaged to increase signal-to-noise ratio and saved. The following pseudo-code summarizes these steps:

```
LOOP1: Repeat until stopped
  LOOP2: Excitation fluences (ND filter)
    LOOP3: Delay timings (delay stage/generator)
      Take several spectra pairs
      Calculate dT/T spectrum at this delay time
    END LOOP3
    Create 2D matrix with dT/T spectra over time
    Save matrix to file
  END LOOP2
END LOOP1
Average individual matrices and save to files
```

It is beneficial to perform short measurements repeatedly instead of taking one long measurement,[3] especially when the setup is left unsupervised. For one, this makes the system more fail-safe because partial data are saved regularly. Thus, unforeseen interruptions of the experiment e. g. by a computer crash or a power failure do not result in complete loss of already recorded data. Drifts in laser power, stability or ambient conditions can disturb the sensitive non-linear WLG process, which can result in unstable, fluctuating probe light (leading to noisier $\Delta T/T$ data) or even the total loss of white light. In such cases, having several consecutive $\Delta T/T$ data sets taken allows to selectively average the "good" ones and ignore all measurements with bad probe light conditions. Lastly, some samples undergo photochemical changes during extended illumination, which can lead to a change in the TAS signal over time. Comparing the individual experiments can unveil these changes. In such cases, averaging over all individual data sets should be avoided, as it distorts the resulting kinetics and spectra.

During the measurement, the user is presented with a GUI that allows them to view the dataset as it is recorded and perform some simple analysis steps (see screenshots in Figure 3.8). For example, the whole 2D data surface can be visualized or kinetic and spectral slices can be plotted. This gives the user valuable information that can be used to asses the quality of the data that are taken and – if necessary – stop the measurement and restart it with different parameters. Data from the individual experiments can be compared (for example to check for degradation) and data from previous measurements can be loaded and compared on-the-fly, without interrupting the measurement process.

After the measurement

The averaged (or individual) 2D TAS matrices are saved in a custom binary file format. For analysis, a MATLAB GUI ("Surface Explorer") is provided to the user that can load these binary files and plot the 2D TAS matrix. A screenshot of the GUI is shown in Figure 3.9. Besides visualization, one of the most common tasks in the analysis of this kind of data is extraction of kinetics and spectra, which is made easy by the GUI and was the original motivation for its creation. The extracted data can be further analyzed directly in MATLAB or copied to other commonly used tools such as Origin or Excel. When working with several data files, recurring tasks (such as extraction of the same set of integrated spectra) can be automated with a simple scripting language.

Moreover, semi-automatic chirp-correction of short delay TAS data can also be performed directly in Surface Explorer. This becomes necessary because the probe white light pulse is chirped, i. e. zero time is slightly shifted for different wavelengths. In order to properly compare kinetics at different spectral positions, the data need to be rectified before analysis. A GUI module of the program assists the user in this. It shifts the data at each wavelength to have a common zero time and saves the it to a new file. A comparison of an affected TAS dataset before and after chirp correction is shown in Figure 3.10.

---

[3] As in TAS very small quantities are measured ($\Delta T/T \lesssim 10^{-3}$), typical measurement times are on the order of hours.

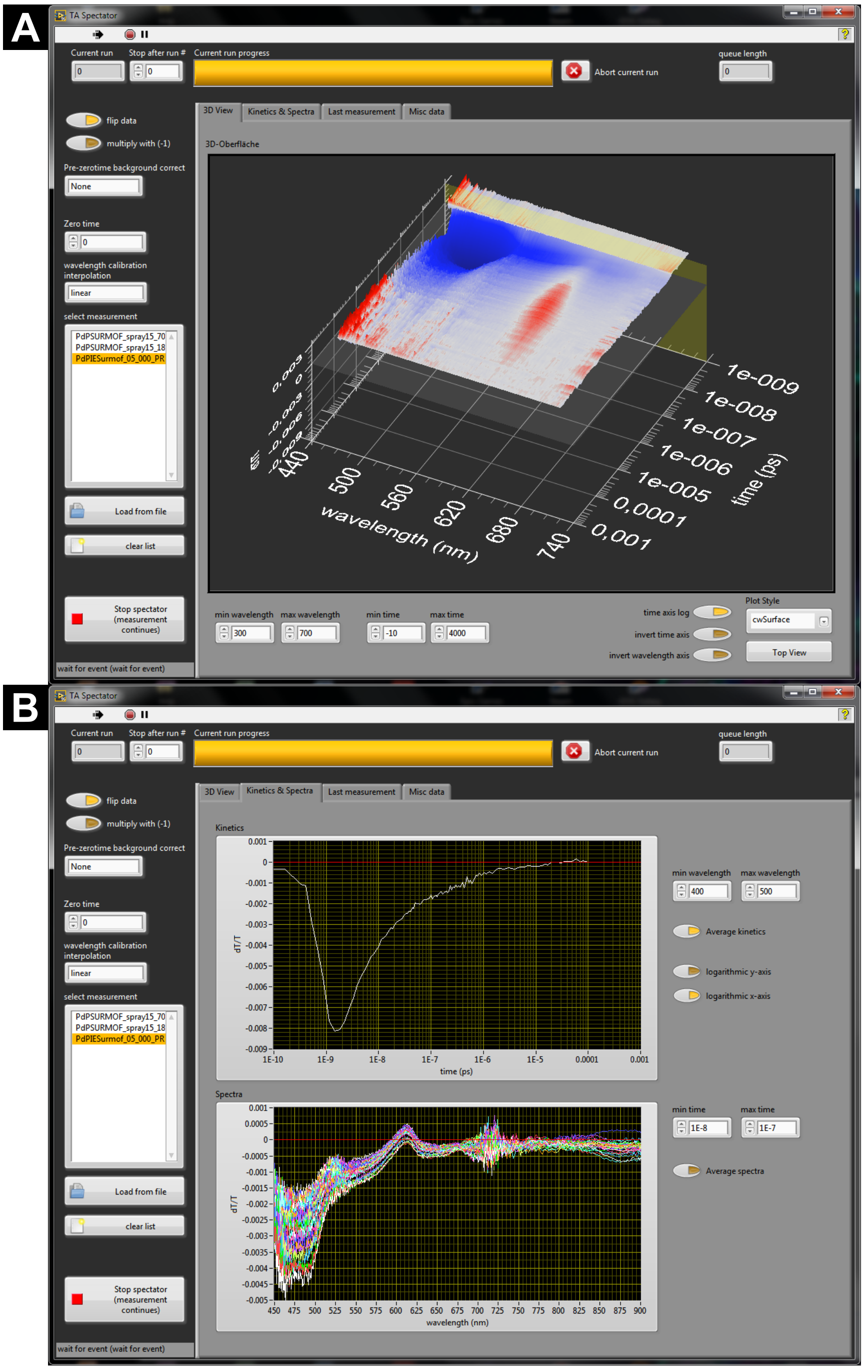

A

TA Spectator

Current run: 0
Stop after run #: 0
queue length: 0
Pre-zerotime background correct: None
Zero time: 0
wavelength calibration interpolation: linear
select measurement: PdPSURMOF_spray15_70, PdPSURMOF_spray15_18, PdPIESurmof_05_000_PR
min wavelength: 300
max wavelength: 700
min time: -10
max time: 4000
Plot Style: cwSurface
wait for event (wait for event)

B

TA Spectator

Current run: 0
Stop after run #: 0
queue length: 0
Pre-zerotime background correct: None
Zero time: 0
wavelength calibration interpolation: linear
select measurement: PdPSURMOF_spray15_70, PdPSURMOF_spray15_18, PdPIESurmof_05_000_PR
Kinetics – min wavelength: 400
Kinetics – max wavelength: 500
Spectra – min time: 1E-8
Spectra – max time: 1E-7
wait for event (wait for event)

Figure 3.8: Screenshots of the TA Control LabVIEW GUI during a measurement. **(A)** The TAS data is interactively visualized as it is taken and can be compared to other data sets. **(B)** Quick analysis and comparison can be performed by plotting (averaged) kinetics and spectra without interrupting the measurement process.

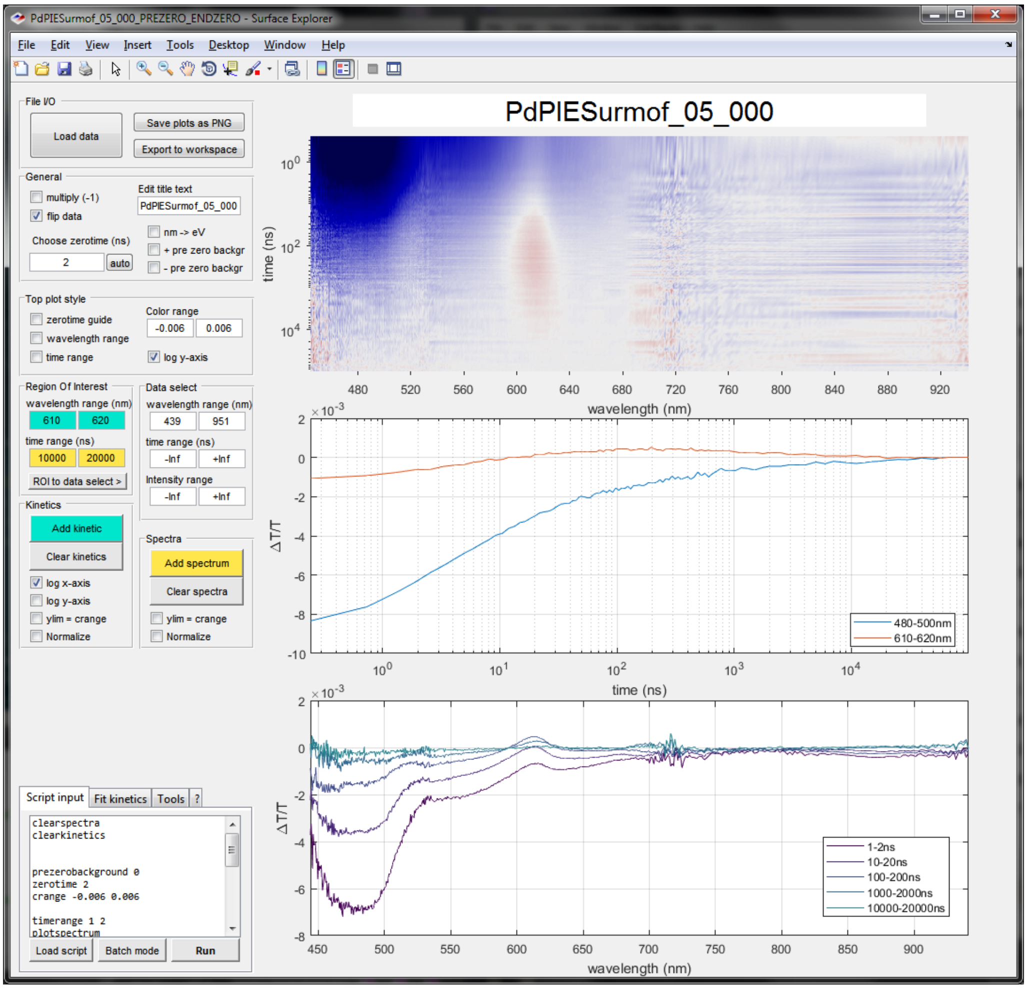

☐ multiply (-1)
☑ flip data
Edit title text: PdPIESurmof_05_000
Choose zerotime (ns): 2 auto
☐ nm -> eV
☐ + pre zero backgr
☐ - pre zero backgr
☐ zerotime guide
☐ wavelength range
☐ time range
Color range: -0.006 0.006
☑ log y-axis
wavelength range (nm): 610 620
time range (ns): 10000 20000
wavelength range (nm): 439 951
time range (ns): -Inf +Inf
Intensity range: -Inf +Inf
☑ log x-axis
☐ log y-axis
☐ ylim = crange
☐ Normalize
☐ ylim = crange
☐ Normalize

```
clearspectra
clearkinetics


prezerobackground 0
zerotime 2
crange -0.006 0.006

timerange 1 2
plotspectrum
```

Figure 3.9: Screenshots of the Surface Explorer MATLAB GUI. The tool can be used to read TAS data, visualize it (top panel), extract kinetics (middle panel) and spectra (bottom panel). All data can be easily transfered to other software for further analysis.

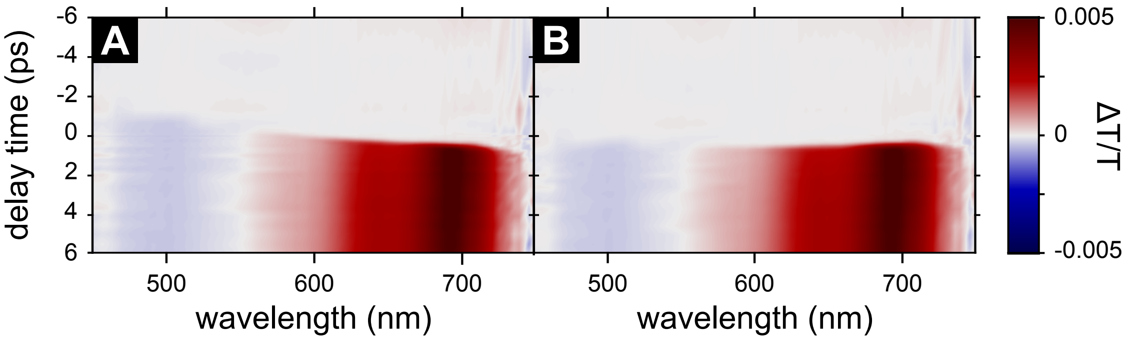

Figure 3.10: Chirp correction of short delay TAS data. **(A)** Raw data shows the chirp of the white light pulse. The shorter wavelengths show signal earlier than the longer wavelengths. The zero time edge appears tilted. **(B)** After chirp-correction with the Surface Explorer MATLAB GUI, the zero time edge is rectified, i. e. the signal at all wavelengths rises at the same time.

Surface Explorer is not restricted to TAS data. All data that can be represented as a 2D data surface can be loaded and processed. Notable examples include time-resolved PL data (streak camera) or time-resolved electron paramagnetic resonance spectrosopy (trEPR) data. Hence, the GUI is a highly versatile and useful tool that integrates seamlessly into the workflow of analyzing time-resolved spectroscopic data.

3.5.3 Current and future development

Several changes have been made by me to the setup recently, in order to increase its utility and versatility. The whole system was moved to a new state-of-the-art femtosecond laser system that can provide higher repetition rates (up to 20 kHz), which reduces the measurement time. Accordingly, a new spectrometer has been developed to obtain shot-to-shot spectra at these higher repetition rates. Furthermore, the updated spectrometer includes an additional NIR line camera to extend the sensitivity of the system into the infrared. Also, WLG inside a calcium fluoride (or YAG) crystal will be implemented, which yields a white light spectrum with a stronger ultraviolet (infrared) component as compared to WLG in sapphire. Finally, the updated setup allow the sample to be placed inside a closed-cycle helium cryostat, which opens up new experimental possibilities.

3.6 Steady-State PL

To measure the PL emission in steady state, the sample is kept under dynamic vacuum ($< 10^{-4}$ Pa) and is excited by the focused output of a 525 nm CW diode laser (see section 3.1.3). The emitted light from the sample is fibercoupled into a spectrometer (Avantes SensLine AvaSpec-ULS-RS-TEC). Scattered excitation light is blocked by a 550 nm longpass filter (Thorlabs FEL0550). Depending on the signal intensity, integration times are varied between 6 s and 90 s, respectively.

The intensity of the excitation light can be tuned by rotating a continuously variable ND filter (with a range from ND0 to ND2). A fraction of the excitation light is diverted before reaching the sample and directed onto a photodiode to measure its power. Using the ratio between this power and the respective value at the sample position (measured earlier), the actual excitation power at the sample are tracked. This corrects for any fluctuations in the laser diode's output as well as inaccuracies in the rotation of the variable ND filter.

To increase the range of excitation power densities, measurements are performed using two different lenses to focus the excitation light onto the sample, resulting in spot areas of 0.01 mm^2 and 0.52 mm^2. As the collection area is the same in both cases (and much larger), the measured spectrometer signal (proportional to the photon flux) needs to be corrected for the smaller emissive area in the better focused sample. This is done by multiplying it with the ratio between the excitation areas (≈ 52).

3.7 Luminescence Microscopy

Steady-state PL microscopy experiments are performed on a widefield inverted microscope (Zeiss Axio ObserverZ1). The output of a 405 nm CW laser (Stradus 405-250, Vortran Laser Technology, see section 3.1.3) is passed through an acousto-optical tunable filter (AOTF) (AOTFnC-400.650, A-A Opto-Electronic), which is used to control the beam's intensity. The light is coupled into a fiber for spatial filtering and the fiber's output is collimated by a convex lens and focused by an oil immersion objective (Zeiss alpha Plan-Apochromat 63×/1.46 Oil Corr M27) into the sample. The phosphorescence signal or the scattered light from the excitation light are collected by the same objective, passed through bandpass filters (Thorlabs FB405-10, 405/10 nm (center/FWHM), for the excitation light; AHF BrightLine HC 698/70 for phosphorescence) and imaged onto an electron multiplying charge-coupled device (EMCCD) camera (Andor Ixon Ultra X-7759). A schematic drawing of the microscopy setup is shown in Figure 3.11. The resolution limit for this setup can be calculated using the Abbe-criterion

$$d = \frac{\lambda}{2\,\mathrm{NA}} = \frac{\lambda}{2 \times 1.46}\,. \tag{3.4}$$

To prevent triplet quenching by atmospheric oxygen, the sample is encapsulated in a glovebox under nitrogen atmosphere.

3.8 Electron Paramagnetic Resonance

In an electron paramagnetic resonance (EPR) experiment, an external magnetic field is used to split the spin energy sublevels (Zeeman effect, see section 2.1.5) in a previously photo-excited (e. g. by a short laser pulse) material. A microwave source can drive transitions between these sublevels. Depending on the applied field strength and the spin polarization, absorption or stimulated emission can be observed and used to identify excited states such as radicals (doublets) or triplet excitons. In contrast, singlet excitons cannot be detected by EPR, because they do not exhibit sublevel transitions.

Time-resolved electron paramagnetic resonance spectrosopy (trEPR) experiments are performed at Helmholtz Zentrum Berlin. The custom-built setup allows for measurement at X band (9.6 GHz, Bruker ER 4118X-MD5 cavity resonator) and Q band (9.6 GHz, custom cavity resonator) microwave frequencies. The resonators are housed inside a helium gas-flow cryostat and placed between the poles of an electromagnet. The samples are excited at a wavelength of 532 nm using the SHG output of a diode-pumped pulsed neodymium-doped yttrium aluminum garnet (Nd:YAG) laser (Atum Laser Titan AC compact 15MM). The pulse energy is 2 mJ at 100 Hz repetition rate with a pulse duration of 5 ns and a spot size of around 1 cm^2.

Time-resolved absorption and emission of microwave radiation by the excited sample inside the cavity is recorded using a digital oscilloscope (LeCroy WaveRunner 104MXi). The recorded time span is 20 µs for X and 10 µs for Q band experiments. Additionally, the magnetic field strength is swept. Thus, microwave absorption and emission data are obtained as a function of both time and magnetic field. To improve signal-to-noise ratio, experiments are repeated several times for each magnetic field strength. Correction for background signal is done by performing a measurement far from the resonant signal and subtracting it from each EPR transient. The magnetic field axis is calibrated using a NMR Gaussmeter (Bruker ER 035M). The (constant) offset between Gaussmeter and the sample position is determined using a reference sample (C_{60} encapsulated in nitrogen).

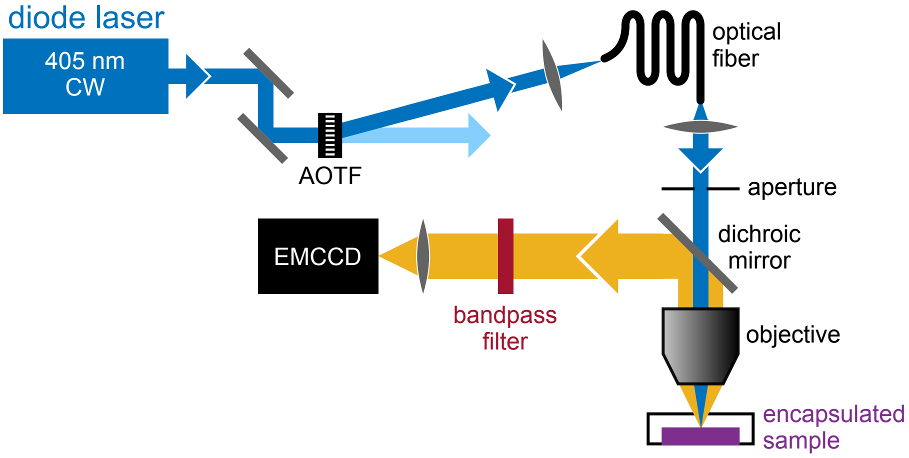

Figure 3.11: Schematic drawing of the PL microscopy setup. See text for detailed description.

3.9 MALDI-ToF Mass Spectrometry

Mass spectrometry is an analytical method to measure the mass-to-charge ratio m/z of a material. Here, m is the atomic mass and z the charge number. This is a common notation in mass spectroscopy.

Typically, a sample is bombarded with electrons or illuminated with an intense laser beam. In either case, the material releases ionized molecules, which are then separated by their m/z ratio. This can be accomplished using electric and/or magnetic fields to separate the ions spatially according to their m/z. Another method is to separate the ions in the time domain by accelerating them in an electric field and measuring the time it takes for them to reach a detector. This is called the *time-of-flight* method.

Electron bombardment can lead to undesired fragmentation of larger molecules. To circumvent this problem, the investigated material can be embedded in a matrix of a second type of molecule. This leads to so called "soft ionization" of analyte molecules. The combination of this method with the time-of-flight scheme is known as matrix-assisted laser desorption/ionisation time-of-flight mass spectrometry (MALDI-ToF-MS).

The setup used for MALDI-ToF-MS experiments is a 4800 Plus MALDI-ToF/ToF mass spectrometer (Applied Biosystems/MDS SCIEX) equipped with a Nd:YAG pulsed laser (wavelength 355 nm, pulse length < 500 ps, repetition rate 200 Hz). The 4000 Series Explorer software (V3.5.3, Build 1017) and the Data Explorer software (V4.9, Build 115) are used for analysis. For each mass spectrum, 500 laser shots are averaged. Before the experiment, samples are digested in a solution of acetic acid (5 %) in ethanol. The matrix substance is DCTB (trans-2-[3-(4-tert-Butylphenyl)-2-methyl-2-propenylidene]malononitrile).

3.10 Preparation of PdP SURMOF Thin Films

The PdP SURMOF films used in this work are based on the established SURMOF-2 isoreticular series [100]. In this specific analogue, zinc paddle-wheel nodes are coordinated to four ditopic palladium porphyrin linkers (15-bis(4-carboxyphenyl)-10,20-diphenylporphyrinato)-palladium(II), in this work abbreviated as PdP). The molecules assemble into free-standing 2D sheets perpendicular to the substrate (see Figure 3.12). The center-to-center distance of PdP molecules inside a sheet is 2.5 nm, whereas the distance between adjacent sheets is 0.6 nm [67].

The PdP SURMOF films used in this work are prepared by the spray-coating method as described exemplarily by Oldenburg [71] and briefly outlined below. The first preparation step is the cleaning of glass substrates in an acetone-ethanol (1:1) solution in an ultrasonic bath for around 5 min. In the next step, the native oxide layer is functionalized with hydroxy groups. This is done either in an oxygen plasma oven or by illumination with ultraviolet light (in both cases for 15 min).

The synthesis of the linker molecule 15-bis(4-carboxyphenyl)-10,20-diphenylporphyrinato)-palladium(II) (in this work abbreviated as PdP) is described in detail by Adams *et al.* [1]. Zinc acetate and ethanol were purchased from VWR and used as received. The linker is dissolved in ethanol in a concentration of $20\,\mu\mathrm{mol\,L^{-1}}$. Zinc acetate is dissolved in ethanol as well ($200\,\mu\mathrm{mol\,L^{-1}}$). First, the zinc acetate solution is sprayed on the substrate (15 s), followed by a waiting time (15 s) and rinsing with ethanol (5 s) to remove unreacted material. Then, the linker solution is sprayed (25 s), which is again followed by a waiting time (35 s) and a rinsing step (5 s). This process is repeated several times to build up the SURMOF. The number of spray cycles determines the film's thickness, as can be seen in Figure 3.12B. The growth rate of this deposition protocol was reported as around 16 nm per cycle [59, 71].

Crystallinity of each sample film is ensured by X-ray diffractometry (XRD): The sample is illuminated by X-ray radiation and the reflected intensity is measured. The incident angle θ of the incoming (and accordingly the detected) beam is varied in a plane, either parallel to the substrate ("out-of-plane" measurement) or

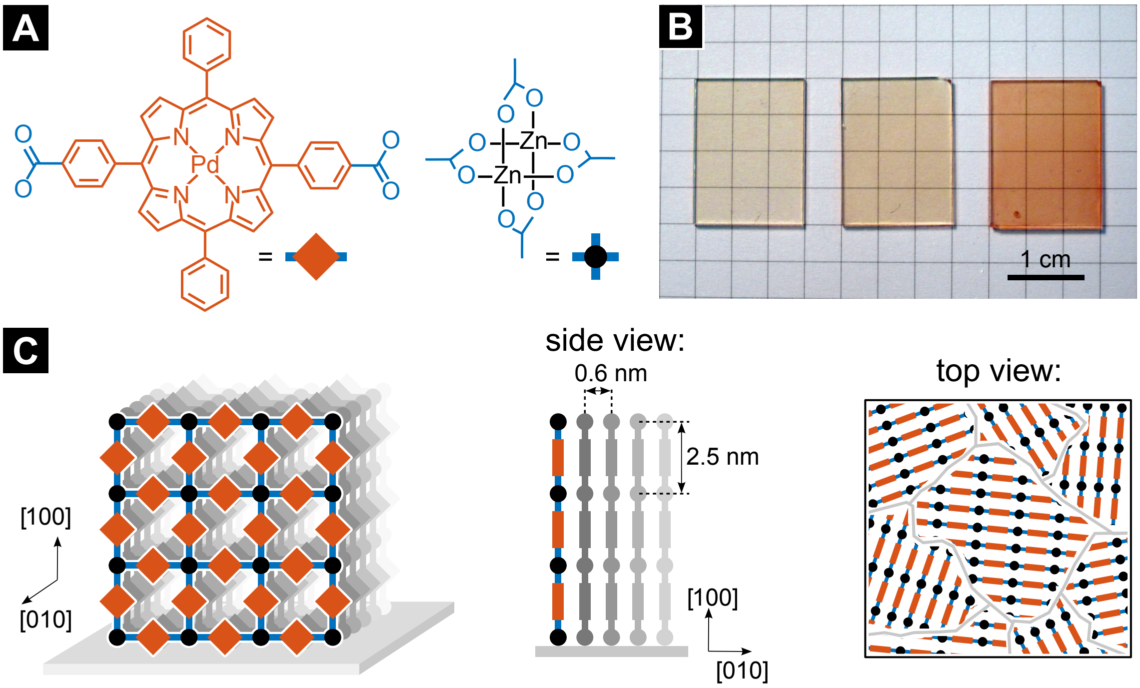

Figure 3.12: The PdP SURMOF. **(A)** Chemical structure of the SURMOFs building blocks: the PdP linker molecule (orange) and zinc acetate metal nodes (black). **(B)** Photograph of three PdP SURMOF thin film samples on glass substrates fabricated with increasing number of spraying cycles (from left to right: 2, 4 and 15 cycles). **(C)** Schematic drawing showing the arrangement of the building blocks into free-standing sheets with the crystallographic axes indicated in square brackets. The top view highlights that crystal domains with different alignments are formed in the substrate plane. Adapted with permission from Adams *et al.* [2].

perpendicular (“in-plane”). X-rays reflected on different crystal planes interfere according to Bragg’s law for constructive interference:

$$n\lambda = 2d\sin(\theta), \tag{3.5}$$

with n being the diffraction order, λ the X-ray wavelength and d the distance between crystal planes. Thus, the diffractogram allows to calculate the dimensions of the crystal’s unit cell. This is how the dimensions shown in Figure 3.12 have been determined.

The measurements were carried out using a Bruker D8-Advance diffractometer equipped with a position sensitive detector (Lynxeye) in θ-θ geometry.[4] The X-ray source is a Cu-anode ($K_{\alpha1,2}$ radiation at $\lambda = 0.154018\,\text{nm}$). Out-of-plane XRD is performed routinely on all PdP SURMOF samples after preparation. The data of such a measurement is exemplarily shown in Figure 3.13. From the peak positions, the crystal plane distance $d = 2.5\,\text{nm}$ can be derived. The inter-sheet distance can be extracted from in-plane XRD, which is experimentally more difficult to perform, especially for thin films with thicknesses on the oder of only 100 nm. The value of 0.6 nm was determined by Liu *et al.* for PdP SURMOF thin films that were prepared in an identical fashion as in this work [67].

An important caveat of this method that should be kept in mind is that, on the one hand, the absence of an XRD signal in a film suggests that the material is not crystalline. On the other hand, the presence of such a signal signifies only that at least part of the sample is crystalline. Notably, it does not imply that the whole film is defect-free or without non-crystalline regions.

---

[4] This means that the sample is fixed and both X-ray tube and detector move by an angle θ. In contrast, in θ-2θ geometry, the X-ray tube is fixed, the sample rotates by an angle θ and the detector by an angle 2θ.

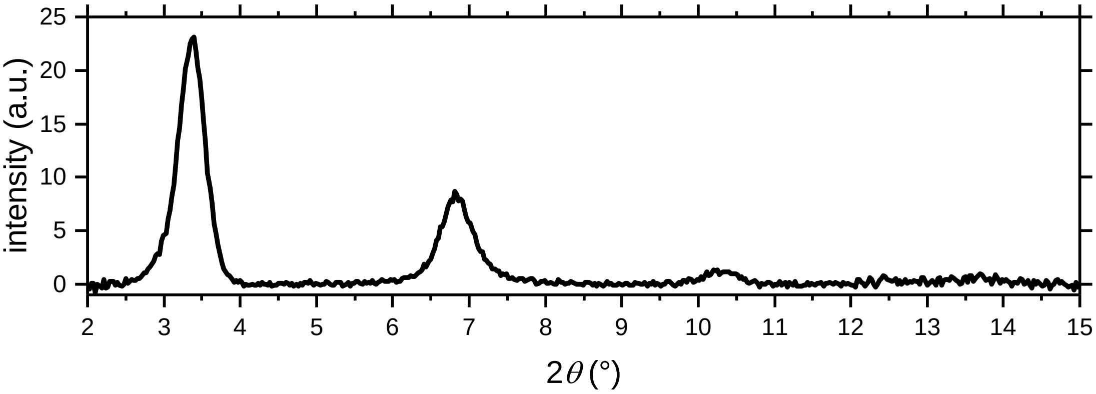

Figure 3.13: Out-of-plane XRD data of a PdP SURMOF thin film sample showing the first three diffraction orders.

4 Exciton Transport in PdP SURMOFs

In this chapter, basic photophysical properties of PdP SURMOF films are established and anisotropic triplet exciton motion inside such films is investigated.

4.1 Creation and Lifetime of Excitons in a PdP SURMOF

The first step in understanding the excitonic processes inside PdP SURMOFs is to look at which types of excitons are created upon illumination and how long their intrinsic lifetimes are. This establishes a basis for further experimentation and analysis.

Acknowledgments and Contributions

The experiments in this section were conceived by the author and Ian A. Howard. The PdP linkers were designed and synthesized by Ganapathi Emandi and Mathias O. Senge. Nicolò Baroni and Michael Oldenburg prepared PdP SURMOF samples with the guidance of Christof Wöll. Absorbance, PL, streak camera and lifetime experiments were performed by the author. Data analysis was performed by the author with support by Ian A. Howard.

4.1.1 Absorption

Excitons are created by the absorption of light in the PdP linker molecules. The absorbance spectra of the linker in solution and inside the SURMOF structure are shown in Figure 4.1. Their difference indicates, that the SURMOF structure alters the molecule's photoresponse. In ethanol solution, the PdP linker exhibits characteristic absorbance peaks at 415 nm (Soret band) and 520 nm (Q band). In the SURMOF, these peaks are red-shifted to 435 nm and 530 nm, respectively. The changes are consistent with those observed in palladium tetraphenyl-porphyrin (PdTPP) based 2D and 3D conjugated microporous polymers (CMPs) [101].

These bathochromic shifts are caused by J-type aggregation and increased π-π interaction of the porphyrin molecules [102]. Furthermore, the Soret band is significantly broadened, which is caused by long-range dipole-dipole interactions [102, 103]. The energy shifts can be understood by quantum chemical calculations, which show that strong noncovalent interactions between the closely packed PdP molecules affect the electron density localization on the PdP frontier orbitals. This changes the energy difference between HOMO and LUMO, which leads to the observed bathochromic shift in the absorbance spectrum [2].

4.1.2 Photoluminescence

Upon absorption of light in the PdP SURMOF film, singlet excitons are created. Metal centers in organic molecules induce spin-orbit coupling [104] and enable efficient ISC. Hence, the ISC yield is close to unity in the case of PdP [43, 44] and the singlet excitons convert quickly to the triplet state. This process leads to a singlet exciton lifetime of less than 15 ps [67].

Ignoring non-radiative processes, the fraction of the singlets that does not cross over to the triplet state can decay radiatively via fluorescence. This emission's center wavelength is 610 nm for the linker molecule in ethanol solution and 620 nm for the PdP SURMOF, as can be seen in Figure 4.1 (the sample is excited at

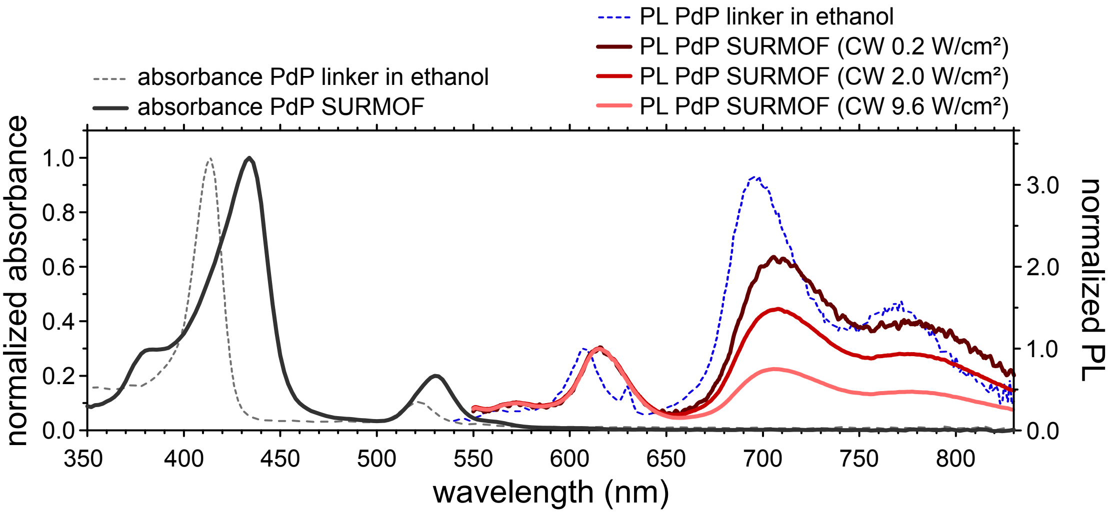

Figure 4.1: Normalized absorbance and PL spectra of the a deaerated solution of PdP linker in ethanol (concentration 10 µmol L^{-1}) and of a PdP SURMOF thin film on glass. The absorbance is normalized to the Soret band maximum, whereas the PL is normalized to the fluorescence around 525 nm. For the PL spectra, the samples were excited with a 123 456 789 nm CW laser and the SURMOF was kept under dynamic vacuum (< 10^{-4} Pa at room temperature). Adapted with permission from Adams *et al.* [2].

525 nm, see section 3.1.3). The triplet excitons decay via phosphorescence, which can be observed as two broad peaks centered roughly around 700 nm and 770 nm in solution or 710 nm and 780 nm in the SURMOF. The difference between the PL spectra in solution and the SURMOF can again be attributed to a shift in the energies of the frontal orbitals caused by the close stacking of the porphyrin molecules.

The assignment of the PL peaks to fluorescence and phosphorescence is consistent with literature [101, 105]. Additionally, streak camera measurements of a PdP SURMOF thin film confirm this as well. The sample is excited by the Q-switched pulsed laser (see section 3.1.2) at 532 nm with 280 µJ cm^{-2} and a repetition rate of 333 Hz. The sample is kept under dynamic vacuum of < 10^{-4} Pa. The measured data are shown in Figure 4.2. The emission at 620 nm (fluorescence) is very short-lived, the decay is faster than the 6 ns instrument response time. The signal above 660 nm (phosphorescence) decays more slowly over several hundred microseconds. The intensity difference between fluorescence and phosphorescence in the streak camera measurement is due to the difference in lifetime and photoluminescence quantum yield (PLQY) of the two processes.

The low intensity and long lifetime of the phosphorescence makes streak camera measurements of the PdP SURMOFs a difficult endeavor, as long integration times are necessary. For example, the data shown in Figure 4.2 was taken over the course of more than 65 h. We will see in chapter 5 that extended exposure to intense light alters the photoresponse of the PdP SURMOF drastically, which prevents us from analyzing pristine samples with the streak camera. This is also connected to the available streak camera setup. The spectral response of the streak tube is optimized for the IR region and not the visible wavelength range of the above measurements. This makes the spectral response more than one to two orders of magnitude lower than with other commercially available streak tubes. Changing this component could aid in shortening experiment time. In this thesis, however, alternative experimental methods will be employed to bypass the shortcomings of the available streak setup. MCS and TAS will be used to monitor the time-dependent behavior of triplet excitons in PdP SURMOFs.

4.1.3 Triplet Exciton Lifetime

In contrast to the short-lived singlet excitons (< 15 ps), the triplet lifetime is on the microsecond scale, which is established experimentally by tracking the phosphorescence decay of a PdP SURMOF thin film after low-

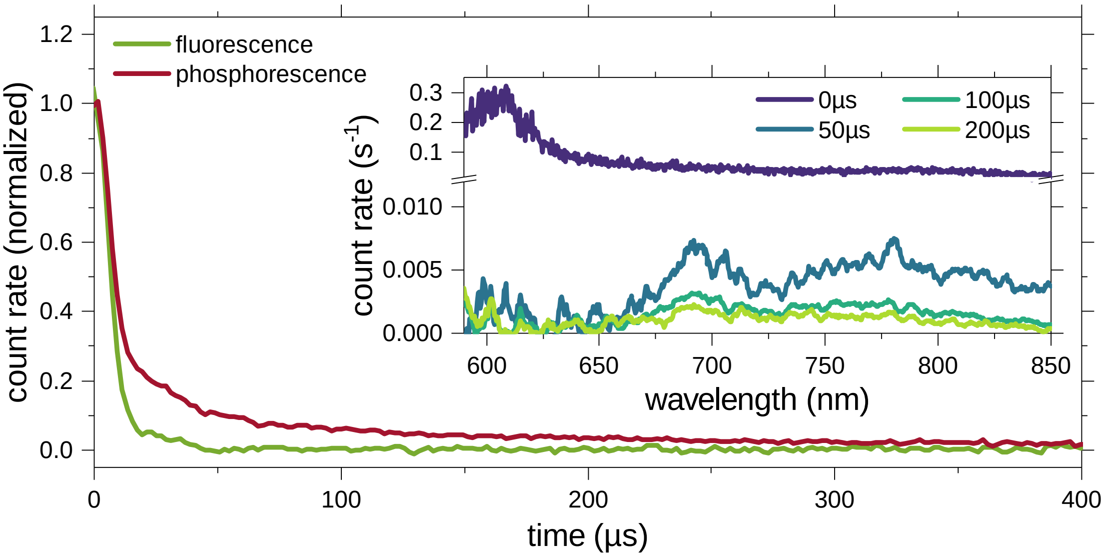

Figure 4.2: PL time evolution of a PdP SURMOF thin film obtained from a streak camera experiment. The sample was excited at 532 nm with 280 µJ cm^{-2}. The fluorescence is integrated from 610 nm to 630 nm, whereas the phosphorescence is integrated from 660 nm to 850 nm. The inset shows the PL spectra at different times after the excitation pulse. The data for 50 µs, 100 µs and 200 µs are smoothed (sliding window average with a window size of 10 pixel) for better visibility.

intensity excitation. The light source is a 525 nm laser diode (see section 3.1.3) in QCW mode (laser on for 1 ms, laser off for 4 ms). The sample is kept under dynamic vacuum ($< 10^{-4}$ Pa) at room temperature. The power density is kept low at 58 mW cm^{-2} in order to reduce the influence of TTA. The phosphorescence decay at 700 nm was measured using a double monochromator, a PMT, and multi-channel scaling electronics synchronized to the laser source (see section 3.2). A 550 nm longpass filter in front of the monochromator is used to block excitation light. Due to the low phosphorescence intensity, the measurement time is 22 min.

The resulting data are shown in Figure 4.3. Before zero-time, the CW laser drives the phosphorescence into steady state. At $t = 0$, the laser is turned off and the signal decays. The initial part of the signal (until around 200 µs) decays slightly faster than the subsequent part. This can be explained by TTA. At lower excited state concentrations, which are reached after around 1 ms, this contribution to the triplet decay vanishes. By fitting a mono-exponential function to the tail of the decay, the monomolecular triplet lifetime $\tau = (729 \pm 2)\,\mu\text{s}$ can be extracted.

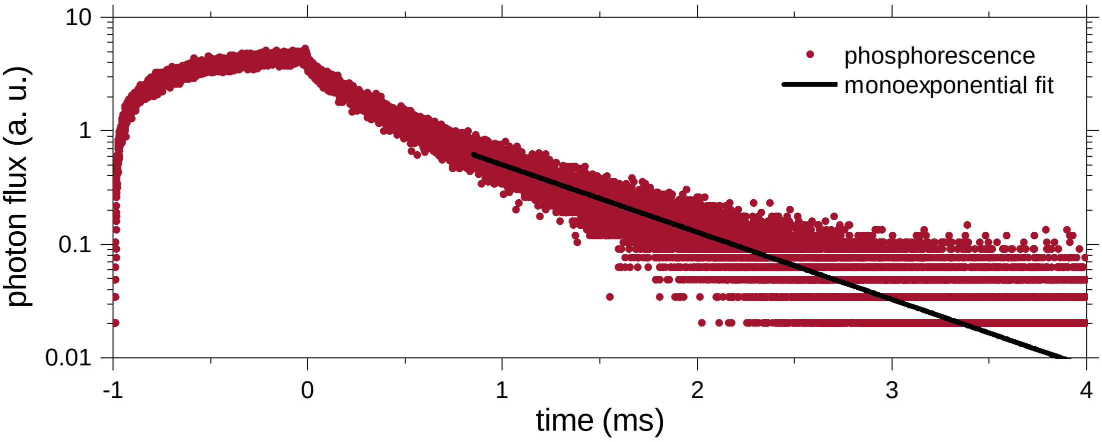

Figure 4.3: Phosphorescence decay of a PdP SURMOF thin film after 1 ms excitation at 525 nm with a power density of 58 mW cm^{-2}.

The triplet lifetime of PdP in the SURMOF configuration is longer than the corresponding value of a similar compound, PdTPP, dissolved in toluene, for which a phosphorescence lifetime of $(498 \pm 40)\,\mu\text{s}$ was reported [106]. The extended lifetime in the SURMOF can be explained by the suppression of non-radiative decay pathways due to the rigid structure of the molecular framework and the absence of solvent molecules [107].

4.2 Triplet Exciton Transport

Having established how excitons are formed and determined the intrinsic lifetime of the triplet exciton in the PdP SURMOF, we turn to investigating their motion inside the organic framework by means of TAS.

Acknowledgments and Contributions

The experiments in this section were conceived by the author and Ian A. Howard. The PdP linkers were designed and synthesized by Ganapathi Emandi and Mathias O. Senge. Nicolò Baroni and Michael Oldenburg prepared PdP SURMOF samples with the guidance of Christof Wöll. TAS and absorbance experiments were performed by the author. Data analysis and modeling were performed by the author with support by Ian A. Howard.

4.2.1 Transient Absorption Experiments

During the TAS experiments, the thin film sample is kept at room temperature under dynamic vacuum ($< 10^{-4}\,\text{Pa}$). The Q-switched pulsed laser (see section 3.1.2) is used to excite the sample at 532 nm and the TAS system is used in long delay and transmission mode.

The whole spectrum can be attributed to the porphyrin triplet exciton state. The broad, negative signal is caused by PIA, i. e. excitation of triplet excitons to higher excited states. This signal is strongest where triplet excited-state absorption is highest, in our case between 450 nm and 500 nm. The spectral shape is consistent with the reported absorption cross-section of the lowest triplet state in meso-tetrakis(4-N-methyl-pyridiniumyl) porphyrin (TMPyP) in different solvents [108]. Additionally, a small cusp is visible in the TAS spectra around 530 nm, which is caused by a positive GSB contribution: the pump laser partially depletes the porphyrin ground state, which absorbs here (see Figure 4.1), leading to increased transmission. As both the positive GSB and the negative PIA are linked to the same excited state species (the triplets excitons) their relative weight does not change and the resulting net negative TAS spectra at each delay time have identical shape.

The decay kinetics of the triplets differ from the PL measurements in that the lifetime is significantly shorter. This can be explained by TTA, which competes with radiative decay and thus reduces the effective triplet lifetime. The effect can best be observed by performing TAS measurements at different pump intensities and comparing the normalized kinetics (integrated from 460 nm to 500 nm for best signal strength), as shown in Figure 4.5. As TTA requires two triplets to meet, the process depends non-linearly on the triplet concentration and the decay rate becomes faster with increasing pump power.

Furthermore, we can conclude from this data, that the porphyrin chromophores in the SURMOF are overall well-connected. Structural defects, such as an uneven surface, residual individual linkers, growth inhomogeneities or not-aggregated MOF sheets can lead to isolated linker molecules (see Figure 4.6). Triplet excitons on such chromophores are immobile and thus cannot participate in TTA. Instead, they decay with their monomolecular lifetime of 730 µs, which would result in a long-lived contribution to the PIA signal on that timescale. The absence of such a contribution is clear evidence that the majority of the PdP molecules in the system are well-connected in the SURMOF bulk. This is consistent with the significant difference between the absorption spectra of linker solution and SURMOF. If a large fraction of PdP molecules in the SURMOF

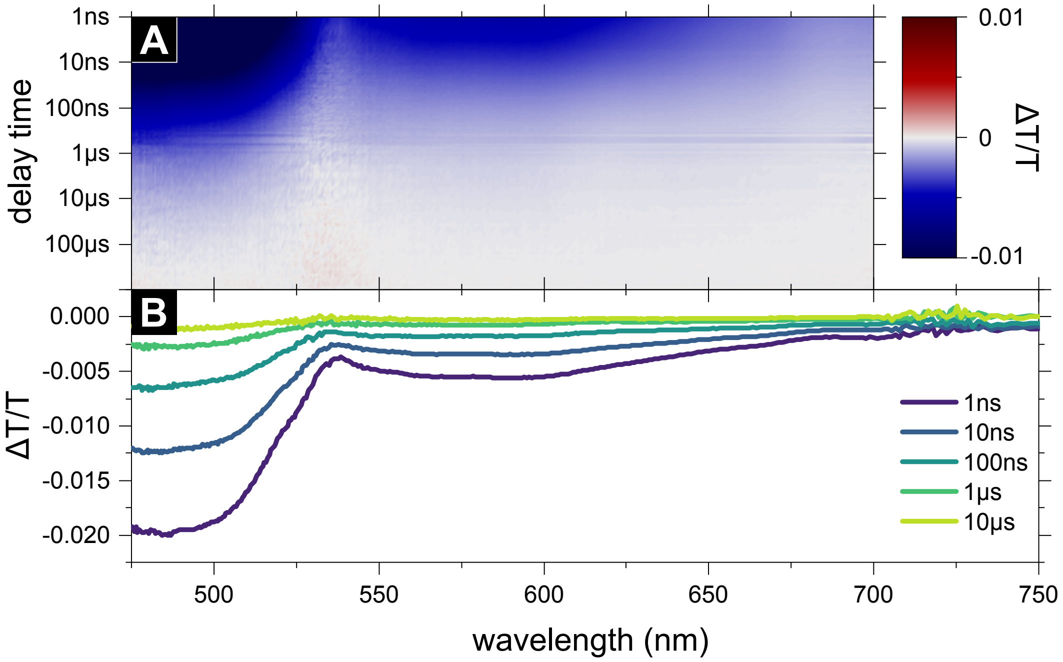

Figure 4.4: **(A)** 2D TAS data of a pristine PdP SURMOF thin film excited at 532 nm (70 µJ cm^{-2}). **(B)** Transient absorption spectra obtained from (A) by integrating over short time intervals at the given delay times.

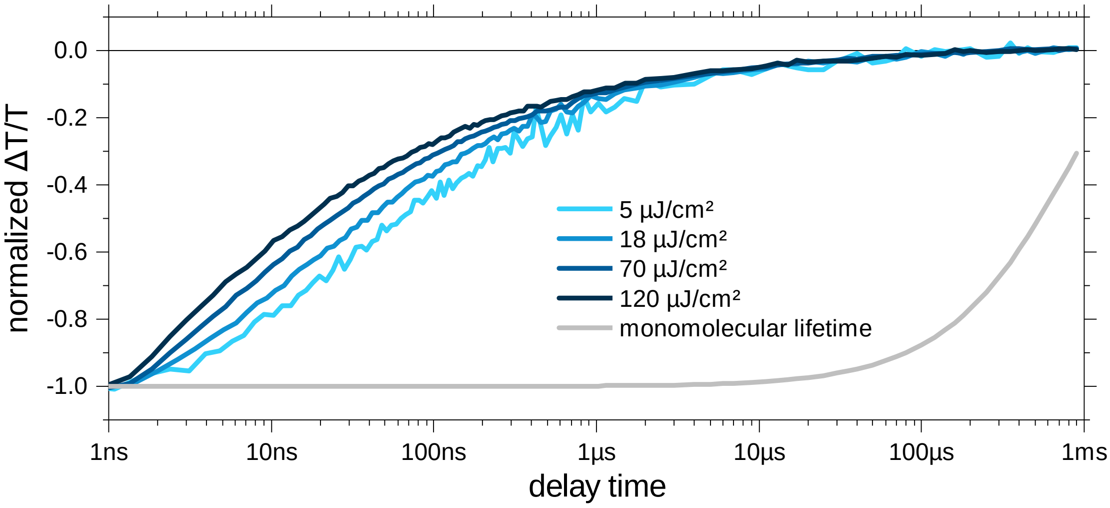

Figure 4.5: Normalized kinetic traces of the PdP SURMOF PIA signal (integrated from 460 nm to 500 nm) for different excitation fluences. A curve with the monomolecular triplet lifetime in the SURMOF is drawn in gray for comparison.

were isolated, the absorption spectra should be more similar to the solution. From the noise-level of the TAS data an upper limit of 5 % for the fraction of trapped triplets can be estimated.

4.2.2 Calculation of Initial Concentrations

To perform a more quantitative analysis of the TAS dataset, the relative $\Delta T/T$ values can be converted to triplet concentrations. This requires knowledge of the excitation fluence H, the film thickness d, and the photon energy E as well as the absorbance A at the pump wavelength. This allows to calculate the amount of absorbed photons per volume, which is identical to the concentration of created singlet excitons per pulse:

$$[S]_0 = \frac{H\left(1-10^{-A}\right)}{Ed}\,. \tag{4.1}$$

This calculation uses the thin film approximation, namely, that the excitation light is attenuated only weakly while passing through the film. Thus, the resulting singlet concentration is assumed to be constant over the whole thickness. To examine whether the thin film approximation is valid in this case, we can calculate the actual exciton concentration profile over the thickness of a film. Absorption in the film causes an exponential attenuation in light intensity (known as the Lambert-Beer law). Accordingly, the generation of excitons follows the same profile and the singlet exciton concentration $[S]$ can be written as

$$[S](z) = [S]_0 \frac{A\ln(10)}{1-10^{-A}} 10^{-Az/d}\,, \tag{4.2}$$

where A is the absorbance and z is the depth coordinate, i. e. the position along the light propagation direction, with $z = 0$ at the front interface of the film and $z = d$ after the film's thickness has been traversed. This can be expressed by the dimensionless quantities $\tilde{z} = z/d$ and $[\tilde{S}](\tilde{z}) = [S](\tilde{z})/[S]_0$. The depth profile of $[\tilde{S}](\tilde{z})$ is shown in Figure 4.7 for several absorbances (typical values for the PdP SURMOF samples in this work are between $A = 0.2$ and $A = 0.3$). The deviation from the thin film approximation increases with the material's absorbance. However, as the approximation underestimates the concentration at the top of the sample, it likewise overestimates the values at the bottom. Considering the material's bulk, the deviations do roughly cancel out. We will return to this discussion later and estimate the potential impact on the results of our analysis (see page 53).

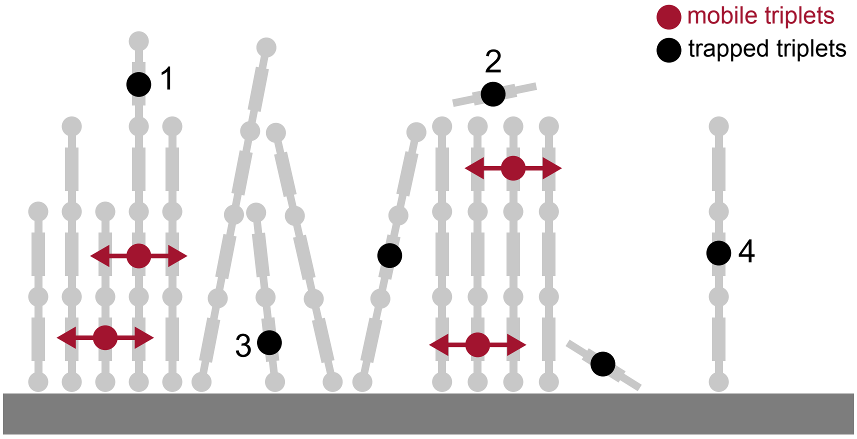

Figure 4.6: Schematic drawing of different defects in a SURMOF structure (shown as a side-view of sheets) that can result in isolated linker molecules. Triplet excitons that form on such linkers (black circles) are trapped and immobile, as opposed to the highly mobile triplets in the bulk (red circles). Isolated linkers can for example occur because of a jagged, uneven top surface caused by unequal growth (1), residual unconnected linkers that have not been washed off (2), inhomogeneities in SURMOF growth (3), and free-standing or unaggregated MOF sheets (4).

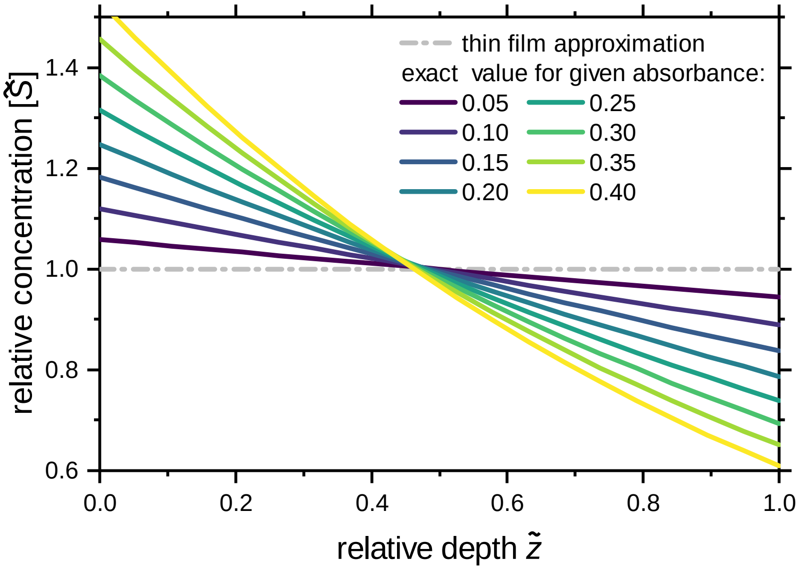

Figure 4.7: Comparison of the depth profile of the dimensionless singlet exciton concentration $[\tilde{S}]$ to the thin film approximation.

Because the ISC rate in PdP is close to unity, we can assume the initial triplet exciton concentration to be identical to the singlet concentration: $[T]_0 \approx [S]_0$. Therefore, $[T]_0$ should be proportional to H. Experimentally, however, the relationship between the pump fluence and the initial PIA signal height is not linear, as shown in Figure 4.8. The data can be fit well with a power function $f(H) \propto H^b$, where $b = 1$ would correspond to the linear case. However, we find $b = 0.71$, so the triplet concentration is below the linear expectation at high pump intensities. This fluence-dependent deviation is caused by losses in triplet concentration via TTA during the instrument response time. To obtain the actual value of $[T]_0$ after these initial losses, we quantify the deviation from linearity by comparing a linear extrapolation of the lowest two excitation fluences with the experimental data (dashed line in Figure 4.8). Dividing these two values gives a correction factor $\xi(H)$, which we can use to correct the values from Equation 4.1:

$$[T]_0 = \xi(H)[S]_0\,. \tag{4.3}$$

The correction factor can be understood as the survival fraction of triplet excitons during the instrument response time. For example at the highest fluence in Figure 4.8, the correction factor is $\xi(280\,\mu\mathrm{J\,cm^{-2}}) = 0.51$, so roughly half of the initially created triplets recombine via TTA.

The TAS signal is proportional to the concentration in case of a single excited state species. Therefore, the TAS kinetics can be rescaled by normalizing them to their initial maximum and multiplying them with $[T]_0$. The resulting kinetics correspond to the triplet concentration over time, $[T](t)$.

4.2.3 Dimensionality of the Transport

The dimensionality of the transport process can be determined from the TTA rate coefficient $\gamma(t)$. The triplet concentration $[T](t)$ is known from the TAS experiment and $\mathrm{d}[T]/\mathrm{d}t$ can be calculated from it. Hence, the TTA rate can be determined experimentally after solving the system's rate equation (Equation 2.11 on page 12) for $\gamma(t)$, which yields

$$\gamma(t) = -\left(\frac{\mathrm{d}[T]}{\mathrm{d}t} + k_{\mathrm{GS}}[T]\right)[T]^{-2} \approx -\left(\frac{\mathrm{d}[T]}{\mathrm{d}t}\right)[T]^{-2}\,. \tag{4.4}$$

The last step is a simplification which is valid when the monomolecular decay is much slower than the pairwise annihilation rate ($k_{\mathrm{GS}} \ll \gamma(t)[T]$), as is the case for our data. The factor f in Equation 2.11 was chosen as $f = 1$.

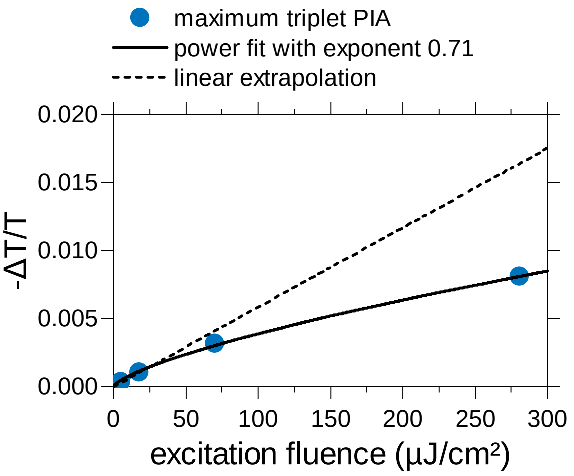

Figure 4.8: Determination of the correction factor ξ for calculating the triplet exciton concentrations. The initial maximum of the triplet PIA signal does not scale linearly with excitation intensity. Instead, a power law with an exponent of 0.71 best describes the relationship.

As described in section 2.1.8 and assuming that the quintet state is inaccessible, in 3/4 of all triplet-triplet encounters one triplet decays while the other survives ($f = 1$), whereas in the remaining 1/4 no triplets survive the encounter ($f = 2$) and one singlet exciton remains. However, as the ISC yield in PdP is close to unity [43, 44], this singlet can quickly convert to a triplet again:

$$\mathrm{T_1} + \mathrm{T_1} \rightarrow \begin{cases} \mathrm{T_1} + \mathrm{S_0} \\ \mathrm{S_1} + \mathrm{S_0} \rightarrow \mathrm{T_1} + \mathrm{S_0} \end{cases} \tag{4.5}$$

In both cases, one triplet exciton survives the bimolecular encounter, therefore $f \approx 1$.

Figure 4.9 shows a plot of Equation 4.4 for the TAS data, which reveals that $\gamma(t)$ is decreasing over time. This suggests that triplet exciton transport is 1D and not a 3D process, as in the latter case $\gamma(t)$ would tend to a constant non-zero value. Only data for the two highest excitation fluences are shown and used in the analysis as they have the best signal-to-noise ratio. The 1D and 3D equations (Equations 2.13 and 2.12) are fit to the experimental data. The 3D model fits poorly,[1] whereas the 1D model matches the data well for the optimized parameter $\gamma_0 = (8.2 \pm 0.2) \times 10^{-16}\,\mathrm{cm^3 s^{-1/2}}$. Thus, triplet diffusion occurs preferentially in the direction of closest chromophore spacing, that is between adjacent SURMOF sheets.

The parameter γ_0 allows to validate the simplification in Equation 4.4. The monomolecular rate is $k_{\mathrm{GS}} = 1.37 \times 10^3\,\mathrm{s^{-1}}$, whereas, for example, at $t = 100\,\mathrm{ns}$ the TTA rate is $\gamma(t)[T] = 3.34 \times 10^5\,\mathrm{s^{-1}}$. Overall, the condition $k_{\mathrm{GS}} < \gamma(t)[T]$ holds true until roughly 60 μs.

4.2.4 Diffusion Constant, Hopping Rate and Diffusion Length

From γ_0, some interesting material parameters can be derived. For instance, the diffusion coefficient can be calculated from Equation 2.14 as $D = 2.7 \times 10^{-4}\,\mathrm{cm^2\,s^{-1}}$ and the triplet exciton hopping rate as $k_{\mathrm{hop}} = 1.5 \times 10^{11}\,\mathrm{s^{-1}}$, which are excellent values for an organic material system (see discussion in section 7.1).

Another figure of merit is the diffusion length, which can be calculated using Equation 2.9 as $L_{\mathrm{D}} = 6.3\,\mu\mathrm{m}$. This assumes that 1D hopping at the rate k_{hop} continues for the monomolecular triplet lifetime of 730 μs. In

---

[1] The interaction radius R in Equation 2.12 is set to a reasonable value of 1 nm. However, values up to $R = 100\,\mathrm{nm}$ can be chosen without observing a significant deviation from the shape shown in Figure 4.9. Only for even higher values of R of several 100 nm does the 3D function fit the data adequately. As R describes the distance at which two particles react (here: two triplets annihilate) such large values are highly implausible and we thus consider the 3D function to not fit the data sufficiently under realistic conditions.

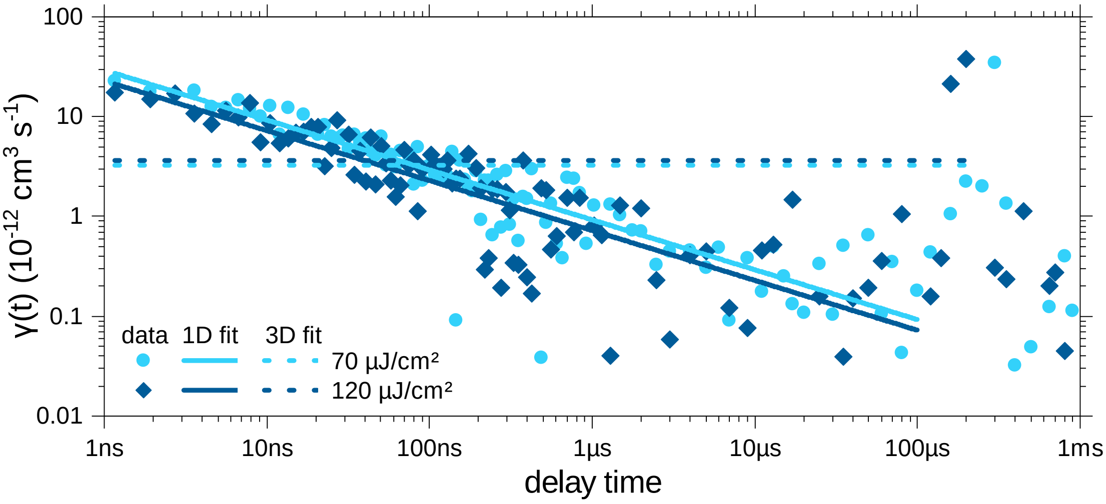

Figure 4.9: Calculated values for the TTA rate coefficient $\gamma(t)$ for two excitation fluences based on the TAS data shown in Figure 4.5. Both a 1D and a 3D diffusion model are fitted to the data.

other words, this is the average distance a triplet exciton travels during its lifetime, unless it is quenched (e. g. by TTA) or otherwise "stopped" (e. g. by lattice defects such as crystal grain boundaries).

4.2.5 Discussion of Uncertainty Boundaries

As mentioned earlier (page 50), the value of the initial triplet concentration $[T]_0$ was assumed to be uniform over the whole film thickness by the thin film approximation. As the actual value deviates (depending on the depth in the film) from this approximation, the values for γ_0, D, k_{hop} and L_D extracted above are average values, which are representative for the bulk of the material. However, we can recalculate these parameters for initial triplet concentrations that are 30 % above or below the thin-film-approximation value. For example, as $D \propto \gamma_0^2 \propto [T]_0^{-2}$, an increase of 30 % in $[T]_0$ leads to a 40 % decrease in D. Upper and lower limits calculated this way are listed in Table 4.1. Even at the extreme limits of $[T]_0$ deviations of ±30 %, the impact on the extracted parameters is sufficiently minor, as the most relevant information lies in their order of magnitude, which is only slightly affected.

4.3 Summary

This chapter established that triplet excitons are the only long-lived excited state species in a PdP SURMOF thin film. Triplets can efficiently move between porphyrin molecules in adjacent SURMOF sheets due to the high degree of order in the metal-organic framework. The porphyrin chromophores are well-connected, with less than 5 % of triplets excitons being located on isolated chromophores. Due to the long monomolecular triplet lifetime ($\tau \approx 730\,\mu\text{s}$) and fast hopping rate ($k_{hop} \approx 1.5 \times 10^{11}\,\text{s}^{-1}$), triplet excitons are able to travel several

Table 4.1: Extracted values for the diffusion coefficient D, the triplet hopping rate k_{hop} and the diffusion length L_D as well as the upper and lower limit assuming a deviation of ±30 % of the initial triplet concentration from the thin-film approximation.

parameter	unit	lower limit	value	upper limit
D	$10^{-4}\,\text{cm}^2\,\text{s}^{-1}$	1.6	2.7	5.5
k_{hop}	$10^{11}\,\text{s}^{-1}$	0.9	1.5	3.1
L_D	µm	4.8	6.3	9.0

micrometers along 1D paths in the material. This is an exciting result, however, mechanisms that reduce the triplet lifetime (for example quenching at impurities or by TTA) or restrict exciton movement (such as small crystal grains) can negatively affect the diffusion length. Such mechanisms will be discussed in the following sections.

5 Photostability of PdP SURMOFs

PdP SURMOFs have exciton transport properties which make them interesting for application in organic electronics or photon harvesting devices. However, a relevant criterion for the applicability of the material is its long-term stability and the effect of environmental conditions (such as exposure to light, heat or humidity) on its properties. In this chapter, the effect of prolonged illumination on the photoresponse of the PdP SURMOF material is investigated.

Acknowledgments and Contributions

The experiments in this section were conceived by the author and Ian A. Howard. The PdP linkers were designed and synthesized by Ganapathi Emandi and Mathias O. Senge. Nicolò Baroni, Michael Oldenburg and Ritesh Haldar prepared PdP SURMOF samples with the guidance of Christof Wöll. MALDI-ToF-MS experiments were performed by Ritesh Haldar and analyzed by the author. The trEPR experiments were performed in collaboration with the “Helmholtz-Zentrum Berlin für Materialien und Energie” by Rowan W. MacQueen, Felix Kraffert, Jan Behrends and Klaus Lips, who were also responsible for the analysis and interpretation of the data. PL, absorbance and TAS experiments were performed by the author. Data analysis and modeling was performed by the author with support by Ian A. Howard.

5.1 Changes Caused by Prolonged Illumination

Experiments already performed on a pristine PdP SURMOF thin film – namely absorbance, PL and TAS – are repeated for extended illumination times. Again, the samples are kept under dynamic vacuum ($< 10^{-4}$ Pa) and at room temperature during the illumination. In each case, prolonged light exposure clearly has an impact on the results, which will be discussed below.

Photoluminescence

During continuous excitation with a 525 nm CW laser diode at a power density of 5.6 W cm^{-2}, the SURMOF’s PL spectrum changes drastically over the course of 32 h, as shown in Figure 5.1. The phosphorescence signal drops over time between 650 nm and 810 nm, whereas it rises for longer wavelengths. In contrast, the fluorescence peak at 615 nm is not affected by these changes. Therefore, the observed effects cannot be explained by ablation, framework disintegration or any other form of physical destruction of the SURMOF. To put the amount of illumination into perspective: During the 32 h exposure, around 380×10^{26} cm^{-3} photons were absorbed by the sample. This corresponds to over 500 days of continuous solar illumination (considering the visible absorption spectrum of a 200 nm thick PdP SURMOF film under AM1.5 conditions [109]).

Absorbance

A more subtle change is observed in the absorbance spectrum in Figure 5.2. Here, the SURMOF is exposed to 0.1 W cm^{-2} of 405 nm CW. After 17 h, the illumination is interrupted, the thin film removed from the vacuum container, and an absorbance measurement is taken. Subsequently, the illumination is continued for another 16 h, followed by a final absorbance measurement.

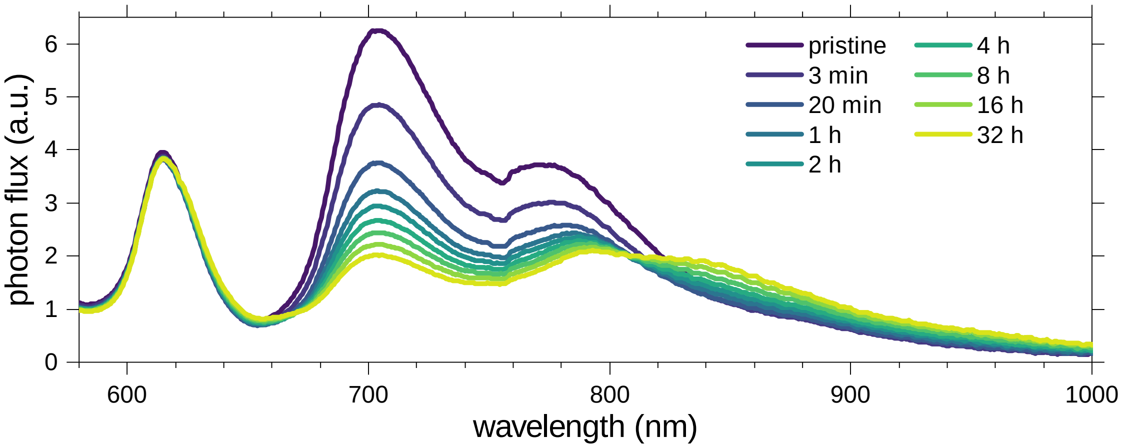

Figure 5.1: Changes in the PL intensity of a PdP SURMOF thin film over the course of 32 h of continuous CW excitation at 525 nm ($5.6\,\mathrm{W\,cm^{-2}}$).

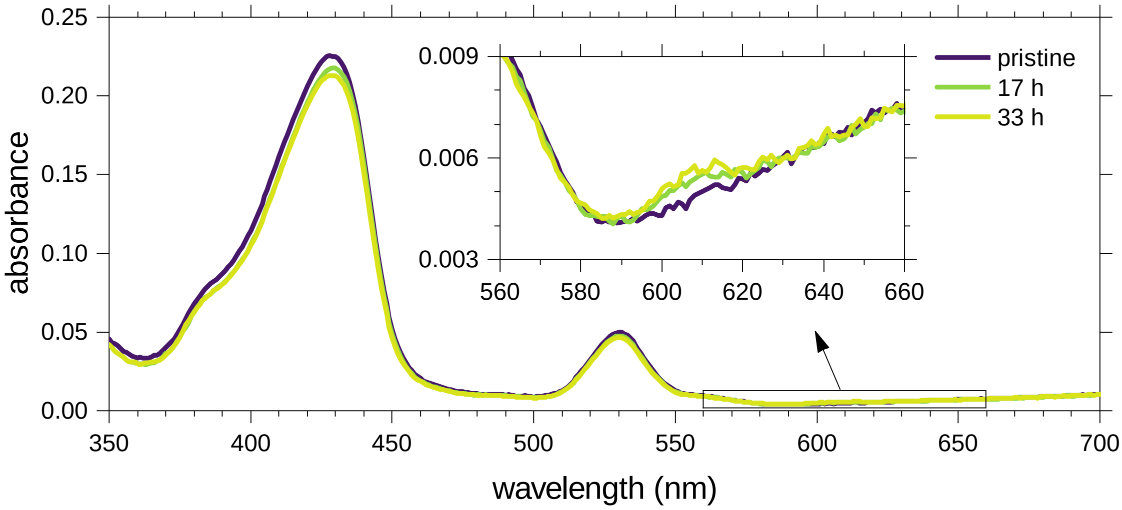

Figure 5.2: Changes in the absorption of a PdP SURMOF thin film over the course of 33 h of continuous CW illumination at 405 nm ($0.1\,\mathrm{W\,cm^{-2}}$).

For the most part, the spectrum remains unaltered. Only two regions exhibit a change: The Soret band's absorbance slightly decreases during the illumination, whereas the region between 600 nm and 620 nm exhibits a small increase. The loss of absorption in the Soret band maximum amounts to 5.1 %. Hence, at least this percentage of porphyrin molecules have been lost during illumination.

The absorption increase at 620 nm can be interpreted as the appearance of a previously absent substance, whereas the Soret band's decrease hints at a loss of a fraction of the PdP linker molecules. This seems to be at odds with the observation that the fluorescence intensity remains unchanged during illumination. A possible explanation is that the newly introduced substance emits in the same wavelength region and compensates the loss of PdP fluorescence.

Transient Absorption

Lastly, the TAS experiment are repeated under extended illumination. The PdP SURMOF thin film is excited by a 532 nm pulsed laser at $120\,\mathrm{\mu J\,cm^{-2}}$ for 15.4 h. As acquisition of a full 2D TAS data surface takes 33 min, the experiment is repeated 28 times.

As described earlier (see e. g. Figure 4.4), in the pristine sample the decay of a single PIA-dominated triplet spectrum is observed (see Figure 5.3A). After 15.4 h of illumination, a new positive GSB feature has appeared around 615 nm (see Figure 5.3B). The temporal evolution of this feature is clearly distinct from the triplet exciton: The 615 nm signal starts negative before it increases, turns positive and then decays to zero. In Figure 5.3C the kinetic traces in this (450 nm to 500 nm, labeled (2)) and the triplet-dominated wavelength region (450 nm to 500 nm, labeled (1)) are shown before and after the extended light exposure. In the pristine material, both regions exhibit the same decay, which is consistent to the earlier assertion that the whole spectrum is linked to these excitons. Furthermore, the triplet kinetics remain unchanged during illumination. Only the 615 nm kinetic change and exhibit the aforementioned rise from a negative PIA-dominated to a positive GSB signal, crossing zero after 100 ns. Interestingly, at late times ($> 1\,\mu s$), the new feature decays with the same time constant as the triplet excitons, as can be seen by the comparison of the absolute values in Figure 5.3D. This observation will be of importance later on.

Furthermore, it is worth noting that the GSB appears in the same wavelength region as the change in the absorption spectrum above. This can best be seen in Figure 5.3E, where the TAS spectrum integrated from 100 ns to 300 ns is tracked over illumination time. The GSB feature grows over time, which mirrors the light-induced increase of the absorbance peak in this very wavelength region. Both effects are indicative of the same material change. In other words, the introduction of a new substance – or photoproduct – is reflected by its absorption and the transient bleach of this ground-state absorption.

Rate of Change

For application purposes it is useful to know how fast this change in material composition occurs. The actual concentration of photoproduct sites is unknown. However, the changes in PL intensity and the GSB signal can be taken as proxy values, as they reflect the increase of photoproduct concentration. In Figure 5.4, the relative changes in the TAS GSB region and the steady-state phosphorescence intensity are shown over the cumulative concentration of absorbed photons n. As before, this can be compared to the corresponding duration of solar illumination under AM1.5 conditions [109] (considering the visible part of the absorption spectrum only and assuming a 200 nm thick PdP SURMOF film): A value of $n = 10^{26}\,\mathrm{cm}^{-3}$ corresponds to 32.4 h of continuous illumination by sunlight.

The PL experiments were performed in a high ($5.6\,\mathrm{W\,cm}^{-2}$ at 525 nm CW) and low ($0.1\,\mathrm{W\,cm}^{-2}$ at 405 nm CW) excitation density regime. In both cases, the decay in phosphorescence intensity as a function of n is similar. Therefore, the creation of photoproduct sites does not depend on the power density or wavelength but rather the number of absorbed photons. This holds also true compared to the GSB data, which was taken under pulsed excitation.

The signals in the PL experiments exhibit an initial fast component followed by a much slower decay. The TAS data only tracks the former process. It is reasonable to empirically quantify the rate of change by fitting a mono-exponential function $f(n) \propto \exp(n/\nu) + f_0$ to all three datasets. The offset f_0 approximates the long decay component, whereas the parameter ν corresponds to the photon dose required for the fast component to decay to $1/e$ of its magnitude. A global fit over the TAS and both PL datasets (for absorbed photon concentrations up to $6 \times 10^{26}\,\mathrm{cm}^{-3}$) results in $\nu = 1.53 \times 10^{26}\,\mathrm{cm}^{-3}$. This corresponds to around 50 h under solar irradiation.

As the actual dynamics of photoproduct creation are not understood, the choice of an exponential function is arbitrary. However, the global fit shows that the rate of change is independent of the excitation regimes (pulsed, high-intensity CW, low-intensity CW).

It is also noteworthy that a mono- or bi-exponential fit does not match the slow decay component. Instead, it is described well by power-law function $f(x) \propto x^{\alpha}$ with a fit coefficient of $\alpha = -0.132\,83 \pm 0.000\,04 \approx -0.13$,

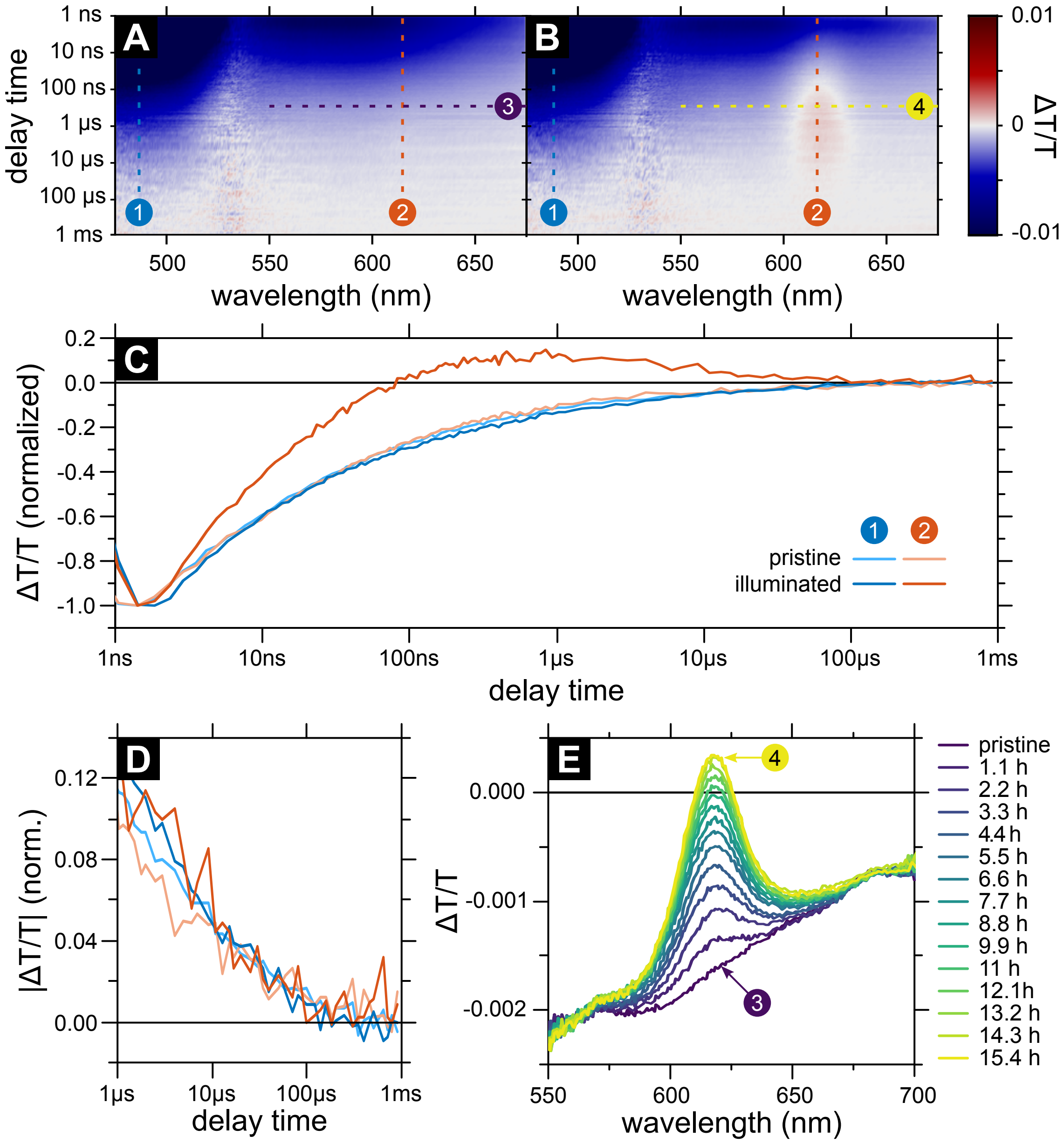

Figure 5.3: Effects of prolonged illumination of a PdP SURMOF thin film monitored by TAS in a **(A)** pristine film and **(B)** after 15.4 h of continuous excitation with the 532 nm pulsed pump laser at 120 µJ cm^{-2}. **(C)** Normalized TAS kinetic traces integrated over the triplet-dominated region 450 nm to 500 nm (1) and the photoproduct-dominated region 605 nm to 620 nm (2) for the pristine and illuminated samples from panels (A) and (B). **(D)** Comparison of the absolute values of the kinetic traces in (C) for delay times > 1 µs. **(E)** TAS spectra integrated over the time region between 100 ns and 300 ns. Spectra were taken at a 33 min interval, however, for clarity, only ever second spectrum is plotted here. Adapted with permission from Adams *et al.* [1].

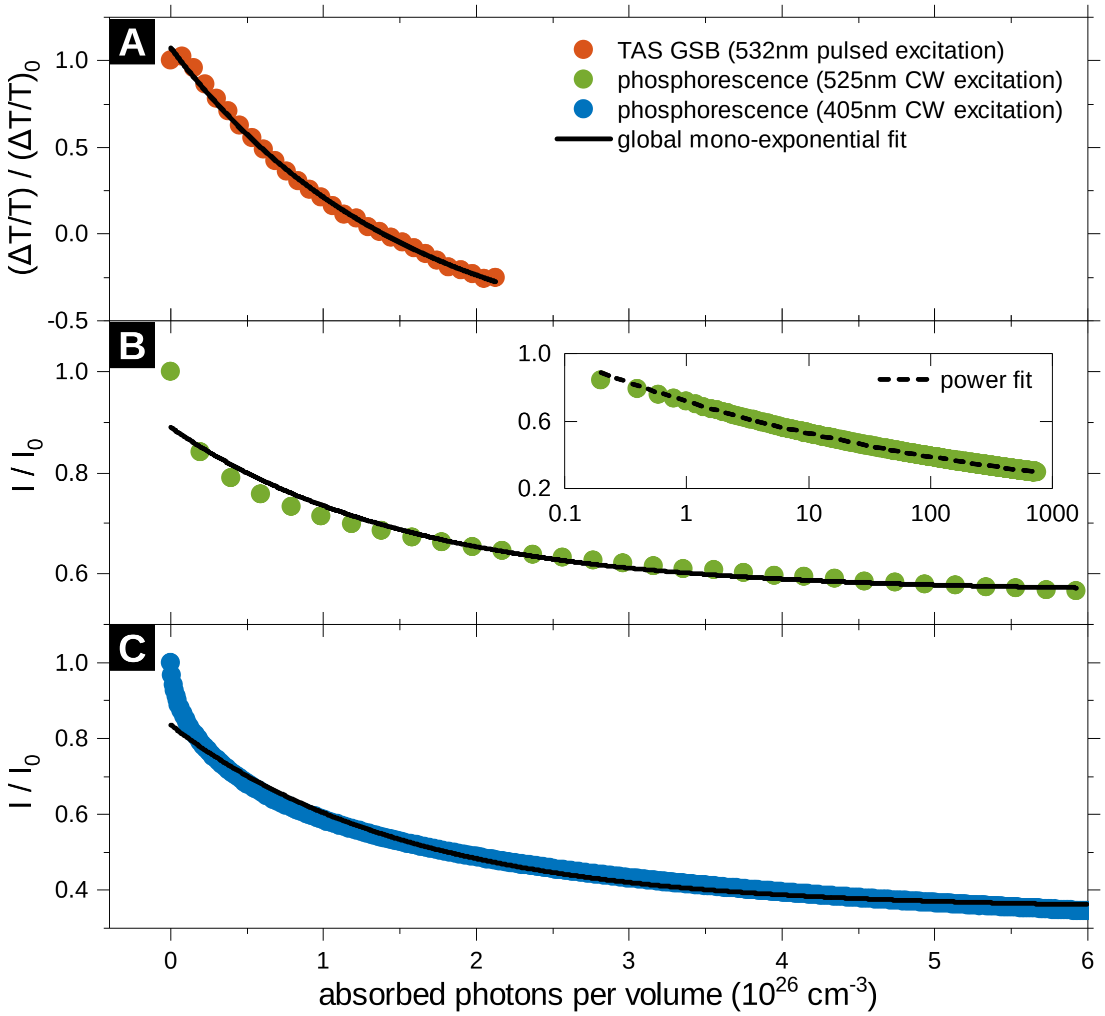

Figure 5.4: Relative change in TAS and PL signals during illumination. The black solid line corresponds to a global fit over all three datasets in the region up to $6 \times 10^{26}\,\mathrm{cm}^{-3}$ which yields a common decay rate $\nu_1 = (1.53 \pm 0.01) \times 10^{26}\,\mathrm{cm}^{-3}$. **(A)** Relative change in TAS signal in the GSB region (605 nm to 620 nm) during illumination with a 532 nm pulsed laser (500 Hz) at $120\,\mu\mathrm{J\,cm}^{-2}$ at room temperature under dynamic vacuum ($< 10^{-4}$ mbar). This is based on the data as shown in Figure 5.3. **(B)** Relative change in phosphorescence (700 nm to 720 nm) during illumination with a 525 nm CW laser at $5.6\,\mathrm{W\,cm}^{-2}$ at room temperature under dynamic vacuum ($< 10^{-4}$ mbar). The horizontal axis range of $6 \times 10^{26}\,\mathrm{cm}^{-3}$ corresponds to 30 min of illumination. This is based on the data as shown in Figure 5.1. The inset shows an extended range and a power fit for the slow decay component which yields a power coefficient $\alpha \approx -0.13$ **(C)** Relative change in phosphorescence (700 nm to 720 nm) during illumination with a 405 nm CW laser at $0.1\,\mathrm{W\,cm}^{-2}$ at room temperature under dynamic vacuum ($< 10^{-4}$ mbar). The horizontal axis range of $6 \times 10^{26}\,\mathrm{cm}^{-3}$ corresponds to 22 h of illumination.Adapted with permission from Adams *et al.* [1].

as can be seen in the inset of Figure 5.4B. Interestingly, a power-law function does not match to the early decay. This difference in the time dynamic shows that the fast and slow component are likely linked to two distinct photochemical processes, that, however, lead to the same photoproduct.

Rank of the TAS Data Matrix

So far, only one additional species was considered to be present in the illuminated SURMOF. To confirm that this is correct and that not more excited-state species are introduced, the rank of the TAS data matrix is tracked over illumination time. This can be done by calculating the singular value decomposition (SVD) of each matrix,[1] as the effective rank equals the number of non-vanishing singular values σ_1, σ_2, $\ldots\sigma_n$. This is shown in Figure 5.5. In the pristine film, triplet excitons are the sole excited-state species and, accordingly, only the first singular value σ_1 is above the noise level: the rank of the matrix is 1. During the illumination, σ_2 rises constantly and therefore the data matrices can be considered as having rank 2. Higher-order singular values remain at the noise floor. Thus, only one additional excited-state species is necessary to explain the data. As σ_2 stays below 10 % of σ_1, the photoproduct state has a limited impact on the overall photoresponse. Please note that this purely mathematical analysis does not exclude the possibility that additional species are introduced that share the same decay kinetic as either the triplets or the photoproduct state, as that would make them indistinguishable in this analysis. Thus, further examination is necessary.

5.2 A Possible Candidate for the Photoproduct

So far, the exact nature of the photoproduct remains open. Under illumination, porphyrin can undergo a photolytic reaction that leads to the reduction of one double bond in the porphyrin macrocycle. This process creates either the unstable product phlorin or the stable chlorin [110, 111]. The latter is a good candidate for the photoproduct observed in the PdP SURMOF. Notably, palladium chlorin (PdC) in different solutions was reported to absorb around 603 nm [112] or 612 nm [110], which matches well to the emergent feature in the PdP SURMOF absorption and the GSB. This absorption corresponds to the Q-band component which is suppressed in metalloporphyrin but is significant in metallochlorin (see section 2.2.2). Furthermore, PdC does not exhibit steady-state emission below 750 nm. Instead, it emits more light than PdP above 850 nm [112]. This matches the observed change in PL shown in Figure 5.1.

---

[1] The computation is performed using MATLAB's built-in `svd()` function.

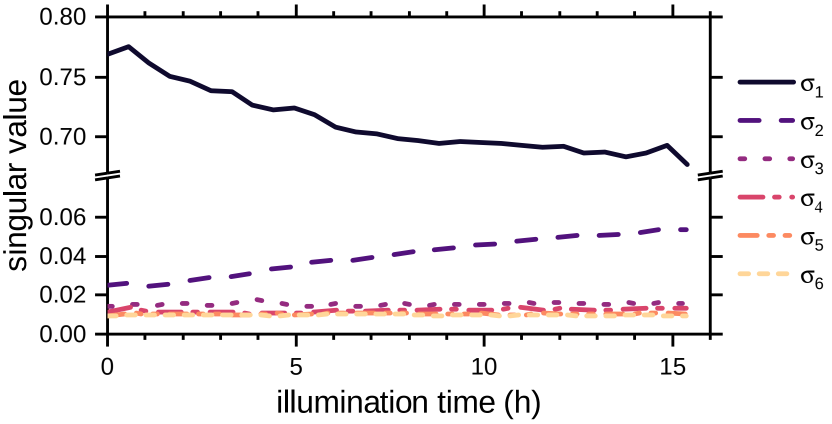

Figure 5.5: Singular values obtained by SVD from TAS data matrices repeatedly taken over the course of 15.4 h illumination time. Only the first six singular values $\sigma_1\ldots\sigma_6$ are shown, as higher order singular values (starting from σ_3) stay consistently at the noise level and can be neglected.

The light-induced reduction of porphyrin to chlorin relies on the presence of a proton source. In an idealized SURMOF under vacuum conditions, no such source exists. However, there might be residual solvent (ethanol) or water being trapped in the SURMOF's pores. It is known that water molecules form hydrogen bonds to the paddlewheel's axial positions [113]. These are difficult to remove, even under extended dynamic vacuum as in the experiments presented here. Alternatively (or additionally), traces of ethanol might be directly photo-oxidized to acetaldehyde, providing the hydrogen atoms required for the reduction of porphyrin to chlorin.

In an attempt to prove that the photoproduct can indeed be identified with PdC, MALDI-ToF-MS measurements were performed on a pristine and an illuminated PdP SURMOF film. MALDI-ToF-MS is a sensitive method able to detect small material quantities (see section 3.9).

A pristine PdP SURMOF is prepared and illuminated for 33 h by a 405 nm CW laser at 0.1 W cm^{-2} (10^{27} cm^{-3} absorbed photons). Illumination was performed at room temperature under dynamic vacuum ($< 10^{-4}$ Pa). MALDI-ToF mass spectra of the PdP SURMOF before and after degradation are shown in Figure 5.6. They are compared to the theoretical spectra of PdP and PdC.[2] The isotopic m/z distribution for PdP ($m/z = 807.075$ Da) obtained for a pristine PdP SURMOF resembles the calculated pattern ($m/z = 807.155$ Da). The mass spectrum of the irradiated SURMOF exhibits only a small increase at $m/z = 809.967$ Da and remains otherwise very similar to the pristine film. This is consistent with the above observation that only a small fraction of PdP molecules form photoproducts.

As the calculated m/z distributions for PdP and PdC overlap significantly, identification of a small quantity of PdC in the illuminated sample is not straightforward. The change in the m/z intensity distribution is at least

---

[2] Theoretical spectra are calculated using the web service ChemCalc [114].

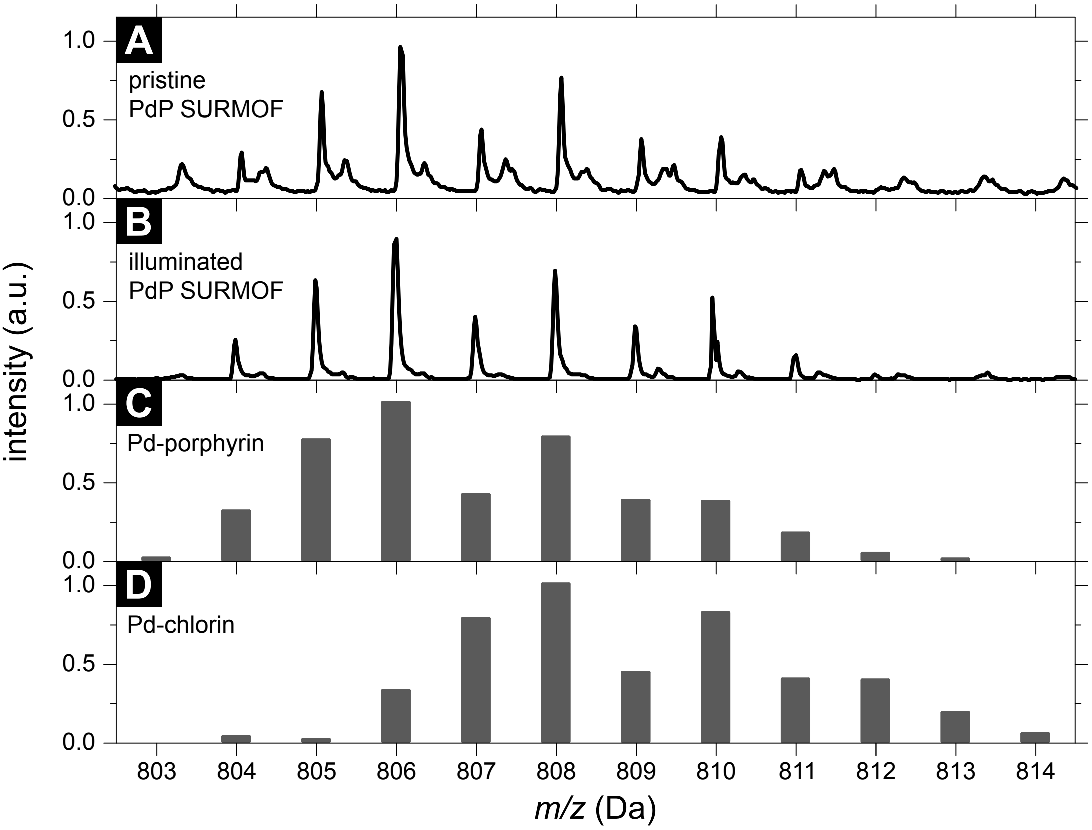

Figure 5.6: MALDI-ToF mass spectroscopy data of a PdP SURMOF thin film **(A)** in pristine condition and **(B)** after 33 h of illumination. Additionally, the theoretical isotopic m/z distribution is shown for **(C)** PdP and **(D)** PdC. Adapted with permission from Adams *et al.* [1].

consistent with PdC formation. This, together with the spectroscopic measurements, lends strong support to the hypothesis that chlorin is the photoproduct introduced into the PdP SURMOF during illumination. However, as no conclusive proof of this hypothesis was possible, the material introduced by illumination continues to be called “photoproduct” throughout this text.

5.3 Influence of the Photoproduct on the SURMOF’s Photoresponse

We have seen earlier in the TAS data (Figure 5.3) that the creation of photoproduct sites inside the PdP SURMOF introduces a new excited state. The spectral position of this GSB feature coincide with the ground state absorption of the photoproduct. Thus, the new state is an excited state of the photoproduct.

Time-Resolved EPR

To identify the nature of this new state, trEPR experiments are performed on an photoreacted PdP SURMOF thin film (accumulated absorbed photon dose on the order of $10^{27}\,\mathrm{cm}^{-3}$). Due to long measurement times under constant illumination, it was not possible to perform trEPR experiments on a pristine film. Instead, a solution of $0.5\,\mathrm{mmol\,L}^{-1}$ PdTPP in toluene is used as reference. For the SURMOF sample, the thin film on glass was broken into cm-long shards to fit into a quartz capillary tube, which was then deaerated and sealed under helium atmosphere. Experiments are performed using microwave radiation at X (9.6 GHz) and Q band (34 GHz) frequencies. The samples were kept at 20 K to improve the signal-to-noise ratio.

A detailed analysis of the trEPR data was previously published [1]. Below, the most relevant results relating to this thesis are summarized.

A comparison of X and Q band data for both the photoreacted PdP SURMOF thin film and the PdTPP linker is shown in Figure 5.7. The EPR signal of the linker solution shows a pattern that has emissive and absorptive components. They represent microwave-driven transitions between different spin sub-levels separated by Zeeman splitting due to the external magnetic field. The data are consistent with a population of triplet excitons. A similar pattern – albeit with a decreased spectral width – appears in the SURMOF’s EPR signal. The difference in width suggests that the PdP triplet excitons are spatially more extended in the SURMOF as compared to the linker solution, which can be related to the more ordered environment of the chromophores. Furthermore, the EPR signal of the photoreacted SURMOF has an additional sharp and strong emissive feature, which corresponds to a particle with spin 1/2. This new feature indicates the presence of a radical species and is likely linked to the excited state on the photoproduct. The spectra agree well with a model of the system (red lines in Figure 5.7; for details on the model please refer to the original publication [1]).

The temporal evolution of the radical signal (see Figure 5.7E) can be modeled by a mono-exponential function (convoluted with the instrument response) with a lifetime of 3.5 μs. Although this measurement was performed at 20 K, this value will be found to be in good agreement with the effective lifetime of the radical population obtained by TAS at room temperature. The triplet’s trEPR signal changes sign over time, which indicate that the spin polarization of the triplet population is driven by the microwave field. Hence, the true triplet lifetime is likely longer than in the trEPR trace.

Transient Absorption

So far, it is unclear whether the radical states are populated directly by the excitation pulse or whether they are created over time by quenching of porphyrin triplet excitons at a porphyrin:photoproduct interface. This question can be answered by comparing the TAS kinetics of the triplet-dominated PIA and the radical-featuring GSB region for different excitation fluences, as shown in Figure 5.8.

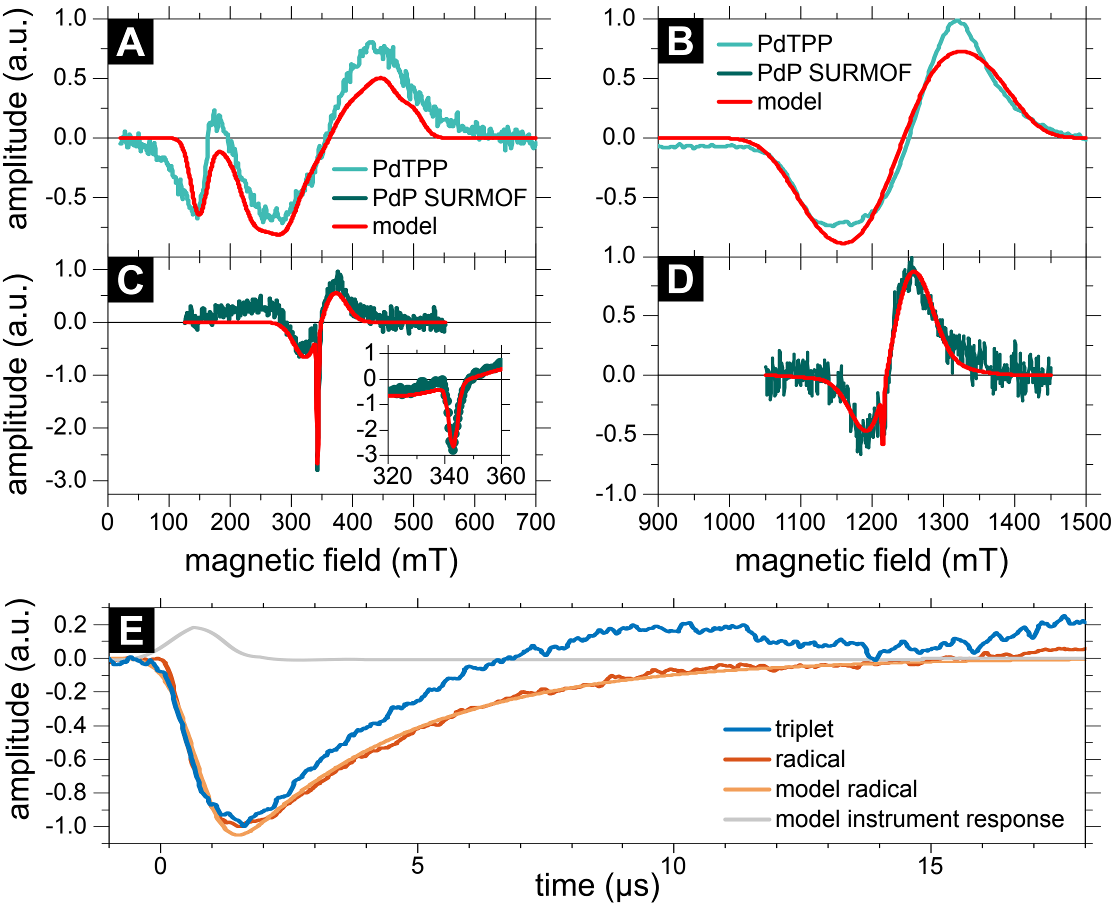

Figure 5.7: **(A)** X band and **(B)** Q band EPR spectra of PdTPP in solution. **(C)** X band and **(D)** Q band EPR spectra of a photoreacted PdP SURMOF thin film. The inset in (C) highlights the strong negative radical peak. All spectra are obtained by integrating over the first 500 ns after the excitation pulse. **(E)** Time evolution of the X band trEPR signal of a photoreacted PdP SURMOF. Adapted with permission from Adams *et al.* [1].

As before, the PIA signal shows a strong dependence on the excitation power density, which can be attributed to TTA. In the wavelength region from 605 nm to 620 nm, the triplet's negative PIA and the radical's positive GSB are superimposed. As we are interested in the radicals, the curves in Figure 5.8B are normalized to the maximum positive signal. The initial signal (up to 30 ns) shows the TTA-induced fluence-dependence of the triplets. In contrast, the normalized kinetics are identical from there on. This shows that the radicals do not partake in bi-molecular processes such as radical-radical or radical-exciton annihilation.

Therefore, the concentration of radical states should scale linearly with excitation pulse energy if the radical are directly created by light absorption. However, tracking the maximum of the GSB reveals a clearly non-linear behavior. The maxima (shown in Figure 5.8C) can be described well with a square-root function $f(x) \propto \sqrt{x}$. This is consistent with a bimolecular deactivation pathway. As such a pathway was just excluded for the radicals but is clearly present in the triplet exciton population, it is straightforward to infer that triplet excitons have to be the precursors to the radical states. In other words, once a mobile triplet diffusing through the SURMOF encounters a photoproduct site, it is quenched and a radical on said photoproduct is formed.

At late times, the decay of the radical population matches the triplet decay, as depicted in Figure 5.3D on page 58. This suggests that the lifetime of the radical state is short compared to that of the triplets. A mono-exponential fit to the four kinetic traces in Figure 5.3D yields a lifetime of $(3.7 \pm 0.3)\,\mu\text{s}$. This is the effective lifetime of triplet excitons at $120\,\mu\text{J}\,\text{cm}^{-2}$, which is much shorter than the monomolecular decay rate due to TTA. The slightly smaller radical population lifetime of $3.5\,\mu\text{s}$ obtained from the trEPR experiment at

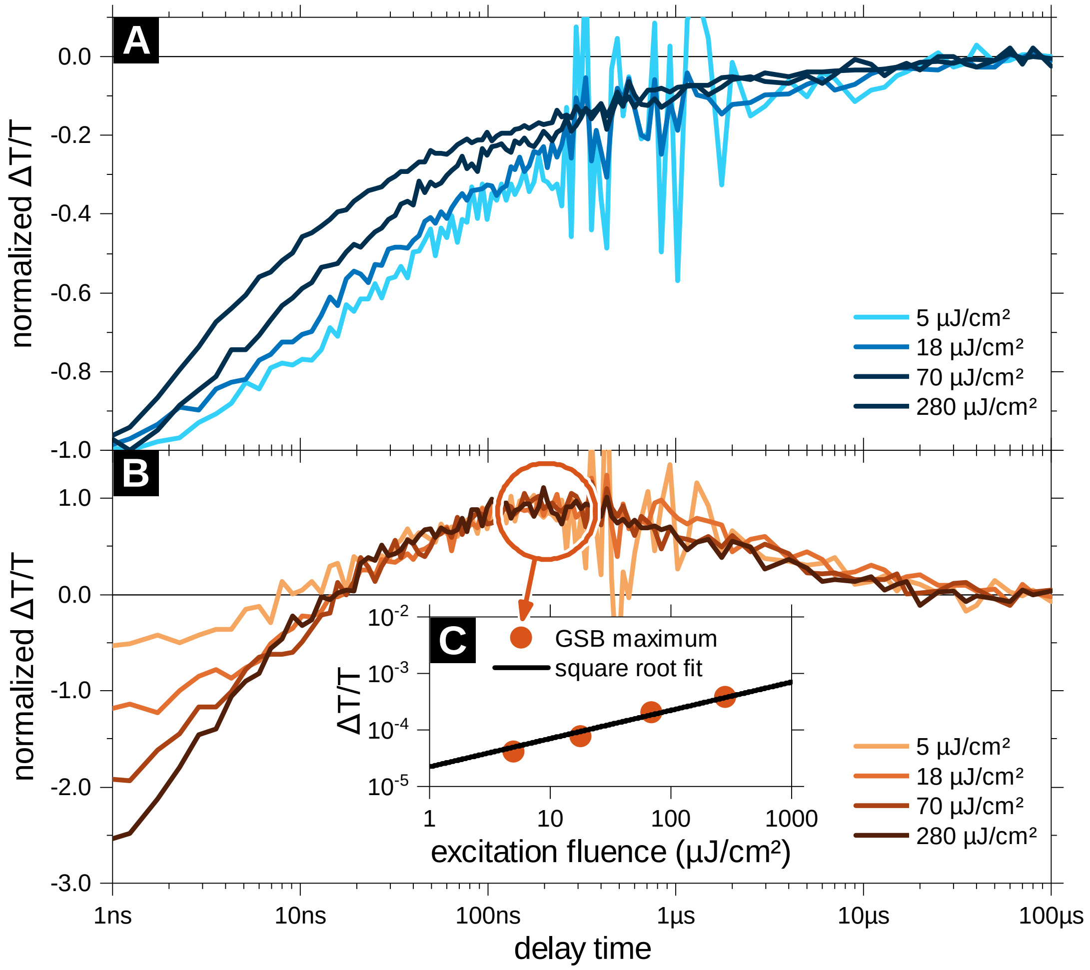

Figure 5.8: Normalized TAS kinetics in a photoreacted PdP SURMOF for different excitation fluences, integrated over **(A)** the triplet-dominated PIA (450 nm to 500 nm) and **(B)** the radical-featuring GSB (605 nm to 620 nm). **(C)** The maxima of the GSB over the excitation fluence can be fit with a square-root function. Adapted with permission from Adams *et al.* [1].

$2\,\mathrm{mJ\,cm^{-2}}$ matches this observation well. Furthermore, it is noteworthy that this effective lifetime is the same before and after extended illumination. Thus, quenching of triplet excitons at photoproduct sites constitutes only a minor loss channel, especially in competition with TTA.

The creation of a radical by triplet quenching supports the above-mentioned hypothesis of chlorin being the photoproduct. For example, in zinc-metallated porphyrin and chlorin, the LUMO energy levels are nearly isoenergetic, whereas the HOMO levels are higher in chlorin than in porphyrin [115]. Presumably, this enables porphyrin-to-chlorin hole transfer. In fact, free-base chlorin has reportedly been used as a hole acceptor in combination with free-base porphyrin [116]. This behavior is likely similar in palladium-metallated porphyrin/chlorin and is in agreement with the observed radical generation.

The population dynamics of the radicals can be modeled by the following rate equation:

$$\frac{\mathrm{d}[R]}{\mathrm{d}t} = +k_{\mathrm{R}}[T] - k_{\mathrm{R,GS}}[R], \tag{5.1}$$

where $[T]$ and $[R]$ are the concentrations of triplets and radicals, respectively, k_R is the rate of radical generation by triplet quenching and $k_\mathrm{R,GS}$ is the rate at which photoproduct sites with a radical on them return to the ground state. This equation can be solved analytically:

$$[R](t) = k_\mathrm{R} e^{-k_\mathrm{R,GS} t} \int_0^t e^{-k_\mathrm{R,GS}\xi} [T](\xi)\,\mathrm{d}\xi\,. \tag{5.2}$$

The triplet concentration $[T](t)$ is proportional to the kinetic trace of the PIA as shown in Figure 5.8A. Hence, Equation 5.2 makes it possible to model the TAS kinetic at each wavelength as the (weighted) sum of $[T](t)$ and $[R](t)$. This model can then be fit to the experimental data, which results in an optimized value for the radical recombination rate $k_\mathrm{R,GS} = 12.5 \times 10^6\,\mathrm{s}^{-1}$, corresponding to a lifetime of 80 ns. However, the triplet-to-radical rate k_R, which acts as a mere scaling factor in Equation 5.2, cannot be fit properly. It is insufficiently constrained because the absorption cross section of the radical is unknown.

The modeled concentration profiles are shown in Figure 5.9A. Initially, only the triplet state is populated (after fast ISC during the instrument response), and no radicals are present. As the triplet excitons diffuse, some encounter a photoproduct site, are subsequently quenched and thus populate the radical state. The radical concentration increases until around 100 ns, followed by its decay.

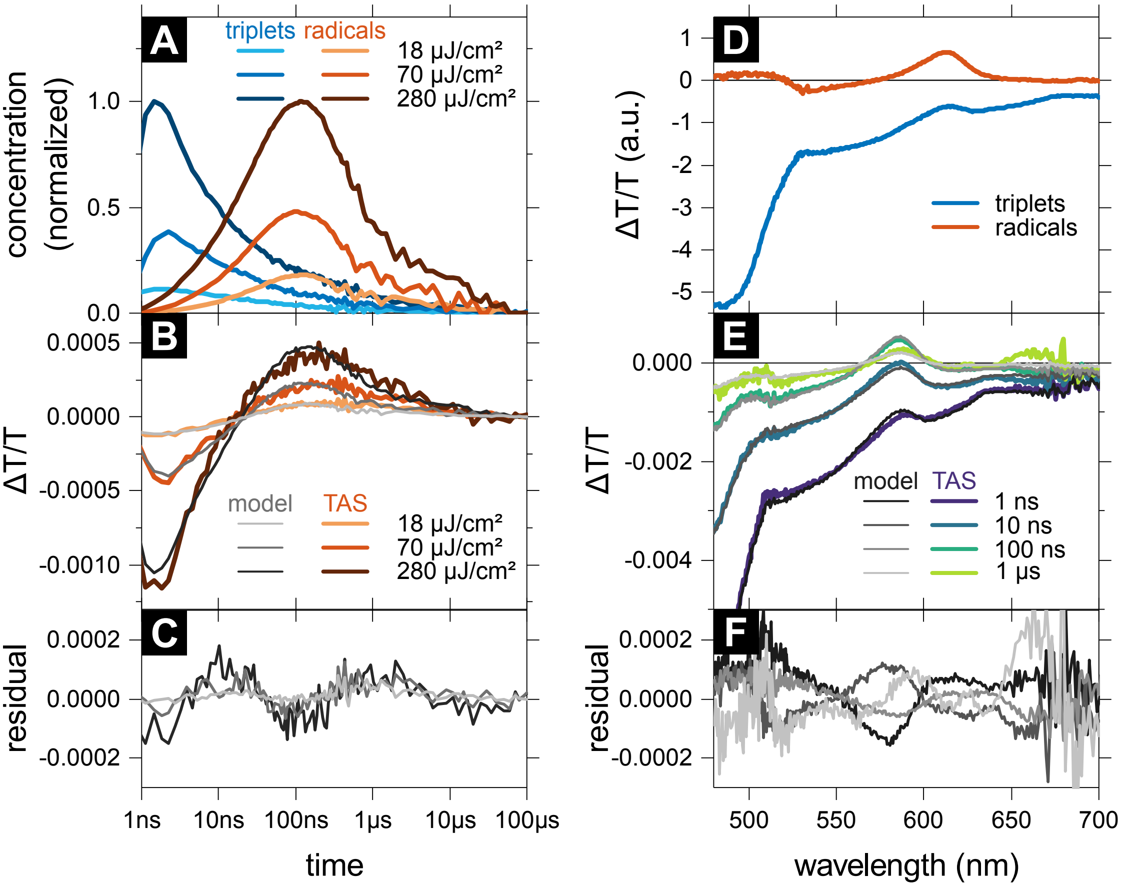

Figure 5.9: Model of the radical and triplet populations. **(A)** Time evolution of triplet and radical concentrations, normalized to their respective values at 280 µJ cm^{-2}. **(B)** Comparison of experimental and modeled TAS kinetics in the GSB wavelength region (605 nm to 620 nm). **(C)** residual values (difference between model and experimental data) from panel (B). **(D)** Single-component TAS spectra of triplets and radicals (arbitrary scale). **(E)** Comparison of experimental and modeled TAS spectra for different time delays at an excitation fluence of 280 µJ cm^{-2}. **(F)** residual values (difference between model and experimental data) from panel (E).

The optimized model fits the experimental kinetics well, as can be seen in Figure 5.9B. The residuals of this fit (Figure 5.9C) are small and do not show a systematic trend.

Besides comparing the kinetics, the data and model can also be compared in terms of their spectra. The two-dimensional TAS data matrices D_n for each of the three excitation fluences ($n \in \{1, 2, 3\}$) are $M \times N$ matrices, where M is the number of discrete time values and N the number of wavelength values. These matrices can be decomposed into their spectra S_n ($N \times R$) and the concentrations kinetics C_n ($M \times R$)

$$D_n = C_n S_n^{\mathrm{T}}, \tag{5.3}$$

where R is the rank of the matrix (here $R = 2$, see section 5.1). The concentration matrices C_n for each D_n are known from the model and fit of the TAS data (see Figure 5.9A). Thus, the spectra S_n can be calculated via Equation 5.3. As the shape of the spectra does not depend on the excitation fluence ($S_n = S$), the matrices D_n and C_n can be concatenated to form matrices D_{123} and C_{123}:

$$D_{123} = C_{123} S^{\mathrm{T}}. \tag{5.4}$$

However, the necessary inversion of this formula to find S does not have an exact solution. Instead, the MATLAB function `mrdivide()` is used to find an approximate least-square optimized solution.

The resulting single-component spectra for the triplets and radicals are shown in Figure 5.9D. The most prominent feature in the radical spectrum is the positive GSB around 610 nm, which was used so far to track this state. In this wavelength region, the triplet PIA is non-zero, which is consistent with the observation that the early TAS kinetic is triplet-dominated before the radical signal becomes relevant. Furthermore, the triplet spectrum is dominated by the negative PIA. It is strongest below 520 nm. Importantly, the radical's contribution to the spectrum is relatively small in this wavelength region, which makes it ideal for tracking solely the triplet population and validates the choice of this wavelength region as a proxy for $[T](t)$.

One way to compare the fitted matrix $C_n S^{\mathrm{T}}$ to the original D_n is by extracting spectra at different times, as depicted in Figure 5.9E. The spectra are in good agreement at all times. Their difference (Figure 5.9F) is small and does not show a systematic trend.

5.4 Summary

This chapter has established that extended illumination of a PdP SURMOF in vacuum leads to the formation of photoproduct sites in the SURMOF. Mobile triplet excitons that encounter such a defect during their 1D diffusion can dissociate and form a radical. All observations – spanning several experimental methods – support the conclusion that the photoproduct is PdC. However, no direct proof was possible.

Around 5 % of the porphyrin molecules in the SURMOF are converted into photoproduct sites after around $10^{27}\,\mathrm{cm}^{-3}$ absorbed photons. The conversion process is independent of photon energy or excitation power density. Instead, it appears to depend on the amount of absorbed photons. The phosphorescence decreases over illumination time due to triplet quenching with a fast initial exponential-like decay followed by a much slower power-law-like decay. Accordingly, the photochemical conversion slows down over time. Radical creation at photoproduct sites is a loss process for triplet excitons. However, at the observed excited state concentrations it is negligible compared to TTA.

6 Film Morphology and Exciton Transport

The efficient transport of long-lived triplet excitons and especially their large diffusion length make the PdP SURMOF an exciting material for light harvesting applications. Hence, the question arises whether micron-scale diffusion is practically realizable. A 1D diffusion length of $L_\mathrm{D} = 6.3\,\mu\mathrm{m}$ implies that each triplet exciton has an average displacement of 1000 porphyrin units during its lifetime. This should be the case in an ideal single-crystal SURMOF. However, the spray-coating technique produces a polycrystalline film (as illustrated in Figure 3.12C). Are the crystal grains of sufficient size to support micron-scale diffusion? If that is not the case: is transport across grain boundaries possible?

6.1 Direct Observation of Triplet Exciton Transport

Earlier reports on micron-scale exciton diffusion showed, that transport processes can be directly observed by luminescence microscopy [7, 12, 24]. Therefore, this method should prove useful in answering the above questions.

Acknowledgments and Contributions

The experiments in this section were conceived by the author, Ian A. Howard and Gerd Ulrich Nienhaus. The PdP linkers were designed and synthesized by Ganapathi Emandi and Mathias O. Senge. Nicolò Baroni and Michael Oldenburg prepared the PdP SURMOF samples with the guidance of Christof Wöll. The author encapsulated the samples. The luminescence microscopy experiments were performed by Rui Ma under the guidance of Gerd Ulrich Nienhaus. Data analysis and modeling was performed by the author with support by Ian A. Howard.

6.1.1 Data Collection and Preprocessing

As the microscopy setup (see Figure 3.11) does not allow for measurements under dynamic vacuum or inert atmosphere, the PdP SURMOF thin film sample used in this experiment is encapsulated under nitrogen atmosphere to prevent triplet quenching by atmospheric oxygen. Furthermore, the experiments are conducted at room temperature.

The sample is excited with a focused 405 nm CW beam. Images of the phosphorescence emission are recorded through a 698 nm bandpass filter (FWHM: 70 nm). Seven different excitation fluences (0, 0.3, 1.4, 8.2, 19.3, 41.3, and 69.3 $\mathrm{W\,cm^{-2}}$) are used. Each experiment is performed on a pristine region of the sample and repeated for 7 different durations of local photodegradation (5, 10, 15, 20, 30, 45, and 60 min of illumination at 1.2 $\mathrm{W\,cm^{-2}}$ using the same 405 nm CW laser with an increased beam size of $\approx 70\,\mu\mathrm{m}$) on the same position. Finally, the whole process is repeated at two additional regions on the sample. To make sure that no degradation occurs during image-taking, each measurement (for a given excitation fluence, degradation time and sample position) is repeated 10 times, using an integration time of 1 s. In total, $3 \times 8 \times 7 \times 10 = 1680$ phosphorescence images are taken; a graphical summary of the whole data collection process is shown in Figure 6.1. As no degradation is visible during each of the 10 consecutive exposures, these sets could be averaged to yield 168 images with an effective integration time of 10 s.

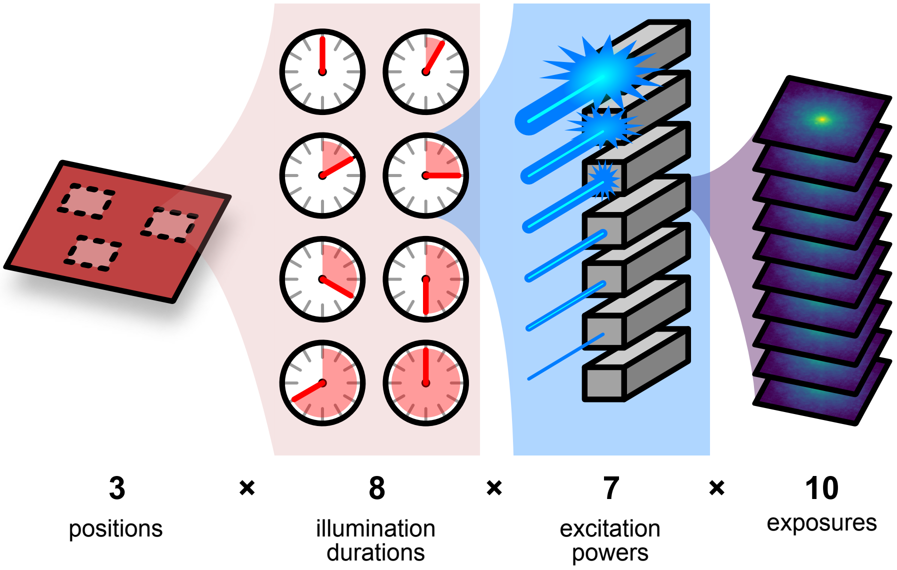

Figure 6.1: A graphical summary of all phosphorescence images that are taken in the luminescence microscopy experiment: 10 exposures of 1 s were made for each of the 7 excitation powers, which was repeated at 8 different illumination durations and at 3 positions on the encapsulated PdP SURMOF thin film sample.

As background correction, the images taken with the laser blocked (excitation density of $0\,\mathrm{W\,cm^{-2}}$) are subtracted from all other images in their respective set (sharing degradation time and position). Potential sources of background signal are light leakage and dark counts on the EMCCD camera. After this step, 144 phosphorescence images remain to be analyzed. Exemplary, such an image is shown in Figure 6.2C.

Furthermore, using a 405 nm bandpass filter with FWHM 10 nm, the scattering/reflection of the excitation light is also imaged. As before, at each of the 3 positions, 10 exposures with 1 s integration time are averaged and a background image with the laser off was subtracted, yielding one image per position (see Figure 6.2B). Additionally, the excitation light's reflection is also imaged on a flat mirror surface in the same fashion (see Figure 6.2A).

The intensity distributions on all phosphorescence and excitation images are radially symmetric and, therefore, radial averaging is performed. For this purpose, the pixel location with the maximum intensity is located, which is taken to be the center of the radially symmetric distribution. Then, the signal per area as a function of the radius is determined by iterating over all pixels, finding the intensity contained within all pixels at a given radial distance (rounded to integer values) divided by the number of pixels at that distance.

It is noteworthy that the datasets taken at different sample positions are consistent and almost identical. Therefore, in the following figures only data from one sample position will be shown for clarity's sake. However, all calculations are repeated with the respective data from each of the three sample positions. Because none of the calculations shows significant differences between the positions, the resulting parameters are averaged over these three values.

6.1.2 Qualitative Data Analysis

Comparing the shape of the phosphorescence images and profiles to those of the excitation light reveals that the former appear broadened (see Figure 6.2). A conceivable explanation for this observation is diffusion of triplet excitons through the film. However, the radial symmetry is at odds with the 1D nature of the diffusion process, as it should result in an anisotropic luminescence spot, extended along the fast axis of the crystal –

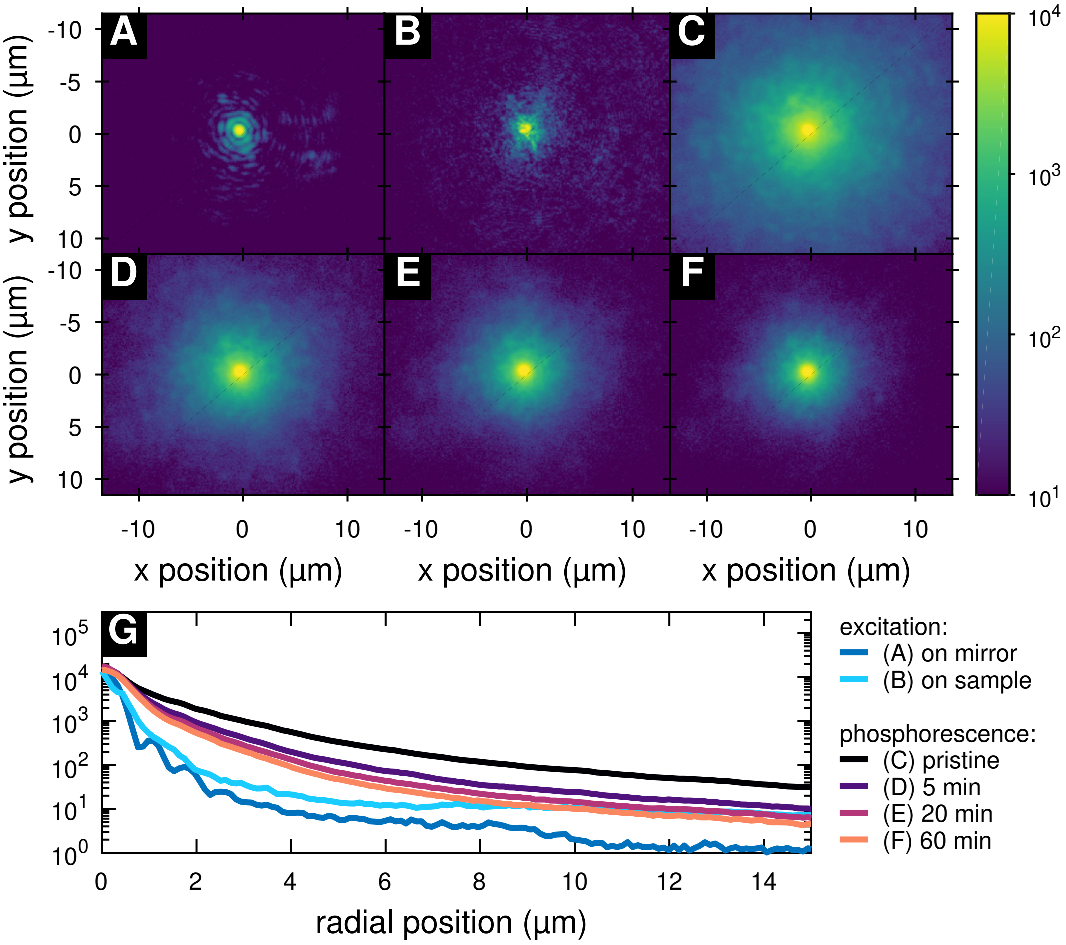

Figure 6.2: Micropscopy images of the excitation light's reflection on **(A)** a mirror and **(B)** the PdP SURMOF thin film sample. Furthermore, the phosphorescence images are shown at an excitation intensity of 41.3 W cm^{-2} in a **(C)** pristine sample and after **(D)** 5 min, **(E)** 20 min and **(F)** 60 min of illumination. **(G)** Radial profiles of the images (A)-(F).

at least for an ideal crystal. As this is not the case, there exist three possible explanations for the isotropic broadening of the PL:

H1 Anisotropic 1D diffusion in small crystal domains leads to effective isotropic diffusion, wherein the triplets cross domain boundaries,

H2 no micron-scale diffusion occurs, the excitation profile matches the measured profiles in Figure 6.2A and B, and the phosphorescence light is scattered inside the SURMOF isotropically,

H3 no micron-scale diffusion occurs and the broadening comes from scattered or waveguided (inside the glass substrate) excitation light, that is not properly represented in the excitation scatter profile in Figure 6.2B.

Based on the following detailed analysis, both hypothesis **H1** and **H2** will be eliminated, while **H3** is consistent with the data.

First, a discussion of the spatial distribution of TTA will help in ruling out **H2**. As before, the effects of TTA can be visualized by tracking the PL intensity for different excitation fluences. The microscopy data allow to analyze the scaling of PL intensity with excitation fluence at virtually every image pixel or – more practically – at each center-distance in the radially averaged dataset. The results are shown in Figure 6.3. At each radial position, a power-law fit ($f(x) \propto x^{\alpha}$, with α as free parameter) is performed on the PL intensity over excitation power density data. Two of these fits are shown exemplary in the inset of Figure 6.3. The power coefficient α is the value of interest: In case of linear scaling $\alpha = 1$, whereas in case of purely TTA-dominated exciton deactivation $\alpha = 0.5$. This TTA-dominated scaling is visible close to the center ($\approx 1\,\mu m$) of the phosphorescence spot. Going further away from the center, the power fit coefficient increases, and linear scaling is observed for center-distances of $> 10\,\mu m$. Even further out, α decreases again, as the PL signal becomes weak. Obviously, in regions without phosphorescence, there is no power-dependence of the signal, $\alpha \approx 0$. Very close to the center (radial distance around $1\,\mu m$), the power-dependence appears more linear, which is the result of exciton generation by the excitation laser.

An important conclusion can be drawn from this data: If the origin of the detected emission was scattered phosphorescence from the center region (hypothesis **H2**), the power-dependence and α would be independent of the distance from the center. This is obviously not the case. Thus, **H2** can be rejected. Instead, the phosphorescence emission is linked to an actual presence of triplets in the emissive region and proportional to their concentration.

Repeating the power-dependence analysis for the illuminated sample shows the effects of triplet quenching by photoproduct molecules, as discussed in chapter 5. The increasing concentration of such photoproduct sites in the PdP SURMOF opens an alternative deactivation pathway, which reduces the efficiency of TTA. Thus, the fit coefficient α in the center region increases with illumination time (see Figure 6.3). Because the overall signal is reduced in the illuminated samples, the decrease towards zero starts at smaller center-distances.

Another – more direct – way of looking at this illumination-induced change is by plotting PL profiles for all excitation intensities normalized to their values at $10\,\mu m$ (a compromise between being close to the linear regime and still having a good signal-to-noise ratio after extended illumination), as shown in Figure 6.4. In the pristine sample, the center region exhibits a different (sublinear) scaling behavior than the profile's tail region.

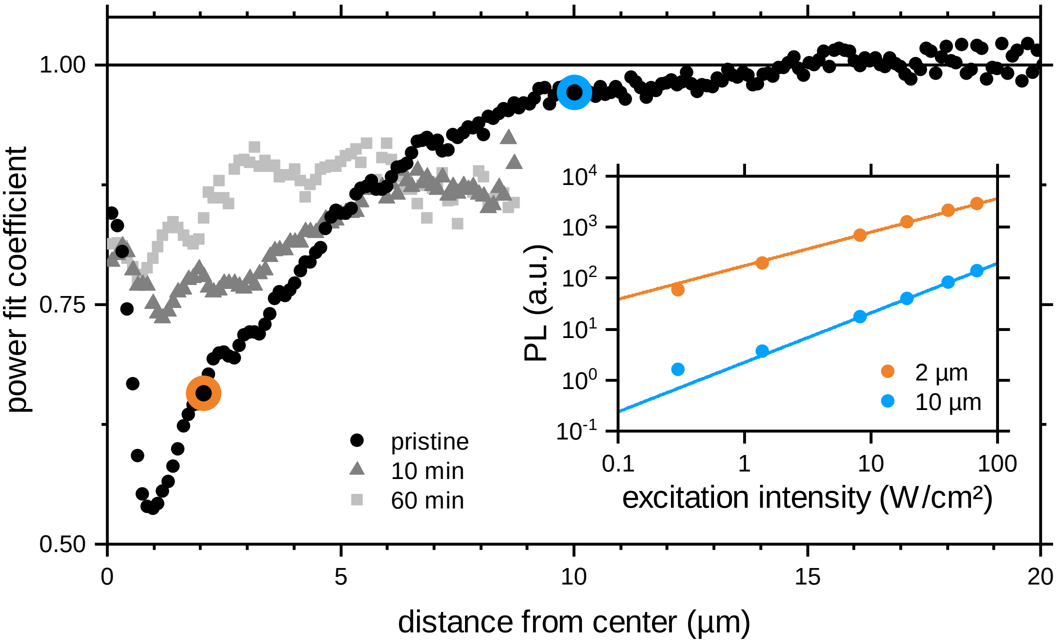

Figure 6.3: Power-dependence of the phosphorescence signal in the pristine PdP SURMOF thin film (black circles) and after 10 min (dark gray triangles) and 60 min (light gray squares) of illumination. Power-law fits are performed at each center-distance. For two data points (at $2\,\mu m$, highlighted orange, and at $10\,\mu m$, highlighted blue) the underlying PL data and the power fits are shown in the inset. Data for the illuminated sample are shown until $9\,\mu m$ only, as for larger center-distances the power fit becomes less reliable due to low PL signal intensity. Specifically, the fit values become noisy and tend towards zero instead of one.

At high excitation power density, the center intensities are – relative to the tail – smaller than at low power density. This is caused by TTA, which enables triplet exciton deactivation at high triplet concentrations. In contrast, this difference vanishes after extended illumination, because TTA now has to compete with radical pair generation.

6.1.3 Modeling the PL Profiles

For further analysis, it is instructive to introduce a model which describes the PL profiles. Introducing the rate of triplet generation G, we can express the triplet concentration dynamics as follow:

$$\frac{\partial T(\vec{x},t)}{\partial t} = G(\vec{x},t) - kT(\vec{x},t) - \gamma(\vec{x},t)T(\vec{x},t)^2 + \nabla\left(D(\vec{x},t)\nabla T(\vec{x},t)\right) . \tag{6.1}$$

Under steady-state conditions this expression equals zero. To simplify, γ can be assumed to be constant over time and space. TTA has been shown to be an important process in the thin film, however, it is not yet clear if exciton diffusion is observed in the microscopy experiment. Thus, as a first step, a simplified model is considered wherein no diffusion occurs. In combination with the radial symmetry of the PL data (distance from center: r) this leads to a simplified differential equation

$$\frac{\partial T(r)}{\partial t} = G(r) - kT(r) - \gamma T(r)^2 = 0 , \tag{6.2}$$

which can be solved analytically:

$$T_{1,2}(r) = -\frac{k}{2\gamma}\left(1 \pm \sqrt{1 + \frac{4G(r)\gamma}{k^2}}\right) . \tag{6.3}$$

The total generation rate G_{total} (absorbed photons per second) is calculated from the excitation power P, absorbance A, and the photon energy $E = hc/\lambda$:

$$G_{\text{total}} = \frac{P(1-10^{-A})}{E} . \tag{6.4}$$

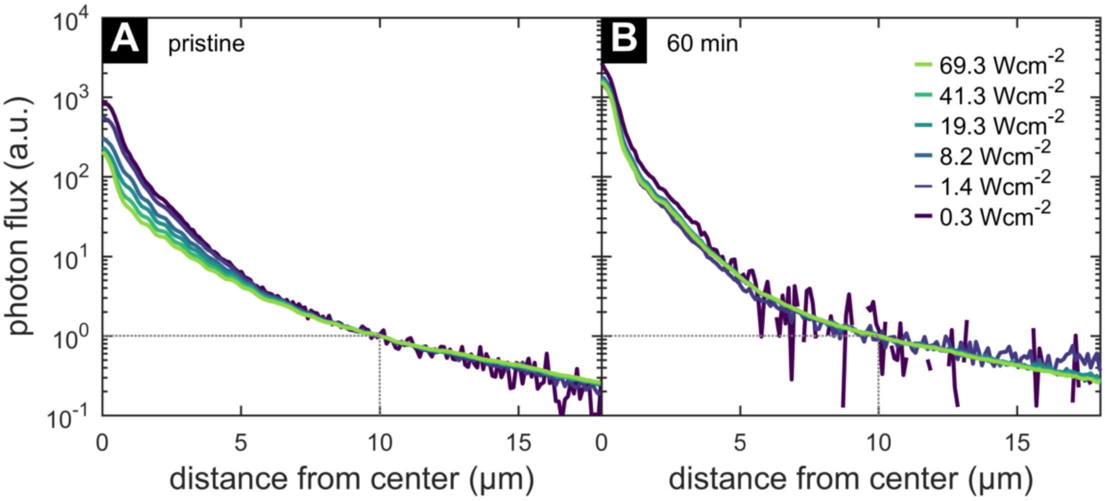

Figure 6.4: Phosphorescence profiles normalized at 10 µm for several excitation power densities of a **(A)** pristine and **(B)** degraded (60 min) encapsulated PdP SURMOF thin film sample.

The last piece of information that is required to calculate the radial triplet concentration profiles using Equation 6.3 is the shape of $G(r)$. It can be derived from the previous discussion of TTA and Figure 6.4. After 60 min of illumination, TTA does no longer play a significant role and can be neglected in Equation 6.2, yielding

$$G(r) = kT(r) \propto I(r)\,. \tag{6.5}$$

Therefore, the shape of $G(r)$ can be extracted from the radially averaged PL intensity profiles $I(r)$ as measured in arbitrary units on the EMCCD for the sample with the longest illumination time.[1]

Comparing the shape of $G(r)$ in Figure 6.2G (as the "60 min" curve) with the excitation profiles shows a clear deviation: Triplet excitons are created much farther away from the center than excitation light is detected. A possible explanation is that excitation light is scattered in the sample in such a way that it does not meet the detector but still excites the SURMOF. Similarly, excitation light might be waveguided either in the thin film or the substrate, thus exciting a wider area without being detected by the EMCCD. This would be consistent with hypothesis **H3**.

6.1.4 Calculation of the PL Profiles

To test the assumptions made in setting up the model above and to gain further insight into the PdP SURMOF photophysical characteristics, the calculated triplet concentrations from Equation 6.3 are fit to the experimental data. As motivated above, the generation rate $G(r)$ is derived by averaging the PL profiles of the most-degraded samples over all three sample positions. The profile for $8.2\,\mathrm{W\,cm^{-2}}$ excitation is used as it offers the best trade-off between low excitation power (for the least influence of TTA) and a good signal-to-noise-ratio.

Pristine Film

Optimizing the unknown steady-state TTA rate γ for the PL profiles from the pristine sample (while fixing the monomolecular rate $k = 1.37 \times 10^3\,\mathrm{s^{-1}}$ as established in section 4.1.3) yields $\gamma = 6 \times 10^{-17}\,\mathrm{cm^3\,s^{-1}}$. Using this parameter, the modeled curves match well to the experimental data for all excitation power densities, as can be seen in Figure 6.5A.

It is noteworthy that the inclusion of a diffusion term into the model can only reduce the overall fit quality because it would decrease the central PL intensity while increasing the signal at larger center-distances. In contrast, the TTA term is not only necessary for the model to correctly describe the data (especially the power dependence in Figure 6.3), it is also sufficient. Thus, the diffusion hypothesis **H1** can be rejected and – as **H2** was already dismissed above – hypothesis **H3** can be accepted.

Of course, triplet diffusion is a prerequisite for TTA and therefore certainly does take place in the SURMOF. However, the exciton's motion is restricted to its crystal domain. The absence of observable long-range diffusion thus reveals that the domain size is below the resolution limit of the microscopy setup, which is 240 nm for 700 nm phosphorescence light (see Equation 3.4).

---

[1] Some care has to be taken when converting $I(r)$ (arbitrary units) to $G(r)$ (in units of $\mathrm{s^{-1}\,cm^{-3}}$), as the data are discretized and radially averaged. One option is to divide the image's pixel values by their sum over the whole image before radial averaging, thus obtaining an area-normalized radial average $\tilde{I}(r)$ and

$$G(r) = \tilde{I}(r) \times G_{\mathrm{total}}\,. \tag{6.6}$$

Dividing this by the pixel area ($A_{\mathrm{pixel}} = 109\,\mathrm{nm} \times 109\,\mathrm{nm}$) and sample thickness d results in $G(r)$ having the correct units. When starting from the already radially averaged intensity profiles $I(r)$, the number of pixels that were averaged for each discrete position of r have to be taken into account:

$$\tilde{I}(r) = \frac{I(r)}{\sum_r \left(I(r) \times \sigma(r)\right)}\,, \tag{6.7}$$

where $\sigma(n)$ is the "[n]umber of integer Cartesian grid points covered by a ring around the origin with width 1 and outer radius n + 1/2." [117].

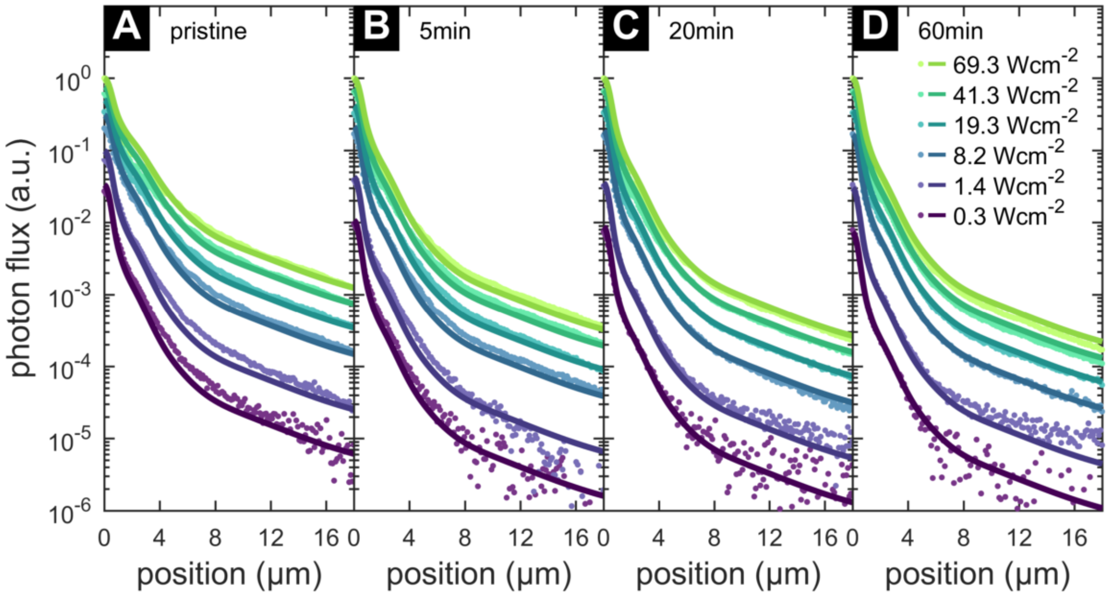

Figure 6.5: Experimental data (colored circles) and optimized models (solid lines, see text for details) of the radial phosphorescence profiles for different excitation power densities in **(A)** a pristine sample and for photodegraded samples after **(B)** 5 min, **(C)** 20 min and **(D)** 60 min of illumination. Profiles in each panel are normalized to the maximum value at the highest excitation power, maintaining their relative ratios while facilitating easy comparison between the illumination times.

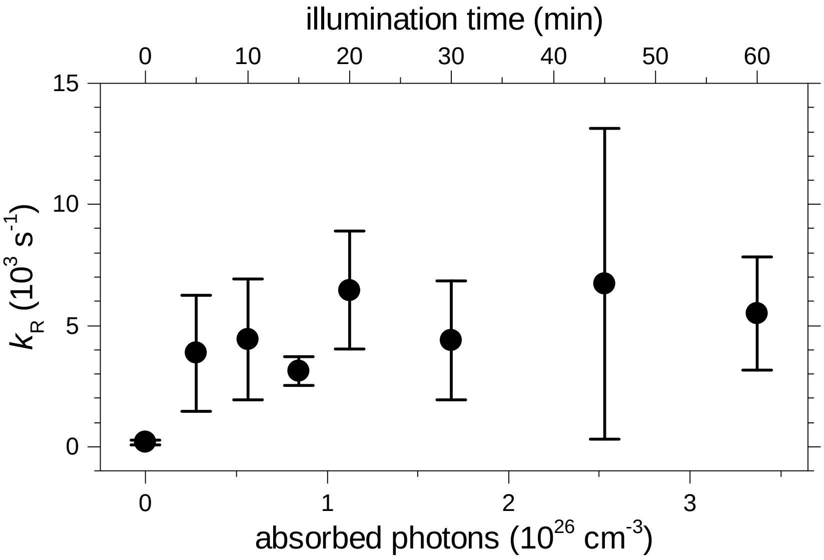

Figure 6.6: Radical generation rate k_R for different illumination durations. Values are determined for each of the three sample positions and averaged. The error bars represent the respective standard deviations. The absorbed photon density of the most-illuminated film corresponds to roughly 110 h of exposure to the sun at AM1.5 conditions.

Illuminated Film

In the measurements on illuminated samples, the process of radical generation needs to be taken into account. This can be done by substituting k in Equation 6.2 with a new rate $k = k_0 + k_R$, wherein k_R is the radical formation rate and k_0 the monomolecular decay rate. This rate depends on the concentration of photoproduct sites in the SURMOF. Thus, in a pristine film $k_R = 0$ and $k = k_0$. Thus, the analysis of the pristine sample, which considered only the monomolecular rate, remains valid.

The PL model fits are repeated for the illuminated SURMOF film with γ fixed to the value in the pristine sample and k_R as the free parameter. Again, the model describes the data well for all positions and excitation power densities (exemplarily shown in Figure 6.5B-D for three illumination times at one sample position). The extracted values (averaged over the three measurement positions) for k_R are shown in Figure 6.6 for each illumination time. The radical generation rate, being initially zero, increases over the first 20 min of illumination and subsequently levels out. After 60 min, which corresponds to a concentration of absorbed photons of $3.4 \times 10^{26}\,\mathrm{cm}^{-3}$, it reaches $k_R = (5 \pm 2) \times 10^3\,\mathrm{s}^{-1}$. For comparison: The monomolecular decay rate is $k_0 = 1.4 \times 10^3\,\mathrm{s}^{-1}$. Thus, k increases by roughly a factor 3.5 during the 1 h illumination. This is still small compared to the effective inverse lifetime of $2.7 \times 10^5\,\mathrm{s}^{-1}$ observed in the TAS experiment (see page 63). At excited state densities as in the TAS experiments, radical generation is a minor process, which is consistent with the previous analysis.

The effective diffusion length in an illuminated PdP SURMOF film can be calculated with Equation 2.9 using the effective lifetime $\tau = (k_0 + k_R)^{-1}$ and the previously established diffusion coefficient D. For the most-illuminated sample above, this computes to $L_D = 2.8\,\mu\mathrm{m}$, which is around 45 % of the value in the pristine material. This is well above the limit given by the crystal domain size and still highly competitive in comparison to other materials from literature [12, 31]. The light-induced formation of photoproduct defects in the SURMOF is therefore no obstacle in achieving micron-range exciton diffusion.

6.2 Steady-State PL

Another experiment that can be performed to investigate the photoresponse of a PdP SURMOF thin film is the measurement of the steady-state PL emission for different excitation fluences. This experiment independently corroborates the findings established in the previous section.

Acknowledgments and Contributions

The experiment in this section was conceived by the author and Ian A. Howard. The PdP linkers were designed and synthesized by Ganapathi Emandi and Mathias O. Senge. Nicolò Baroni and Michael Oldenburg prepared PdP SURMOF samples with the guidance of Christof Wöll. The steady-state PL experiment was performed by the author. Data analysis and modeling was performed by the author with support by Ian A. Howard.

Steady-State PL experiment

Measuring the steady-state PL for different excitation fluences is conceptually similar to the power-dependent measurements in the microscopy experiment, with the major difference being that the excitation power is swept over a wider range and with smaller steps and the emission is detected by a spectrometer. The latter allows for simultaneous detection of fluorescence (integrated from 600 nm to 640 nm) and phosphorescence (integrated from 700 nm to 850 nm).

The resulting data are shown in Figure 6.7. At low laser intensities, both fluorescence and phosphorescence scale linearly with excitation power. In contrast, the phosphorescence signal begins to deviate from a linear behavior and scales sublinearly for excitation power densities above $0.1\,\mathrm{W\,cm}^{-2}$. There, it scales with the square root of the power density. Absorption saturation of the sample can be excluded, because the fluorescence is measured simultaneously and still exhibits a linear dependence at high excitation intensities. The phosphorescence's linear scaling at low, and square-root scaling at high excitation intensities is a clear indication of TTA and therefore consistent with our earlier findings.

The data can be modeled in a similar way as the microscopy PL data (Equations 6.2-6.5). The phosphorescence signal I_{ph} can be expressed as

$$I_{\mathrm{ph}} = \alpha \left(-1 + \sqrt{1 + \frac{4[G]\gamma}{k^2}} \right), \tag{6.8}$$

where α is an unknown scaling factor and $[G]$ is the generation rate (here as the concentration of absorbed photons per second):

$$[G] = \frac{P(1-10^{-A})}{Ed}. \tag{6.9}$$

Fitting the model from Equation 6.8 to the data with α and γ as open parameters and k set to the monomolecular decay rate, an excellent match to the experimental data is obtained. This confirms once more the assertion that TTA plays a relevant role in the SURMOF's photoresponse. The extracted value of the steady-state TTA rate is $\gamma = 5.6 \times 10^{-18}\,\mathrm{cm^3\,s^{-1}}$. This is an order of magnitude below the value extracted in the luminescence microscopy experiment. The difference can be explained by the fact that here, the PL signal is integrated over the whole emission area. Because the excitation beam profile has long tails, regions with lower triplet concentration are included, which in turn leads to an underestimation of the TTA rate.

Furthermore, an interesting observation can be made by a back-of-the-envelope calculation based on the onset of TTA. The phosphorescence signal begins to deviate from linearity roughly between $0.01\,\mathrm{W\,cm^{-2}}$ and $0.1\,\mathrm{W\,cm^{-2}}$. Whereas the signal already scales sublinearly at the latter value, the former can be considered

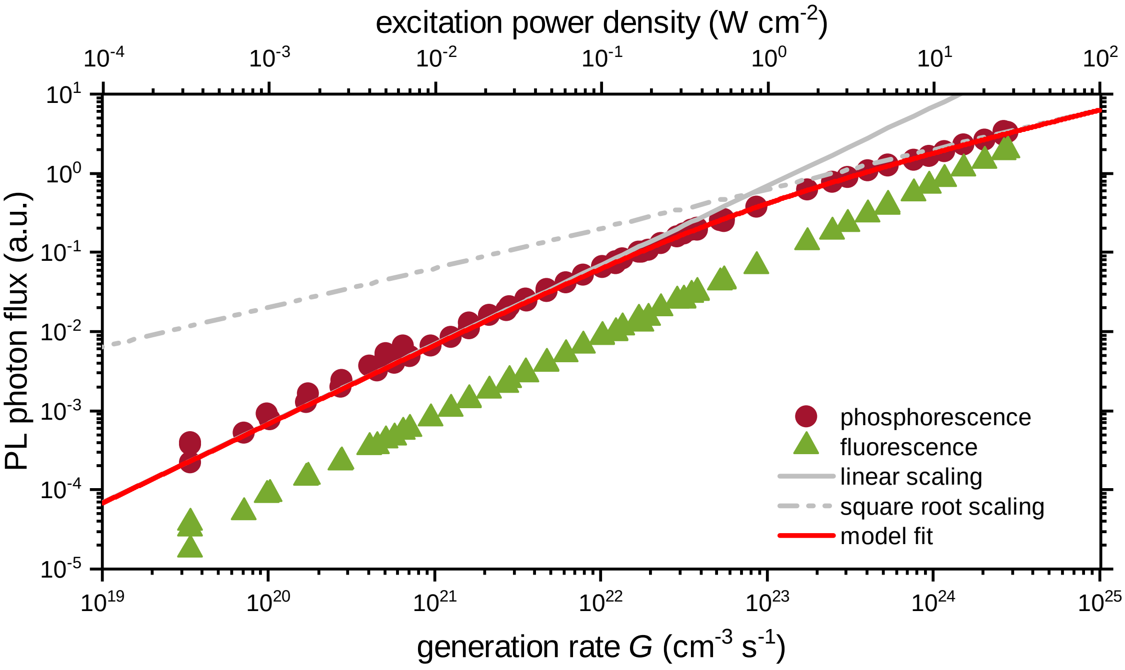

Figure 6.7: Dependence of the steady-state PL signal on the excitation power density and the triplet generation rate G in a PdP SURMOF thin film sample excited at 525 nm (CW). The scaling between phosphorescence and fluorescence is arbitrary and chosen to facilitate visual comparison. Linear and square root scaling are shown as a guide to the eye. Details of the model fit are described in the text.

as a "critical" power density, at which TTA is about to become possible. In this linear, TTA-free regime, the differential equation 6.2 solves to

$$[T] = [G]/k\,. \tag{6.10}$$

At an excitation power density of $0.01\,\mathrm{W\,cm^{-2}}$, this results in a critical triplet concentration of $[T]_{\mathrm{crit}} = 7.6 \times 10^{17}\,\mathrm{cm^{-3}}$. By comparing $[T]_{\mathrm{crit}}$ to the maximum concentration of PdP linker molecules in the SURMOF,[2] it can be estimated that around 0.3 % of all porphyrin molecules are in an excited triplet state. Furthermore, using the intra-sheet linker-to-linker distance of $b = 2.5\,\mathrm{nm}$, the average linear distance l_{crit} between two triplet excitons can be calculated as $l_{\mathrm{crit}} = (b^2[T]_{\mathrm{crit}})^{-1} = 210\,\mathrm{nm}$.

This distance is much smaller than the calculated triplet diffusion length in the SURMOF. Consistent with the luminescence microscopy experiment, the difference can be understood as the effect of small crystal domain sizes, which prevent triplet excitons from realizing their potential diffusion distances. For $l_{\mathrm{crit,D}} = L_{\mathrm{D}} = 6.3\,\mu\mathrm{m}$, the critical generation rate in this experiment at which TTA barely does not occur would be $[G]_{\mathrm{crit,D}} = 3 \times 10^{19}\,\mathrm{cm^{-3}\,s^{-1}}$. Because TTA starts only at higher concentrations, this means that a triplet exciton can only reach other triplets that are closer than $l_{\mathrm{crit}}/2 = 105\,\mathrm{nm}$. Therefore, the average crystal domain size in the PdP SURMOF can be estimated to lie roughly on the order of 100 nm, which agrees with the observation in the luminescence microscopy experiment that the domain dimensions are below the instrument's resolution of 240 nm.

6.3 Summary

This chapter established that no micron-scale exciton diffusion could be directly observed in the available PdP SURMOF thin films. This is caused by the limited size of crystalline domains in the polycrystalline SURMOF. Inside each domain, however, transport remains efficient, as demonstrated by TTA. These findings were corroborated by an independent steady-state PL experiment. Increasing the size of the crystal domains should enable direct observation of the predicted micron-scale diffusion length.

Comparative experiments with samples that have undergone photoproduct formation by extended illumination allowed the extraction of the radical generation rate k_{R} for different illumination times. Even in the most-illuminated sample, the theoretically achievable transport distance of $2.8\,\mu\mathrm{m}$ is still competitive.

---

[2] Based on the SURMOF structure and the linker-to-linker distances, the maximum porphyrin (and thus the maximum triplet) concentration is $[T]_{\mathrm{max}} = (0.6\,\mathrm{nm} \times 2.5\,\mathrm{nm} \times 2.5\,\mathrm{nm})^{-1} = 2.7 \times 10^{20}\,\mathrm{cm^{-3}}$.

7 Conclusion

This thesis presented a SURMOF comprised of PdP chromophores as linkers and investigated the excited states in this ordered material, with special focus on the motion of triplet excitons.

7.1 Summary and Discussion

Below, the three main results are briefly summarized and discussed. Additionally, a short outlook is presented in each section, outlining promising directions for future research.

Triplet Excitons Move Efficiently Along 1D Paths Between SURMOF Sheets

As the ISC yield in PdP is close to unity [43, 44], it could be shown that the only long-lived excited state in pristine PdP SURMOF thin films is the triplet exciton state. Due to the high degree of order in the SURMOF, these triplets move efficiently between MOF sheets that are spaced 0.6 nm apart. These investigated thin films are defect-poor and well connected, as less than 5 % of the triplet excitons were found to be immobilized on isolated chromophores.

Because triplets move exclusively by incoherent hopping between MOF sheets, triplet diffusion is restricted to one dimension and exciton motion inside the MOF sheets is unfavorable Lin *et al.* argued that the combination of Dexter transport with 1D hopping would be advantageous for energy collecting materials [14]. Notably, the investigated PdP SURMOF fulfills both criteria. Moreover, the Dexter electron exchange process was found by density functional theory (DFT) calculations to be enhanced by virtual intermediate charge-transfer states [2]. This results in a hopping rate on the order of $10^{11}\,\mathrm{s}^{-1}$.

To put this into perspective: The triplet transfer rate in conjugated polymers can be on the order of $10^{6}\,\mathrm{s}^{-1}$ [118], while rates similar to the PdP SURMOF are found in tetracyanoquinodimethane (TCNQ) salts ($10^{7}\,\mathrm{s}^{-1}$ to $10^{11}\,\mathrm{s}^{-1}$) [119], tetracene crystals ($10^{10}\,\mathrm{s}^{-1}$ to $10^{11}\,\mathrm{s}^{-1}$) [24], or triisopropylsilylethynyl acetylene (TIPS) pentacene thin films ($10^{11}\,\mathrm{s}^{-1}$) [120]. To compare with more similar materials, a MOF based on Ru-trisbipyridyl linkers (separated by $> 8\,\text{Å}$) was reported with a 1D triplet transfer rate on the order of $10^{8}\,\mathrm{s}^{-1}$ [14]. Furthermore, 3D triplet diffusion was reported in an anthracene-based MOF with $D = 7.7 \times 10^{-6}\,\mathrm{cm}^2\,\mathrm{s}^{-1}$ and a linker distance of 5.6 Å [31], which results in $k_{\mathrm{hop}} \approx 10^{9}\,\mathrm{s}^{-1}$ (using Equation 2.8).

In combination with the long monomolecular lifetime of 730 µs, the efficient hopping between porphyrin molecules leads to a triplet exciton diffusion length around 6 µm. This is on the same scale and slightly larger than the values reported for an anthracene-based MOF (1.6 µm) [31] or for 1D triplet diffusion in single-crystal rubrene (4 µm) [12].

These comparisons highlight that the PdP SURMOF is a highly competitive material system, outperforming other MOF systems while offering its own advantages, such as being easily deposited as thin film from solution.

Indeed, PdP SURMOFs have already been used in a liquid electrolyte photovoltaic cell with a power conversion efficiency of 0.45 % [67] and as sensitizer in a photon-upconversion SURMOF multilayer with an upconversion quantum yield of $\eta_{\mathrm{UC}} \lesssim 0.1\,\%$ [59]. In both cases, efficient triplet transport should be beneficial. However, both systems require the excitons to travel inside the SURMOF sheets instead of between them. As only the latter direction was found to exhibit highly efficient 1D transport, this could explain the low values for the respective figures of merit in both publications.

Hence, flipping the 1D transport direction in the SURMOF to be perpendicular to the substrate appears to be an obvious next step in the development of the material. This could be achieved by rotating the porphyrin sheets to be parallel to the substrate. A pillar-type SURMOF similar to the ZnP SURMOF presented by So *et al.* or Gordillo *et al.* (see Figure 7.1A) could make this possible [62, 65]. However, the efficient triplet transport in the PdP SURMOF presented in this thesis relies on close spacing of the sheets, with an inter-chromophore distance of 0.6 nm. The bipyridine pillar linkers chosen by Gordillo *et al.* are likely too long for this purpose and need to be substituted by a shorter molecule. Alternatively, Goswami *et al.* collapsed a similar SURMOF (comprised of both PdP and FbP linkers with bipyridine pillars) to achieve an inter-layer spacing of 0.7 nm [77]. However, the porphyrin center-to-center distance remained 1.4 nm, because adjacent layers are shifted laterally during the collapse (as shown in Figure 7.1B). Preventing these shifts while maintaining the small inter-layer distance in a PdP-based SURMOF would yield an ideal framework for efficient vertical 1D triplet transport that is well-suited to be integrated in typical device geometries.

Triplet-Quenching Photoproduct Sites are Introduced in the SURMOF During Prolonged Illumination

Extended illumination of a PdP SURMOF in vacuum leads to the formation of a stable photoproduct, which is likely PdC. Photoproduct concentration scales with the amount of absorbed photons. At these defect sites, triplets are quenched and dissociate into radicals. This leads to a reduction in the achievable diffusion length: By illumination equivalent to 110 h under sunlight, the calculated diffusion length is reduced from 6.3 µm to 2.8 µm.

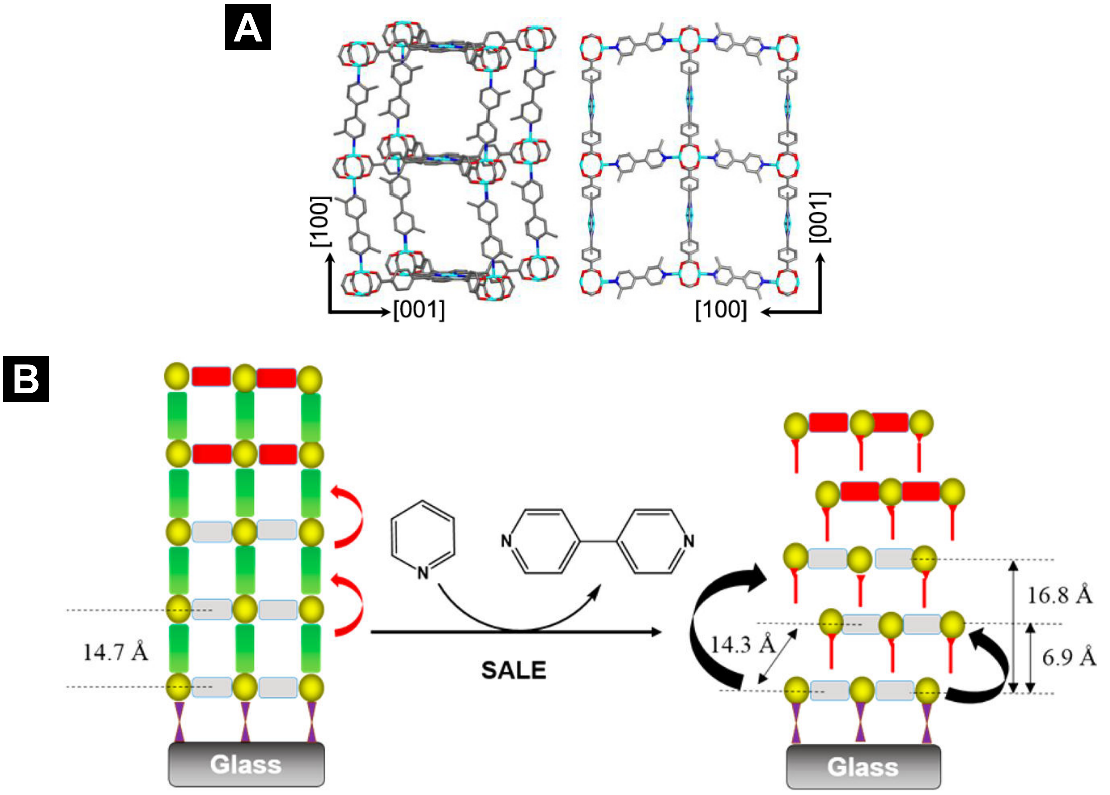

Figure 7.1: Porphyrin-based SURMOFs in which the porphyrin plane is parallel to the substrate. **(A)** Illustration of a pillar-type ZnP SURMOF. Reproduced with permission from Gordillo *et al.* [65]. **(B)** Illustration of a pillar-type ZnP/PdP (gray/red) SURMOF before and after collapse of the bipyridine pillars (green). Reproduced with permission from Goswami *et al.* [77].

Although this is still a good value for an organic material system, slowing down the degradation process or altogether preventing formation of triplet quenching sites has to be an important goal for future research. A good starting point could be to change the metalation of the porphyrin linker. For example, both platinum porphyrin (PtP) and ZnP are known to have a lower chlorin yield than PdP [110, 111]. Alternatively, the proposed reaction pathway from PdP to PdC requires a proton source such as residual water or solvent. By optimizing the deposition process to prevent accumulation of such residuals or efficiently removing them after film fabrication could thus block the photochemical pathway that leads to photoproduct formation. Yet another research direction would be the synthesis of an isoreticular SURMOF based on a different non-porphyrinic linker with a high ISC yield and a long triplet lifetime, but without a comparable photochemical degradation pathway.

Triplet Diffusion is Limited by the SURMOF's Crystal Domain Size

An attempt was made to assess whether multi-micron triplet diffusion can be observed directly by luminescence microscopy. This was found not to be the case. Although effective triplet transport does take place (established via the observation of efficient TTA), excitonic motion is restricted to individual SURMOF crystal domains, whose average size is below the resolution limit of the microscope (around 240 nm for the phosphorescence). As the efficient transport behavior is enabled by the close spacing between SURMOF sheets, a disruption of this ordered system at domain boundaries effectively stops the excitonic motion. The maximum distance a triplet exciton can travel is no longer determined by its lifetime and hopping rate, but by the size of the crystal domain. Based on data of a steady-state PL experiment, the grain SURMOF's crystal domain size was independently estimated to be on the order of 100 nm, which is consistent with the microscopy results.

This practical limitation prevents triplets in the PdP SURMOF to achieve their potential 1D diffusion length of 6.4 µm as extracted above. This needs to be overcome by increasing the size of crystalline domains in the SURMOF thin films. Notably, MOF single crystals with diameters on the millimeter scale have already been reported [121, 122], as shown in Figure 7.2. Whereas similar dimensions remain to be achieved in SURMOFs, promising reports exist. For example, Makiura & Konovalov could increase the domain size in a PdP single-sheet MOF from 140 nm to 220 nm by optimizing the injection process of the metal ions during the fabrication step [123]. Likewise, Müller *et al.* could drastically reduce the defect density in an HKUST-1 SURMOF by performing the rinsing step during deposition in an ultrasonic bath [124]. While not explicitly shown, this – or similar advancements of the fabrication process – could potentially be beneficial for creating larger SURMOF crystal domains.

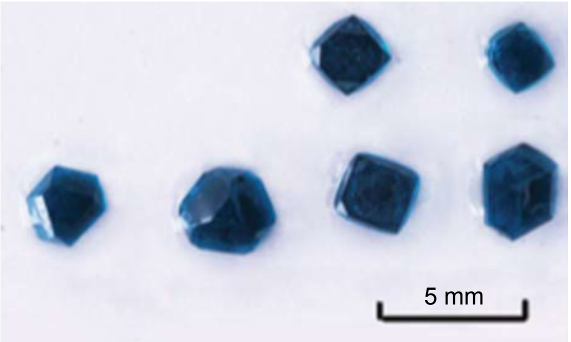

Figure 7.2: Digital photographs of millimeter-sized MOF single crystals. Adapted with permission from Li *et al.* [122].

7.2 Closing Remarks

Inspired by nature's approach for efficient transport of excited states (i. e. by using ordered porphyrin arrangements), the investigated PdP SURMOF thin films could be shown to exhibit beneficial exciton transport properties. Although some practical issues have to be addressed before the material is application-ready, the present thesis shows that SURMOFs can be a highly useful and versatile addition to the toolbox of device architects and engineers.

As the old saying goes: “If all you have is a hammer, everything looks like a nail”. However, with a well-equipped toolbox, the goals determine which tool to use, not the other way around. In this sense, to some creative problems that scientists and engineers will come up with, materials such as the PdP SURMOF presented in this thesis will surely be the solution. To use the words of Henry Ford [125]: “Progress happens when all the factors that make for it are ready, and then it is inevitable.”

Bibliography

1. Adams, M., Baroni, N., Oldenburg, M., Kraffert, F., Behrends, J., MacQueen, R. W., Haldar, R., Busko, D., Turshatov, A., Emandi, G., Senge, M. O., Wöll, C., Lips, K., Richards, B. S. & Howard, I. A. Reaction of porphyrin-based surface-anchored metal-organic frameworks caused by prolonged illumination. *Physical Chemistry Chemical Physics* **20,** 29142–29151. doi:`10.1039/C8CP05254A`. (2018).
2. Adams, M., Kozlowska, M., Baroni, N., Oldenburg, M., Ma, R., Busko, D., Turshatov, A., Emandi, G., Senge, M. O., Haldar, R., Wöll, C., Nienhaus, G. U., Richards, B. S. & Howard, I. A. Highly Efficient One-Dimensional Triplet Exciton Transport in a Palladium–Porphyrin-Based Surface-Anchored Metal–Organic Framework. *ACS Applied Materials & Interfaces* **11,** 15688–15697. doi:`10.1021/acsami.9b03079`. (2019).
3. Haldar, R., Mazel, A., Joseph, R., Adams, M., Howard, I. A., Richards, B. S., Tsotsalas, M., Redel, E., Diring, S., Odobel, F. & Wöll, C. Excitonically Coupled States in Crystalline Coordination Networks. *Chemistry - A European Journal* **23,** 14316–14322. doi:`10.1002/chem.201702968`. (2017).
4. Lami, V., Leibold, D., Fassl, P., Hofstetter, Y. J., Becker-Koch, D., Biegger, P., Paulus, F., Hopkinson, P. E., Adams, M., Bunz, U. H. F., Huettner, S., Howard, I., Bakulin, A. A. & Vaynzof, Y. N-Heteroacenes as a New Class of Non-Fullerene Electron Acceptors for Organic Bulk-Heterojunction Photovoltaic Devices. *Solar RRL* **1,** 1700053. doi:`10.1002/solr.201700053`. (2017).
5. Yost, S. R., Hontz, E., Yeganeh, S. & Van Voorhis, T. Triplet vs Singlet Energy Transfer in Organic Semiconductors: The Tortoise and the Hare. *The Journal of Physical Chemistry C* **116,** 17369–17377. doi:`10.1021/jp304433t`. (2012).
6. Mikhnenko, O. V., Blom, P. W. M. & Nguyen, T.-Q. Exciton diffusion in organic semiconductors. *Energy & Environmental Science* **8,** 1867–1888. doi:`10.1039/C5EE00925A`. (2015).
7. Wan, Y., Stradomska, A., Knoester, J. & Huang, L. Direct Imaging of Exciton Transport in Tubular Porphyrin Aggregates by Ultrafast Microscopy. *Journal of the American Chemical Society* **139,** 7287–7293. doi:`10.1021/jacs.7b01550`. (2017).
8. Caram, J. R., Doria, S., Eisele, D. M., Freyria, F. S., Sinclair, T. S., Rebentrost, P., Lloyd, S. & Bawendi, M. G. Room-Temperature Micron-Scale Exciton Migration in a Stabilized Emissive Molecular Aggregate. *Nano Letters* **16,** 6808–6815. doi:`10.1021/acs.nanolett.6b02529`. (2016).
9. Haedler, A. T., Kreger, K., Issac, A., Wittmann, B., Kivala, M., Hammer, N., Köhler, J., Schmidt, H.-W. & Hildner, R. Long-range energy transport in single supramolecular nanofibres at room temperature. *Nature* **523,** 196–199. doi:`10.1038/nature14570`. (2015).
10. Dubin, F., Melet, R., Barisien, T., Grousson, R., Legrand, L., Schott, M. & Voliotis, V. Macroscopic coherence of a single exciton state in an organic quantum wire. *Nature Physics* **2,** 32–35. doi:`10.1038/nphys196`. (2006).
11. Grieco, C., Doucette, G. S., Pensack, R. D., Payne, M. M., Rimshaw, A., Scholes, G. D., Anthony, J. E. & Asbury, J. B. Dynamic Exchange During Triplet Transport in Nanocrystalline TIPS-Pentacene Films. *Journal of the American Chemical Society* **138,** 16069–16080. doi:`10.1021/jacs.6b10010`. (2016).

12. Irkhin, P. & Biaggio, I. Direct Imaging of Anisotropic Exciton Diffusion and Triplet Diffusion Length in Rubrene Single Crystals. *Physical Review Letters* **107,** 017402. doi:`10.1103/PhysRevLett.107.017402`. (2011).
13. Hedley, G. J., Ruseckas, A. & Samuel, I. D. W. Light Harvesting for Organic Photovoltaics. *Chemical Reviews* **117,** 796–837. doi:`10.1021/acs.chemrev.6b00215`. (2017).
14. Lin, J., Hu, X., Zhang, P., Van Rynbach, A., Beratan, D. N., Kent, C. A., Mehl, B. P., Papanikolas, J. M., Meyer, T. J., Lin, W., Skourtis, S. S. & Constantinou, M. Triplet Excitation Energy Dynamics in Metal–Organic Frameworks. *The Journal of Physical Chemistry C* **117,** 22250–22259. doi:`10.1021/jp401515r`. (2013).
15. Green, M. A. & Keevers, M. J. Optical properties of intrinsic silicon at 300 K. *Progress in Photovoltaics: Research and Applications* **3,** 189–192. doi:`10.1002/pip.4670030303`. (2007).
16. Würfel, P., Trupke, T., Puzzer, T., Schäffer, E., Warta, W. & Glunz, S. W. Diffusion lengths of silicon solar cells from luminescence images. *Journal of Applied Physics* **101,** 123110. doi:`10.1063/1.2749201`. (2007).
17. Dong, Q., Fang, Y., Shao, Y., Mulligan, P., Qiu, J., Cao, L. & Huang, J. Electron-hole diffusion lengths > 175 µm in solution-grown CH3NH3PbI3 single crystals. *Science* **347,** 967–970. doi:`10.1126/science.aaa5760`. (2015).
18. Stranks, S. D., Eperon, G. E., Grancini, G., Menelaou, C., Alcocer, M. J. P., Leijtens, T., Herz, L. M., Petrozza, A. & Snaith, H. J. Electron-Hole Diffusion Lengths Exceeding 1 Micrometer in an Organometal Trihalide Perovskite Absorber. *Science* **342,** 341–344. doi:`10.1126/science.1243982`. (2013).
19. Schock, H.-W. & Noufi, R. CIGS-based solar cells for the next millennium. *Progress in Photovoltaics: Research and Applications* **8,** 151–160. doi:`10.1002/(SICI)1099-159X(200001/02)8:1<151::AID-PIP302>3.0.CO;2-Q`. (2000).
20. Brown, G., Faifer, V., Pudov, A., Anikeev, S., Bykov, E., Contreras, M. & Wu, J. Determination of the minority carrier diffusion length in compositionally graded Cu(In,Ga)Se2 solar cells using electron beam induced current. *Applied Physics Letters* **96,** 022104. doi:`10.1063/1.3291046`. (2010).
21. Tang, J. & Sargent, E. H. Infrared Colloidal Quantum Dots for Photovoltaics: Fundamentals and Recent Progress. *Advanced Materials* **23,** 12–29. doi:`10.1002/adma.201001491`. (2011).
22. Andernach, R., Utzat, H., Dimitrov, S. D., McCulloch, I., Heeney, M., Durrant, J. R. & Bronstein, H. Synthesis and Exciton Dynamics of Triplet Sensitized Conjugated Polymers. *Journal of the American Chemical Society* **137,** 10383–10390. doi:`10.1021/jacs.5b06223`. (2015).
23. Najafov, H., Lee, B., Zhou, Q., Feldman, L. C. & Podzorov, V. Observation of long-range exciton diffusion in highly ordered organic semiconductors. *Nature Materials* **9,** nmat2872. doi:`10.1038/nmat2872`. (2010).
24. Akselrod, G. M., Deotare, P. B., Thompson, N. J., Lee, J., Tisdale, W. A., Baldo, M. A., Menon, V. M. & Bulović, V. Visualization of exciton transport in ordered and disordered molecular solids. *Nature Communications* **5,** 3646. doi:`10.1038/ncomms4646`. (2014).
25. Liu, J. & Wöll, C. Surface-supported metal–organic framework thin films: fabrication methods, applications, and challenges. *Chemical Society Reviews* **46,** 5730–5770. doi:`10.1039/C7CS00315C`. (2017).
26. Köhler, A. & Bässler, H. *Electronic Processes in Organic Semiconductors: An Introduction* 1st ed. ISBN: 978-3-527-33292-2 (Wiley-VCH, Weinheim, 2015).
27. Gerson, F. & Huber, W. *Electron Spin Resonance Spectroscopy of Organic Radicals* doi:`10.1002/3527601627`. (Wiley-VCH, Weinheim, 2003).

28. Jelley, E. E. Spectral absorption and fluorescence of dyes in the molecular state. *Nature* **138,** 1009 (1936).

29. Scheibe, G. Über die Veränderlichkeit der Absorptionsspektren in Lösungen und die Nebenvalenzen als ihre Ursache. *Angewandte Chemie* **50,** 212–219 (1937).

30. Pope, M., Swenberg, C. E. & Pope, M. *Electronic processes in organic crystals and polymers* 2nd ed. *Monographs on the physics and chemistry of materials* **56.** ISBN: 978-0-19-512963-2 (Oxford University Press, New York, 1999).

31. Park, J., Xu, M., Li, F. & Zhou, H.-C. 3D Long-Range Triplet Migration in a Water-Stable Metal–Organic Framework for Upconversion-Based Ultralow-Power *in Vivo* Imaging. *Journal of the American Chemical Society* **140,** 5493–5499. doi:`10.1021/jacs.8b01613`. (2018).

32. Samiullah, M., Moghe, D., Scherf, U. & Guha, S. Diffusion length of triplet excitons in organic semiconductors. *Physical Review B* **82,** 205211. doi:`10.1103/PhysRevB.82.205211`. (2010).

33. Chandrasekhar, S. Stochastic Problems in Physics and Astronomy. *Reviews of Modern Physics* **15,** 1–89. doi:`10.1103/RevModPhys.15.1`. (1943).

34. Engel, E., Leo, K. & Hoffmann, M. Ultrafast relaxation and exciton–exciton annihilation in PTCDA thin films at high excitation densities. *Chemical Physics* **325,** 170–177. doi:`10.1016/j.chemphys.2005.09.004`. (2006).

35. Torney, D. C. & McConnell, H. M. Diffusion-limited reactions in one dimension. *The Journal of Physical Chemistry* **87,** 1941–1951. doi:`10.1021/j100234a023`. (1983).

36. Chemical Entities of Biological Interest. *bacteriochlorophyll a* 2015. URL: `https://www.ebi.ac.uk/chebi/searchId.do?chebiId=CHEBI:30033` (visited on Apr. 13, 2019).

37. Hastings, J., Owen, G., Dekker, A., Ennis, M., Kale, N., Muthukrishnan, V., Turner, S., Swainston, N., Mendes, P. & Steinbeck, C. ChEBI in 2016: Improved services and an expanding collection of metabolites. *Nucleic Acids Research* **44,** D1214–D1219. doi:`10.1093/nar/gkv1031`. (2016).

38. Gouterman, M. Spectra of porphyrins. *Journal of Molecular Spectroscopy* **6,** 138–163. doi:`10.1016/0022-2852(61)90236-3`. (1961).

39. Gouterman, M., Wagnière, G. H. & Snyder, L. C. Spectra of porphyrins: Part II. Four orbital model. *Journal of Molecular Spectroscopy* **11,** 108–127. doi:`10.1016/0022-2852(63)90011-0`. (1963).

40. Soret, J.-L. Analyse spectrale: Sur le spectre d'absorption du sang dans la partie violette et ultra-violette. *Compt. Rend* **97,** 1269–1270 (1883).

41. Otsuki, J. Supramolecular approach towards light-harvesting materials based on porphyrins and chlorophylls. *Journal of Materials Chemistry A* **6,** 6710–6753. doi:`10.1039/C7TA11274B`. (2018).

42. Wang, X.-F. & Tamiaki, H. Cyclic tetrapyrrole based molecules for dye-sensitized solar cells. *Energy & Environmental Science* **3,** 94–106. doi:`10.1039/B918464C`. (2010).

43. Kalyanasundaram, K. & Neumann-Spallart, M. Photophysical and redox properties of water-soluble porphyrins in aqueous media. *The Journal of Physical Chemistry* **86,** 5163–5169. doi:`10.1021/j100223a022`. (1982).

44. Solov'ev, K. N., Tsvirko, M. P. & Sapunov, V. V. Quantum yield for intersystem crossing in nonfluorescent metal porphyrins. *Journal of Applied Spectroscopy* **18,** 543–545. doi:`10.1007/BF00604521`. (1973).

45. Caprasecca, S., Corni, S. & Mennucci, B. Shaping excitons in light-harvesting proteins through nanoplasmonics. *Chemical Science* **9,** 6219–6227. doi:`10.1039/C8SC01162A`. (2018).

46. Fleming, G. R. & Grondelle, R. v. Femtosecond spectroscopy of photosynthetic light-harvesting systems. *Current Opinion in Structural Biology* **7,** 738–748. doi:`10.1016/S0959-440X(97)80086-3`. (1997).

47. Mirkovic, T., Ostroumov, E. E., Anna, J. M., van Grondelle, R., Govindjee & Scholes, G. D. Light Absorption and Energy Transfer in the Antenna Complexes of Photosynthetic Organisms. *Chemical Reviews* **117,** 249–293. doi:`10.1021/acs.chemrev.6b00002`. (2017).

48. Batten, S. R., Champness, N. R., Chen, X.-M., Garcia-Martinez, J., Kitagawa, S., Öhrström, L., O'Keeffe, M., Paik Suh, M. & Reedijk, J. Terminology of metal–organic frameworks and coordination polymers (IUPAC Recommendations 2013). *Pure and Applied Chemistry* **85,** 1715–1724. doi:`10.1351/PAC-REC-12-11-20`. (2013).

49. Li, H., Eddaoudi, M., O'Keeffe, M. & Yaghi, O. M. Design and synthesis of an exceptionally stable and highly porous metal-organic framework. *Nature* **402,** 276. doi:`10.1038/46248`. (1999).

50. Wang, H., Zhu, Q.-L., Zou, R. & Xu, Q. Metal-Organic Frameworks for Energy Applications. *Chem* **2,** 52–80. doi:`10.1016/j.chempr.2016.12.002`. (2017).

51. Furukawa, H., Cordova, K. E., O'Keeffe, M. & Yaghi, O. M. The Chemistry and Applications of Metal-Organic Frameworks. *Science* **341,** 1230444. doi:`10.1126/science.1230444`. (2013).

52. Eddaoudi, M., Kim, J., Rosi, N., Vodak, D., Wachter, J., O'Keeffe, M. & Yaghi, O. M. Systematic Design of Pore Size and Functionality in Isoreticular MOFs and Their Application in Methane Storage. *Science* **295,** 469–472. doi:`10.1126/science.1067208`. (2002).

53. Dolgopolova, E. A., Rice, A. M., Martin, C. R. & Shustova, N. B. Photochemistry and photophysics of MOFs: steps towards MOF-based sensing enhancements. *Chemical Society Reviews* **47,** 4710–4728. doi:`10.1039/C7CS00861A`. (2018).

54. Stassen, I., Burtch, N., Talin, A., Falcaro, P., Allendorf, M. & Ameloot, R. An updated roadmap for the integration of metal–organic frameworks with electronic devices and chemical sensors. *Chemical Society Reviews* **46,** 3185–3241. doi:`10.1039/C7CS00122C`. (2017).

55. Sun, L., Campbell, M. G. & Dincă, M. Electrically Conductive Porous Metal–Organic Frameworks. *Angewandte Chemie International Edition* **55,** 3566–3579. doi:`10.1002/anie.201506219`. (2016).

56. Pan, L., Ji, Z., Yi, X., Zhu, X., Chen, X., Shang, J., Liu, G. & Li, R.-W. Metal-Organic Framework Nanofilm for Mechanically Flexible Information Storage Applications. *Advanced Functional Materials* **25,** 2677–2685 (2015).

57. Wang, Z., Nminibapiel, D., Shrestha, P., Liu, J., Guo, W., Weidler, P. G., Baumgart, H., Wöll, C. & Redel, E. Resistive Switching Nanodevices Based on Metal–Organic Frameworks. *ChemNanoMat* **2,** 67–73. doi:`10.1002/cnma.201500143`. (2016).

58. Monguzzi, A., Tubino, R., Hoseinkhani, S., Campione, M. & Meinardi, F. Low power, non-coherent sensitized photon up-conversion: modelling and perspectives. *Physical Chemistry Chemical Physics* **14,** 4322–4332 (2012).

59. Oldenburg, M., Turshatov, A., Busko, D., Wollgarten, S., Adams, M., Baroni, N., Welle, A., Redel, E., Wöll, C., Richards, B. S. & Howard, I. A. Photon Upconversion at Crystalline Organic–Organic Heterojunctions. *Advanced Materials* **28,** 8477–8482. doi:`10.1002/adma.201601718`. (2016).

60. Oldenburg, M., Turshatov, A., Busko, D., Jakoby, M., Haldar, R., Chen, K., Emandi, G., Senge, M. O., Wöll, C., Hodgkiss, J. M., Richards, B. S. & Howard, I. A. Enhancing the photoluminescence of surface anchored metal–organic frameworks: mixed linkers and efficient acceptors. *Physical Chemistry Chemical Physics.* doi:`10.1039/C7CP08452H`. (2018).

61. Mahato, P., Yanai, N., Sindoro, M., Granick, S. & Kimizuka, N. Preorganized chromophores facilitate triplet energy migration, annihilation and upconverted singlet energy collection. *Journal of the American Chemical Society* **138,** 6541–6549 (2016).

62. So, M. C., Wiederrecht, G. P., Mondloch, J. E., Hupp, J. T. & Farha, O. K. Metal–organic framework materials for light-harvesting and energy transfer. *Chemical Communications* **51,** 3501–3510. doi:`10.1039/C4CC09596K`. (2015).

63. Lee, C. Y., Farha, O. K., Hong, B. J., Sarjeant, A. A., Nguyen, S. T. & Hupp, J. T. Light-Harvesting Metal–Organic Frameworks (MOFs): Efficient Strut-to-Strut Energy Transfer in Bodipy and Porphyrin-Based MOFs. *Journal of the American Chemical Society* **133,** 15858–15861. doi:`10.1021/ja206029a`. (2011).

64. Son, H.-J., Jin, S., Patwardhan, S., Wezenberg, S. J., Jeong, N. C., So, M., Wilmer, C. E., Sarjeant, A. A., Schatz, G. C., Snurr, R. Q., Farha, O. K., Wiederrecht, G. P. & Hupp, J. T. Light-Harvesting and Ultrafast Energy Migration in Porphyrin-Based Metal–Organic Frameworks. *Journal of the American Chemical Society* **135,** 862–869. doi:`10.1021/ja310596a`. (2013).

65. Gordillo, M. A., Panda, D. K. & Saha, S. Efficient MOF-Sensitized Solar Cells Featuring Solvothermally Grown [100]-Oriented Pillared Porphyrin Framework-11 Films on ZnO/FTO Surfaces. *ACS Applied Materials & Interfaces* **11,** 3196–3206. doi:`10.1021/acsami.8b17807`. (2019).

66. Liu, J., Zhou, W., Liu, J., Fujimori, Y., Higashino, T., Imahori, H., Jiang, X., Zhao, J., Sakurai, T., Hattori, Y., Matsuda, W., Seki, S., Garlapati, S. K., Dasgupta, S., Redel, E., Sun, L. & Wöll, C. A new class of epitaxial porphyrin metal–organic framework thin films with extremely high photocarrier generation efficiency: promising materials for all-solid-state solar cells. *Journal of Materials Chemistry A* **4,** 12739–12747. doi:`10.1039/C6TA04898F`. (2016).

67. Liu, J., Zhou, W., Liu, J., Howard, I., Kilibarda, G., Schlabach, S., Coupry, D., Addicoat, M., Yoneda, S., Tsutsui, Y., Sakurai, T., Seki, S., Wang, Z., Lindemann, P., Redel, E., Heine, T. & Wöll, C. Photoinduced Charge-Carrier Generation in Epitaxial MOF Thin Films: High Efficiency as a Result of an Indirect Electronic Band Gap? *Angewandte Chemie International Edition* **54,** 7441–7445. doi:`10.1002/anie.201501862`. (2015).

68. Yoon, S. M., Park, J. H. & Grzybowski, B. A. Large-Area, Freestanding MOF Films of Planar, Curvilinear, or Micropatterned Topographies. *Angewandte Chemie International Edition* **56,** 127–132. doi:`10.1002/anie.201607927`. (2017).

69. Hermes, S., Schröder, F., Chelmowski, R., Wöll, C. & Fischer, R. A. Selective Nucleation and Growth of Metal-Organic Open Framework Thin Films on Patterned COOH/CF3-Terminated Self-Assembled Monolayers on Au(111). *Journal of the American Chemical Society* **127,** 13744–13745. doi:`10.1021/ja053523l`. (2005).

70. Zhuang, J.-L., Terfort, A. & Wöll, C. Formation of oriented and patterned films of metal–organic frameworks by liquid phase epitaxy: A review. *Coordination Chemistry Reviews. Chemistry and Applications of Metal Organic Frameworks* **307,** 391–424. doi:`10.1016/j.ccr.2015.09.013`. (2016).

71. Oldenburg, M. *Photon upconversion heterostructures made from surface-anchored metal-organic frameworks* PhD thesis (Karlsruhe Institute of Technology, Karlsruhe, Germany, 2019). doi:`10.5445/KSP/1000087374`.

72. Heinke, L., Gliemann, H., Tremouilhac, P. & Wöll, C. in *The Chemistry of Metal-Organic Frameworks: Synthesis, Characterization, and Applications* (ed Kaskel, S.) 523–550 (Wiley-VCH Verlag GmbH & Co. KGaA, 2016). ISBN: 978-3-527-69307-8.

73. Summerfield, A., Cebula, I., Schröder, M. & Beton, P. H. Nucleation and Early Stages of Layer-by-Layer Growth of Metal Organic Frameworks on Surfaces. *The Journal of Physical Chemistry C* **119,** 23544–23551. doi:`10.1021/acs.jpcc.5b07133`. (2015).

74. Arslan, H. K., Shekhah, O., Wohlgemuth, J., Franzreb, M., Fischer, R. A. & Wöll, C. High-Throughput Fabrication of Uniform and Homogenous MOF Coatings. *Advanced Functional Materials* **21,** 4228–4231. doi:`10.1002/adfm.201101592`. (2011).

75. Delen, G., Ristanović, Z., Mandemaker, L. D. B. & Weckhuysen, B. M. Mechanistic Insights into Growth of Surface-Mounted Metal-Organic Framework Films Resolved by Infrared (Nano-) Spectroscopy. *Chemistry – A European Journal* **24,** 187–195. doi:`10.1002/chem.201704190`. (2018).

76. Farha, O. K., Shultz, A. M., Sarjeant, A. A., Nguyen, S. T. & Hupp, J. T. Active-Site-Accessible, Porphyrinic Metal-Organic Framework Materials. *Journal of the American Chemical Society* **133,** 5652–5655. doi:`10.1021/ja111042f`. (2011).

77. Goswami, S., Ma, L., Martinson, A. B. F., Wasielewski, M. R., Farha, O. K. & Hupp, J. T. Toward Metal–Organic Framework-Based Solar Cells: Enhancing Directional Exciton Transport by Collapsing Three-Dimensional Film Structures. *ACS Applied Materials & Interfaces* **8,** 30863–30870. doi:`10.1021/acsami.6b08552`. (2016).

78. Deria, P., Yu, J., Balaraman, R. P., Mashni, J. & White, S. N. Topology-dependent emissive properties of zirconium-based porphyrin MOFs. *Chemical Communications* **52,** 13031–13034. doi:`10.1039/C6CC07343C`. (2016).

79. Zewail, A. H. Femtochemistry: Atomic-Scale Dynamics of the Chemical Bond. *The Journal of Physical Chemistry A* **104,** 5660–5694. doi:`10.1021/jp001460h`. (2000).

80. Nobel Media AB. *The Nobel Prize in Chemistry 1999 Press Release* 1999. URL: `https://www.nobelprize.org/prizes/chemistry/1999/press-release/` (visited on Apr. 19, 2019).

81. *Springer Handbook of Lasers and Optics* 2nd ed. (ed Träger, F.) ISBN: 978-3-642-19408-5. (Springer-Verlag, Berlin Heidelberg, 2012).

82. *Lasers in Chemistry* (ed Lackner, M.) ISBN: 978-3-527-31997-8 (Wiley-VCH, Weinheim, 2008).

83. Strickland, D. & Mourou, G. Compression of amplified chirped optical pulses. *Optics Communications* **55,** 447–449. doi:`10.1016/0030-4018(85)90151-8`. (1985).

84. Nobel Media AB. *The Nobel Prize in Physics 2018 Press Release* URL: `https://www.nobelprize.org/prizes/physics/2018/press-release` (visited on Apr. 22, 2019).

85. *Empower – Intracavity Doubled, Diode-Pumped Nd:YLF Laser Systems – User's Manual* Rev. B. Spectra-Physics (2005).

86. *Tsunami – Mode-locked Ti:sapphire Laser – User's Manual* Spectra-Physics ().

87. *Spitfire – Ti:Sapphire Regenerative Amplifier Systems – User's Manual* Rev. D. Spectra-Physics (2002).

88. *LD-515-10MG* rev.1.0. Roithner LaserTechnik GmbH (2016). URL: `http://www.roithner-laser.com/datasheets/ld_div/ld-515-10mg.pdf` (visited on Jan. 8, 2019).

89. *Laser Diode Current and Temperature Controller ITC4000 Series Operation Manual* version 3.9. Thorlabs (2018). URL: `https://www.thorlabs.com/drawings/a79d958735ed1874-066096A0-FA46-256A-01D734C719932CB1/ITC4001-Manual.pdf` (visited on Jan. 9, 2019).

90. *DL-7146-101S* rev.2.0. Roithner LaserTechnik GmbH (2017). URL: `http://www.roithner-laser.com/datasheets/ld_div/dl-7146-101s.pdf` (visited on May 16, 2019).

91. *Stradus 405-250 Datasheet* version P/N 10860 B2. Vortran Laser Technology, Inc. (2016). URL: `http://www.vortranlaser.com/images/stories/printables/Stradus%20405-250%20Datasheet%2010860.pdf` (visited on Feb. 12, 2019).

92. Czerny, M. & Turner, A. F. Über den Astigmatismus bei Spiegelspektrometern. *Zeitschrift für Physik* **61,** 792–797. doi:`10.1007/bf01340206` (1930).

93. *Photomultiplier Tubes – Basics and Applications* Edition 3a. Hamamatsu Photonics K. K. (2007). URL: `https://www.hamamatsu.com/resources/pdf/etd/PMT_handbook_v3aE.pdf` (visited on Jan. 10, 2019).

94. *Photomultiplier Tubes R928, R928P, R955* Hamamatsu Photonics K. K. (2016). URL: `https://www.hamamatsu.com/resources/pdf/etd/R928_R928P_R955_R955P_TPMS1091E.pdf` (visited on Jan. 10, 2019).

95. *TimeHarp 260 TCSPC and MCS board with PCIe interface* PicoQuant GmbH (2018). URL: `https://www.picoquant.com/images/uploads/downloads/timeharp260.pdf` (visited on Jan. 10, 2019).

96. *Guide to Streak Cameras* Hamamatsu Photonics K. K. (2008). URL: `https://www.hamamatsu.com/resources/pdf/sys/SHSS0006E_STREAK.pdf` (visited on May 14, 2019).

97. *High-Performance Lambda Spectrometers Hardware Guide* Release A. Perkin Elmer, Inc. (2007).

98. Haldar, R., Jakoby, M., Mazel, A., Zhang, Q., Welle, A., Mohamed, T., Krolla, P., Wenzel, W., Diring, S., Odobel, F., Richards, B. S., Howard, I. A. & Wöll, C. Anisotropic energy transfer in crystalline chromophore assemblies. *Nature Communications* **9,** 4332. doi:`10.1038/s41467-018-06829-3`. (2018).

99. Kiseleva, N., Filatov, M. A., Oldenburg, M., Busko, D., Jakoby, M., Howard, I. A., Richards, B. S., Senge, M. O., Borisov, S. M. & Turshatov, A. The Janus-faced chromophore: a donor–acceptor dyad with dual performance in photon up-conversion. *Chemical Communications* **54,** 1607–1610. doi:`10.1039/C7CC08930A`. (2018).

100. Liu, J., Lukose, B., Shekhah, O., Arslan, H. K., Weidler, P., Gliemann, H., Bräse, S., Grosjean, S., Godt, A., Feng, X., Müllen, K., Magdau, I.-B., Heine, T. & Wöll, C. A novel series of isoreticular metal organic frameworks: realizing metastable structures by liquid phase epitaxy. *Scientific Reports* **2,** 921. doi:`10.1038/srep00921`. (2012).

101. Hynek, J., Rathouský, J., Demel, J. & Lang, K. Design of porphyrin-based conjugated microporous polymers with enhanced singlet oxygen productivity. *RSC Advances* **6,** 44279–44287. doi:`10.1039/C6RA04066G`. (2016).

102. Verma, S. & Ghosh, H. N. Exciton Energy and Charge Transfer in Porphyrin Aggregate/Semiconductor (TiO2) Composites. *The Journal of Physical Chemistry Letters* **3,** 1877–1884. doi:`10.1021/jz300639q`. (2012).

103. Verma, S., Ghosh, A., Das, A. & Ghosh, H. N. Ultrafast Exciton Dynamics of J- and H-Aggregates of the Porphyrin-Catechol in Aqueous Solution. *The Journal of Physical Chemistry B* **114,** 8327–8334. doi:`10.1021/jp101643c`. (2010).

104. Arnaut, L. G. in *Advances in Inorganic Chemistry* (eds van Eldik, R. & Stochel, G.) 187–233 (Academic Press, 2011). doi:`10.1016/B978-0-12-385904-4.00006-8`.

105. Harriman, A. Luminescence of porphyrins and metalloporphyrins. Part 3.—Heavy-atom effects. *Journal of the Chemical Society, Faraday Transactions 2: Molecular and Chemical Physics* **77,** 1281–1291. doi:`10.1039/F29817701281`. (1981).

106. Önal, E., Saß, S., Hurpin, J., Ertekin, K., Topal, S. Z., Kumke, M. U. & Hirel, C. Lifetime-Based Oxygen Sensing Properties of palladium(II) and platinum(II) meso-tetrakis(4-phenylethynyl)phenylporphyrin. *Journal of Fluorescence* **27,** 861–868. doi:`10.1007/s10895-016-2022-x`. (2017).

107. D. Allendorf, M., A. Bauer, C., K. Bhakta, R. & T. Houk, R. J. Luminescent metal–organic frameworks. *Chemical Society Reviews* **38,** 1330–1352. doi:`10.1039/B802352M`. (2009).

108. Barbosa Neto, N. M., Correa, D. S., De Boni, L., Parra, G. G., Misoguti, L., Mendonça, C. R., Borissevitch, I. E., Zílio, S. C. & Gonçalves, P. J. Excited states absorption spectra of porphyrins – Solvent effects. *Chemical Physics Letters* **587,** 118–123. doi:`10.1016/j.cplett.2013.09.066` (2013).

109. U.S. Department of Energy (DOE)/NREL/ALLIANCE. *ASTM G173-03 Reference Spectra Derived from SMARTS v. 2.9.2* 2003. URL: `https://www.nrel.gov/grid/solar-resource/spectra-am1.5.html` (visited on Oct. 30, 2018).

110. Kalyanasundaram, K. Mechanism of photoreduction of water-soluble palladium and zinc porphyrins. *Journal of Photochemistry and Photobiology A: Chemistry* **42,** 87–109. doi:`10.1016/1010-6030(88)80051-0`. (1988).

111. Vasil'ev, V. V., Blinova, I. A., Golovina, I. V. & Borisov, S. M. Photophysical and photochemical properties of the water-soluble porphyrin complexes of metals of the platinum group. *Journal of Applied Spectroscopy* **66,** 583–587. doi:`10.1007/BF02675390`. (1999).

112. Schneider, J., Vuong, K. Q., Calladine, J. A., Sun, X.-Z., Whitwood, A. C., George, M. W. & Perutz, R. N. Photochemistry and Photophysics of a Pd(II) Metalloporphyrin: Re(I) Tricarbonyl Bipyridine Molecular Dyad and its Activity Toward the Photoreduction of CO $_2$ to CO. *Inorganic Chemistry* **50,** 11877–11889. doi:`10.1021/ic200243y`. (2011).

113. Arslan, H. K., Shekhah, O., Wieland, D. F., Paulus, M., Sternemann, C., Schroer, M. A., Tiemeyer, S., Tolan, M., Fischer, R. A. & Wöll, C. Intercalation in Layered Metal–Organic Frameworks: Reversible Inclusion of an Extended π-System. *Journal of the American Chemical Society* **133,** 8158–8161. doi:`10.1021/ja2037996`. (2011).

114. Patiny, L. & Borel, A. ChemCalc: A Building Block for Tomorrow's Chemical Infrastructure. *Journal of Chemical Information and Modeling* **53,** 1223–1228. doi:`10.1021/ci300563h`. (2013).

115. Chang, C. K., Hanson, L. K., Richardson, P. F., Young, R. & Fajer, J. Cation radicals of ferrous and free base isobacteriochlorins: Models for siroheme and sirohydrochlorin. *Proceedings of the National Academy of Sciences* **78,** 2652–2656. doi:`10.1073/pnas.78.5.2652`. (1981).

116. Hu, G., Suk Kang, H., Kumar Mandal, A., Roy, A., Kirmaier, C., F. Bocian, D., Holten, D. & S. Lindsey, J. Synthesis of arrays containing porphyrin, chlorin, and perylene-imide constituents for panchromatic light-harvesting and charge separation. *RSC Advances* **8,** 23854–23874. doi:`10.1039/C8RA04052D`. (2018).

117. Clark Kimberling, R. S. *A036705* The On-Line Encyclopedia of Integer Sequences. URL: `https://oeis.org/A036705` (visited on Feb. 15, 2019).

118. Fishchuk, I. I., Kadashchuk, A., Sudha Devi, L., Heremans, P., Bässler, H. & Köhler, A. Triplet energy transfer in conjugated polymers. II. A polaron theory description addressing the influence of disorder. *Physical Review B* **78,** 045211. doi:`10.1103/PhysRevB.78.045211`. (2008).

119. Hibma, T. & Kommandeur, J. Dynamics of triplet excitons in the simple tetracyanoquinodimethane (TCNQ) salts of rubidium, potassium, and tri-methyl-benzimidazol. *Physical Review B* **12,** 2608–2618. doi:`10.1103/PhysRevB.12.2608`. (1975).

120. Lee, T. S., Lin, Y. L., Kim, H., Pensack, R. D., Rand, B. P. & Scholes, G. D. Triplet Energy Transfer Governs the Dissociation of the Correlated Triplet Pair in Exothermic Singlet Fission. *The Journal of Physical Chemistry Letters* **9,** 4087–4095. doi:`10.1021/acs.jpclett.8b01834`. (2018).

121. Han, S., Wei, Y., Valente, C., Lagzi, I., Gassensmith, J. J., Coskun, A., Stoddart, J. F. & Grzybowski, B. A. Chromatography in a Single Metal-Organic Framework (MOF) Crystal. *Journal of the American Chemical Society* **132,** 16358–16361. doi:`10.1021/ja1074322`. (2010).

122. Li, L., Sun, F., Jia, J., Borjigin, T. & Zhu, G. Growth of large single MOF crystals and effective separation of organic dyes. *CrystEngComm* **15,** 4094–4098. doi:`10.1039/C3CE40137E`. (2013).

123. Makiura, R. & Konovalov, O. Interfacial growth of large-area single-layer metal-organic framework nanosheets. *Scientific Reports* **3,** 2506. doi:`10.1038/srep02506`. (2013).

124. Müller, K., Fink, K., Schöttner, L., Koenig, M., Heinke, L. & Wöll, C. Defects as Color Centers: The Apparent Color of Metal-Organic Frameworks Containing Cu 2+-Based Paddle-Wheel Units. *ACS Applied Materials & Interfaces* **9,** 37463–37467. doi:`10.1021/acsami.7b12045`. (2017).

125. Curcio, V. *Henry Ford* ISBN: 978-0-19-531692-6 (Oxford University Press, New York, 2013).